Behaviour of Precast Reinforced Concrete Slabs in Steel-Concrete Composite Bridge Decks with Bolted Shear Connectors

by

Ahmad Rajabi

A thesis submitted for the fulfilment of the requirements for the degree of

Master of Engineering

School of Civil and Environmental Engineering

Faculty of Engineering and Information Technology

University of Technology Sydney

2014

CERTIFICATE OF AUTHORSHIP/ORIGINALITY

I certify that the work in this thesis has not previously been submitted for a degree nor has it been submitted as part of requirements for a degree except as fully acknowledged within the text.

I also certify that the thesis has been written by me. Any help that I have received in my research work and the preparation of the thesis itself has been acknowledged. In addition, I certify that all information sources and literature used are indicated in the thesis.

Production Note:
Signature removed prior to publication.

Ahmad Rajabi

Sydney, February 2014

ACKNOWLAGEMENTS

This thesis would not have been completed without the guidance, advice and support of a number of individuals whose contribution I would gratefully like to acknowledge. I would specially like to express my gratitude to my supervisors, Professor Bijan Samali and Dr Hamid Valipour.

I would also like to convey my thanks to University of Technology Sydney (UTS) Civil Engineering Laboratories staff, specially the laboratories manager Mr Rami Haddad, senior project engineer Mr Peter Brown and technical officer Mr David Dicker who kindly helped me in project experimental stages.

Furthermore, I am obliged to many of my colleagues and friends who assisted me during my studies. Special thanks must go to my dear friends and co-researchers, Mr Masoud Moradi for his unfailing assistance and support in this research work.

Lastly, I would like to extend my love and gratitude to my dearest family for their support and encouragement. I want to sincerely thank them from the bottom of my heart and acknowledge that without them none of this could have happened and I was not able to achieve most of the things I have in my life.

Hereby, I would like to dedicate this thesis to my family for being such great supports in my life.

LIST OF PUBLICATIONS BASED ON THIS THESIS

Journal Articles

Rajabi, A., Valipour, H., Samali, B. & Foster, S. 2014, 'Effect of Attenuation Function on the Efficiency and Accuracy of Nonlocal 1D Reinforced Concrete Frame Elements', *Computers and Concrete an International Journal* (Under publication).

Conference Papers

Rajabi, A., Valipour, H., Samali, B. & Foster, S. 2012, 'Application of externally post-tensioned FRP bars for strengthening reinforced concrete members', *22nd Australian Conference on the Mechanics of Structures and Materials*, Sydney, Australia, December 2012 in From materials to structures.

ABSTRACT

Due to ease of fabrication and maintenance and speed of construction, precast prefabricated composite deck slabs have gained huge popularity all around the globe. The precast prefabricated structural systems do not require the costly in-situ formworks. Accordingly, the precast prefabricated structural systems can reduce the cost of labour and improve the safety and speed of construction. In addition, the prefabricated composite structures can significantly facilitate application of external reinforcement in lieu of conventional internal steel bars. The reinforced concrete (RC) structures, in general, suffer maintenance and repair difficulties, as internal reinforcements in reinforced concrete (RC) structures are susceptible to corrosion that can be typically accelerated by chloride and other corrosive material ingress. Once the corrosion occurs, reinforcement starts to expand inside the concrete and that in turn causes concrete cracking and spalling. Accordingly, the reinforced concrete member cannot perform its structural role properly. Second generation bridge deck slabs, namely steel-free deck slabs, in which conventional embedded reinforcements are replaced by external reinforcements have proved to be efficient in mitigating the problems associated with corrosion of reinforcing steel bars..

The steel-free deck slabs rely on development of arching action to withstand the load. The inherent arching action in longitudinally restrained reinforced concrete members was realised about fifty years ago, however, the beneficial effects of arching action has not been recognised by most of the existing reinforced concrete design standards yet. So far only **Northern Island** Standard, DRD, NI (1990), and **Canadian** code, OHBD (1992) takes account of the enhancing effect of arching action in design practice. This intrinsic capacity of laterally restrained RC structures helps the flexural reinforced concrete members to show loading capacity far in excess of flexural resistance predicted by the conventional formulas.

Apart from corrosion of reinforcing steel bars, the existing steel-concrete composite deck slabs cannot be repaired and rehabilitated conveniently and without the interruption to the traffic. Although many studies have been conducted examining a wide range of composite deck systems, lack of a practical precast prefabricated steel-concrete deck slab that allow for easy replacement of concrete slabs in case of

deterioration is apparent. The restrained steel-free concrete deck provides a practical solution to the corrosion of reinforcement by removing the internal steel bars and replacing them with external steel straps. However, in the meshless slabs proposed by them, the future repair and replacement of concrete slab cannot be conducted easily without a major interruption to the traffic.

To take advantage of the intrinsic characteristic of precast prefabricated deck slabs and to overcome the issues associated with corrosion of internal steel bars in RC bridge decks subject to corrosive environment, a novel steel-concrete deck with precast prefabricated concrete slabs is proposed and examined in this study. The results of experimental tests on precast prefabricated slabs with high strength bolts are presented and FE numerical simulation are carried out using ATENA 2D. The novelty of this research project lies in the application of high strength steel bolts for connecting the concrete slabs to steel girders. The high strength bolts are pre-tensioned with a special amount of tensile force induced in them by a torque meter wrench. This new steel-concrete composite deck has two main advantages; firstly, there is no requirement as to design and assemble formworks for constructing cast-in-situ concrete slabs and hence the construction of deck is much faster. Secondly, the high strength bolts can be opened and the precast slab can be easily released and replaced if required. This advantage allows for easy repair and maintenance of the concrete deck slab without causing significant interruption to the traffic during repair and rehabilitation.

TABLE OF CONTENTS

LIST OF FIGURES

LIST OF TABLES

NOTATIONS

The symbols used in this thesis, including their definitions, are listed below.

A	Cross-sectional area of a rectangular concrete section
A_s	Cross-sectional area of reinforcement
A_s'	Cross-sectional area of compressive reinforcement
b	Width of a rectangular cross-section (width of slab)
c	Depth of neutral axis
C	Membrane force
C_c	Compressive force carried by concrete
C_s	Compressive force carried by tensile
d	Effective depth (the distance from the extreme fibre to the centroid of the tensile steels)
D	Diameter of high strength bolt
d_b	Diameter of steel reinforcement
d_1	Half of the arching depth
d'	Distance from the extreme compressive fibre to the centroid of the compression steels
e	Distance from neutral axis
E	Modulus of elasticity of steel reinforcement
E_c	Modulus of elasticity of concrete
f_c	Compressive strength of concrete – stress in concrete
f_c'	Characteristic compressive (cylinder) strength of concrete
E_{tot}	The total area under the load-deflection diagram up to the failure load (total energy)
E_{el}	The elastic energy
$E_{0.75pu}$	The area under the load-deflection diagram up to 0.75% the ultimate load.

f_{cu}	Compressive (cube) strength of concrete
f_{cyl}	Compressive (cylinder) strength of concrete
F_t	Post tensioning force induced in high strength bolt
f_u	Specified ultimate strength of steel reinforcement
f_y	Specified yield strength of steel reinforcement
h	Overall height of a rectangular cross-section
h_a	Height of the arch in three-hinged arch theory
h_1	Distance between membrane force at hogging and sagging
I_{10}	Energy ductility index
k	The ratio of the outward movement of the support to elastic shortening of the beam
k	Lateral stiffness in a laterally restrained RC member
K_b	Equivalent stiffness of support beam
K_d	Stiffness of diaphragm and slab
K_r	Combined stiffness of restraint
l	RC member's span length
L	RC member's span length
L_e	Half of span length in elastically restrained arch
L_r	Half of span length in rigidly restrained arch
M_a	Arching moment of resistance
M_{ar}	Arching moment of resistance of rigidly of rigidly restrained slab strip
M_{bal}	Balanced moment of resistance
M_r	Moment ratio (non-dimensional)
m_u	Sagging moment in a yielded section
m_u'	Hogging moment in a yielded section
M_b	Sagging moment in a yielded section

M_{-b}	Hogging moment in a yielded section
n_u	Difference between compressive and tensile forces in a yielded section
P	Applied load
P_a	Predicted ultimate arching capacity
P_b	Predicted ultimate flexural capacity
P_j	Johansen's loads (i.e. flexural capacity using yield line analysis)
P_m	Load due to compressive membrane action
P_p	Predicted ultimate capacity under Park's method
P_{test}	Maximum total load on the slab
P_{vf}	Flexural punching strength
P_{vs}	Shear punching strength
R	McDowell's non-dimensional parameter (elastic deformation)
t	Thickness of slab
T	Tensile force carried by tensile reinforcement
T_b	Torque applied by wrench in high strength bolt
Q_e	Effective reinforcement ratio at principal section
w	Load/(unit area carried by arching action)
w	Deflection under the point load
ε_{av}	Average axial strain in a section
ε_0	Concrete compressive plastic strain
ε_u	Concrete maximum compressive strain
ξ	Axial strain
κ	Beam/column curvature
ε	Strain
ε_c	Plastic strain of idealised elastic-plastic concrete

φ	Width of circular patch load
ρ	Longitudinal tension reinforcement ratio in a section (A_s/bd)
ρ_a	Effective arching reinforcement ratio at principal section
ρ_e	Effective reinforcement ratio at principal section
μ	Ductility index (general definition)
$\mu_\emptyset$	Ductility index in term of curvature
μ_θ	Ductility index in term of rotation
μ_Δ	Ductility index in term of deflection
μ_E	Energy ductility index
$\emptyset$	Curvature
$\emptyset_u$	Ultimate curvature
$\emptyset_y$	Yielding curvature
θ	Rotation
θ_y	Rotation at yielding
θ_u	Rotation at ultimate load
β_1	Ratio of depth of rectangular stress block, *a*, to depth to neutral axis, *c*
δ	Deflection under the load point
Δ	Deflection at centre of structure member
Δ_e	Mid-span elastic deformation
Δ_u	Ultimate deflection
Δ_p	Mid-span plastic deformation
Δ_y	Yielding deflection

Chapter 1

Introduction

1.1 Overview

1.2 Research significance and contribution

1.3 Thesis layout

1.4 Terminologies

1 INTRODUCTION

1.1 Overview

Steel-concrete composite structures have been subject of numerous studies over the last four decades. These composite structures take advantage of great performance of steel under tension and concrete under compressive. To overcome difficulties of this system for maintenance, repair and rehabilitation, precast technology have been introduced to composite construction. The composite floors with precast slabs remove the need for in situ scaffolding and formwork. The precast slabs allow for better quality control and less waste. Furthermore, the steel-concrete composite floors and decks with precast slab can significantly reduce the cost of labour and enhance the speed of construction Apart from these advantages, application of the precast slabs in composite systems can facilitate future rehabilitation and repair of composite decks and floors, provided the shear connectors allow for easy disassembling of the composite system. However, the existing steel-concrete composite floors/decks rely on shear connectors embedded in concrete that makes future disassembly or deconstruction of composite systems very difficult, if not impossible.

Considering the significant role of steel-concrete composite floors in the construction industry, particularly in bridge infrastructures, there is a need to investigate the behaviour of composite floors/decks with precast slabs that allow for easy disassembling and repair/rehabilitation of the composite systems. Accordingly, this research project focuses on the behaviour of precast slabs in a deconstructible steel-concrete composite bridge deck. The steel-concrete composite deck to be examined in this study, takes advantage of post-tensioned high strength steel bolts to transfer shear between precast slab and steel girder. In the proposed steel-concrete composite deck, transverse diagonal bracings and straps are employed to restrain the axial deformation of the precast RC slab and subsequently mobilise the mechanism of arching action that significantly enhance the loading capacity of the slab.

In this research project, ten precast reinforced concrete slab strips (i.e. one-way slab) have been fabricated and tested under a monotonically increasing displacement load applied at the mid-span. The main objective is to evaluate and determine,

- ultimate loading capacity,
- ductility,
- structural performance,
- mode of failure and

Influence of transverse straps and diagonal bracings on the enhancing effect of arching action in the proposed steel-concrete composite deck. Apart from the experimental studies, 2D continuum-based finite element (FE) models of steel-concrete composite decks are developed and analysed using ATENA 2D software. The 2D FE models are verified and calibrated against experimental data and sensitivity of FE predictions with respect to different parameters such as concrete compressive strength, post-tensioning stress in the bolted shear connectors and coefficient of friction between precast concrete slab and steel girder is investigated.

1.2 Research significance and contribution

A survey of the literature shows that almost no suitable composite bridge deck system has been proposed with the potential to be repaired and rehabilitated conveniently and without causing major interruption to the traffic. A wide range of studies have been conducted examining behaviour of steel-concrete composite decks, but lack of a composite system with precast slabs that allow for easy replacement of concrete slabs in case of deterioration is apparent. The steel-free decks proposed by researchers provide a practical solution for mitigating problems associated with corrosion of internal reinforcement, however, the existing steel-free composite decks with their shear connectors embedded in the cast-in-situ slabs cannot be easily replaced or repaired.

The composite action in steel-concrete composite floors/decks is typically developed through application of welded shear stud, with a permanent bond between concrete and steel counterparts and no chance for replacing, repairing or rehabilitating the concrete slab. A thorough literature review revealed that no experimental study on the behaviour

of precast concrete slabs with deconstructible high-strength bolted connections to steel girders has been reported. Only few researches have been reported on bolted steel-concrete composite connections that mainly focus on level of composite action in steel-prefabricated concrete slabs with bolted shear connectors. Among those researches, Lee and Bradford (2013a, b) have carried out some push-out test on the de-constructible bolted shear connectors to establish the degree of composite action and characterise the behaviour of bolted connection with respect to shear-slip diagrams obtained from the push-out tests.

In this study, results of experimental tests on prefabricated precast slabs with high strength bolts are presented accompanied with the results of the numerical simulation conducted using ATENA 2D and 1D frame FE models developed earlier by Valipour and Foster (2009). The novelty of this study is in the method of connecting the bridge decks to steel girders with high strength bolts. These bolts are pre-tensioned using a torque meter wrench and the tensile force induced in these bolts provide a shear transfer mechanism that basically rely on the friction between slab and steel girder. The proposed composite system has the following advantages;

- The precast slab decks remove the need for scaffolding and formwork and hence increase the speed and safety of construction
- The bolted shear connectors allow for easy replacement of precast slab panels. Accordingly, the future repair and rehabilitation can be conducted easily.
- The idea of steel-free corrosion-resistant composite decks with external reinforcements can be easily incorporated into this new form of composite construction. The gripping force provided by high-strength bolted shear connectors can potentially mitigate the fatigue cracks observed at the concrete slab-steel girder connection of steel-free decks.

1.3 Thesis layout

This thesis has been presented in 5 chapters;

Chapter 1, focus on the introduction and significance and innovation of this research project.

Chapter 2 comprises two parts. The first part provides a review of literature on previous studies which have been conducted on development of compressive membrane action in in longitudinally restrained flexural reinforced concrete (RC) slabs. In the second part, an overview of composite structures with precast slabs is presented. Particular emphasis is placed on the advantages and drawbacks of recently developed composite floors/decks with precast slabs to justify the need for the proposed study.

Chapter 3 includes experimental studies which have been undertaken as part of this research project. Firstly, the adopted experimental procedure and set up for testing ten slab strips is presented. Following that, the results of tests on composite bridge decks with precast RC slabs are presented and briefly discussed with particular emphasis on the ultimate loading capacity of the specimens.

Chapter 4 focuses on detailed analysis of experimental results of ten slab strips. Furthermore, finite element simulations of all ten specimens are presented and load-deflection response of the specimens obtained from FE model are compared with the experimental results.

Finally, in chapter 5 a summary of the research results is provided and conclusions are drawn.

1.4 Terminologies

Precast concrete:

Precast concrete is a construction product produced by casting concrete in a reusable mould or "form" which is then cured in a controlled environment, transported to the construction site and lifted into place. In contrast, standard concrete is poured into site-specific forms and cured on site.

Prefabricated slab:

A concrete slab may be prefabricated or in situ. Prefabricated concrete slabs are built in a factory and transported to the site, ready to be lowered into place between steel or concrete beams.

Compressive membrane action (CMA) or Arching action:

If a RC structure is restrained laterally against sideway movements, it can take advantage of inherent arching action to increase the ultimate loading capacity. Depending on the degree of lateral confinement improvement in loading capacity varies from 0 to some per cent depending on compressive strength of the concrete.

***Ductility**:*

Ductility is usually defined as ratio of the post yield deformation to yield deformation. It can be defined as ductility index or energy ductility.

FRP, fibre-reinforced polymer:

FRP is a composite material made of a polymer matrix reinforced with fibres. The fibres are usually glass, carbon, basalt or aramid, although other fibres such as paper or wood or asbestos have been sometimes used. The polymer is usually an epoxy, vinylester or polyester thermosetting plastic, and phenol formaldehyde resins are still in use. FRPs are commonly used in the aerospace, automotive, marine, construction industries and ballistic armor.

Fibre reinforced concrete (FRC):

FRC is a material made from hydraulic cement and aggregates of various sizes incorporating discrete, discontinues fibres.

Chapter 2

Background and Literature Review

2.1 Arching Action

2.2. Steel-concrete composite structures

2 BACKGROUND AND LITERATURE REVIEW

2.1 Arching action

2.1.1 Introduction

Reinforced concrete (RC) structures have exhibited strength far in excess of what is calculated using conventional bending moment design theory when the RC member is restrained in the longitudinal direction. This reserve of strength that can be mobilised by restraining the elongation of RC members is known as compressive membrane action (CMA) or arching action. The ultimate loading capacity of restrained RC members has been reported to be three times of that obtained from conventional yield line or plastic hinge analysis theory. Accordingly, in design of restrained reinforced concrete structures less steel is required, if the enhancing effect of arching action is taken into account. Using less reinforcement in the concrete slabs can also help to resolve or alleviate the problems associated with the corrosion of conventional reinforcing steel bars.

2.1.2 Different factors influencing Arching action

1- Based on pure bending theory, the tension in reinforcement will tend to have the same magnitude as the compression in concrete. The increase of reinforcing ratio in a section will demand more compressive stress in concrete and hence less compressive force will be available in concrete for arching action. This is particularly true once we postulate that compressive membrane forces develop after yielding of the reinforcement. However, this effect can be negligible as long as the ratio of tensile force in steel bars $\boldsymbol{A_s.f_y}$ over compression in concrete $\boldsymbol{f_c.h}$ is small (Christiansen and Fredriksen, 1983). Taylor and Hayes (1965) tested 22 square slabs and observed that the greatest strength enhancement occurs in the laterally restrained slabs with lower reinforcing ratio.

2- Slenderness of the slab, which is defined as a proportion of the slab length to its thickness, $\boldsymbol{l/t}$, is another factor that influences the membrane action. An increase in the slenderness will decrease the enhancing effect of compressive membrane action in RC members. Usually a slenderness ratio of 10 to 15 is the margin to consider a member as slender or thick.

3- The position of the load with respect to support can also affect the arching action. When the loading spot is closer to the supports, higher level of enhancement due to arching action is expected. Because, in such cases, the compressive arches can easily develop and directly transfer the load to the support.

4- The greater the deflection of the slab, the higher the CMA force will be.

5- The side ratio, or the slab shape factor, $\boldsymbol{l/b}$, seems to have a trivial or no influence in arching action force.

6- The concrete stress-strain model can influence the magnitude of CMA (Park and Gamble, 1980), and concrete compressive strength has a direct relationship with the magnitude of CMA force.

7- Support condition or the degree of external lateral restraint (i.e. stiffness against elongation of the RC member) is the main factor that can significantly influences the compressive membrane action.

The factor influencing development and magnitude of CMA in laterally restrained RC structure are summarised in Table 2-1.

Table 2-1. Different factors affecting compressive membrane force

	Factor	Influence
1	Concrete compressive strength	Major
2	Lateral restraint	Major
3	Stress-stress relationship	Major
4	Side ratio ($^{l}/_{b}$)	Trivial or no influence
5	Position of the load	Trivial
6	Slenderness ($^{l}/_{t}$)	Minor
7	Reinforcement ratio (ρ)	No influence
8	Deflection of the slab	Major

2.1.3 Previous studies

It is now more than fifty years since compressive membrane action (CMA) or arching action and its enhancing effects on the ultimate loading capacity of longitudinally restrained RC members has been recognised by researchers. However, so far just few design standards and codes of practices have recognised the enhancing effect of CMA on the ultimate loading capacity of the structures. Conventional code of designs for planning of concrete slabs usually advise a reinforcement ratio of 1.2% and upward (Taylor et al., 2007). However, amended standards such as **Northern Island** Standard, DRD, NI (1990), and **Canadian** code, OHBD (1992), offer a reinforcement ratio of 0.6% and 0.3% respectively. Table 2-2 shows the detail for these codes.

Table 2-2. The reinforcing proportion recommended by Canadian and Northern Island standards for concrete bridge decks.

Standard	*ρ(%)*	*Arrangement*	*Span Length (m)*	*Thickness (mm)*	*L / t*
(NI, 1990)	0.6	Top & Bot	< 2	>160	< 15
(OHBD, 1992)	0.3	Isotropic	< 3.7	>225	< 15

Development of arching action in laterally-restrained concrete slabs was initially noticed in some studies date back early 20th century. These early studies were carried out by Turner (1909), Westergaard and Slater (1921) and Gvozdev (1960).

The research on arching action can be categorised to, 1) experimental studies, 2) theoretical/analytical methods and 3) numerical (e.g. finite element FE) analysis. Furthermore, the analytical models developed for capturing the arching action falls within two major categories, i.e. plastic and elasto-plastic models. Furthermore, some of the computer-based (nonlinear finite element) models have adopted an elasto-plastic material model for concrete (Table 2-3). A detailed discussion on the available analytical models for capturing the CMA is presented in the following sections.

Table 2-3. Classification of methods available for predicting CMA

Category	*Authores*	*Year*
Elasto-plastic	Brotchie	1963
	Liebenberg	1966
	Christiansen and Frederikson	1963 & 1983
	McDowell, McKee and Sevin	1956
	Long, Rankin, Kirkpatrick, Taylor & Cleland	1975-present
	Janas	1973
Plastic	Ockleston	1958
	Wood	1961
	Morley et al	1967-1995
	Braestrup	1980's
	Kemp and Eyre	1967-1994
	Park	1960-1980
	Hayes	1968
	Sawuck and Winnicki	1965
Computer-based elastic-plastic (NLFEA)	Cope, Rao and Clark	1977-1990
	Morley et al.	1980-1995
	Bakht, Jaeger, Mufti, Agarwal and Thorburn	1980-1998
	Lahlou and Waldron	1992
	Fang et al.	1990 & 1994
	Azad et al.	1993 & 1994
	Petrou and Perdikaris	1996

2.1.3.1 PLASTIC

Ockleston (1955) is among the first researchers who noticed the enhancing effect of arching action during a destructive tests on an old RC building in South Africa when significantly higher ultimate loads compared with yield line theory predictions was observed during the test. Ockleston (1955) re-examined the results later and proposed the idea of arching action as the factor causing the increase in loading capacity after it was established that the tensile strength of concrete and strain hardening of steel were not the main reason behind significantly higher ultimate loads observed in the field tests. Arching action is generally considered to be a secondary effect that occurs after cracking of the concrete or yielding of the reinforcement and leads to substantial enhancement in the ultimate loading capacity (Ockleston, 1958).

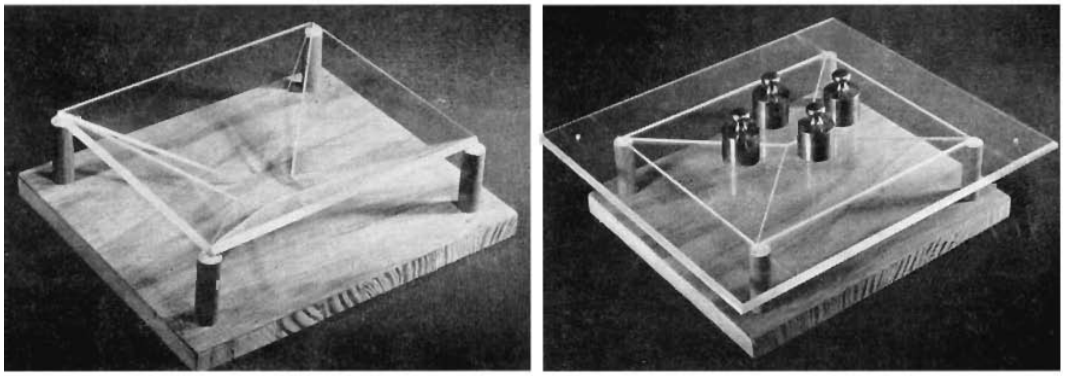

Figure 2-1. Model demonstration of arching action (simply supported without (i) and with (ii) lateral restraint, (Ockleston, 1958)).

To account for the arching action effects, Ockleston (1955) considered the yield line mechanism for a two way slab under uniformly distributed loading. Assuming no shear at the sagging yield line, by means of virtual work theory, the arching force was calculated as a function of vertical displacement at mid-span and subsequently depth of compression zone was obtained from:

$$w = C\frac{\frac{c}{a}(h-\Delta) + 2\left(\frac{a}{b}+\frac{b}{a}\right)\left(h-\frac{1}{2}\Delta\right)}{\frac{ac}{2}+\frac{2ab}{3}} \qquad \text{Equation 1}$$

The results obtained from this formula correlates satisfactorily with the experimental data on two-way slabs, provided accurate experimental deflection is used in conjunction with Equation 1.

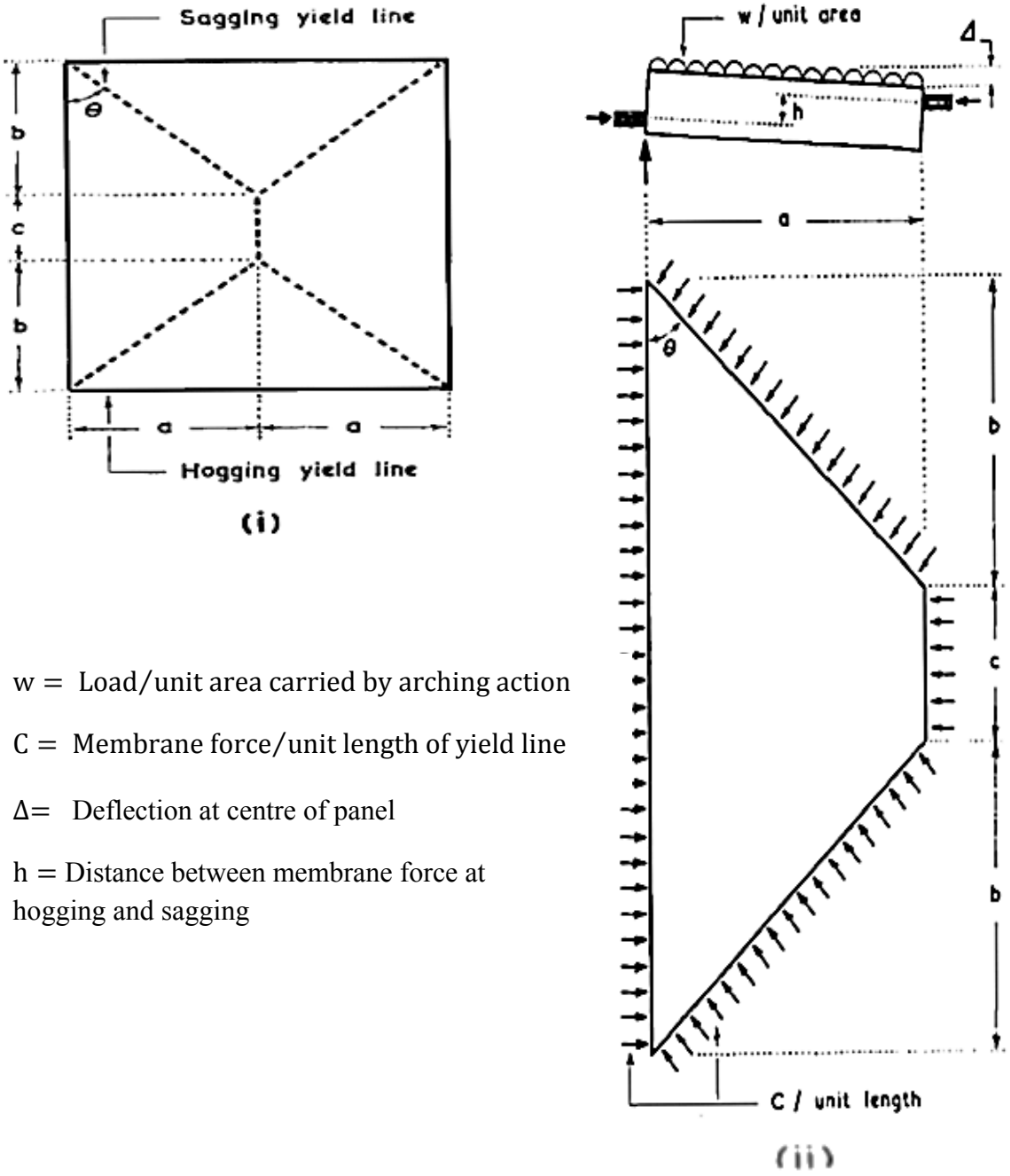

w = Load/unit area carried by arching action

C = Membrane force/unit length of yield line

Δ= Deflection at centre of panel

h = Distance between membrane force at hogging and sagging

Figure 2-2. Yield line mechanism for a two-way slab (Ockleston, 1958).

Simultaneously, Powell (1956) ran some experiments on fully restrained small scale slabs and a failure load about 1.60 to 8.25 times of what is obtained from yield line theory was observed. However, no analysis was carried out to discover the reason of behind this significant enhancement in the loading capacity.

One of the most thorough studies on the compressive membrane action (CMA) was undertaken by Park (1964a). A plastic theory of analysis was proposed by Park (1964a) to investigate the effect of arching action on rectangular slabs with all or 3 sides restrained. Park verified the results of his analytical method against experimental data on thirty-five slabs. The procedure he applied is outlined in Chapter 12 of a book by Park and Gamble (1980). Figure 2-3 depicts the geometry of the slab between the yield lines according to Park (1964a) analytical model.

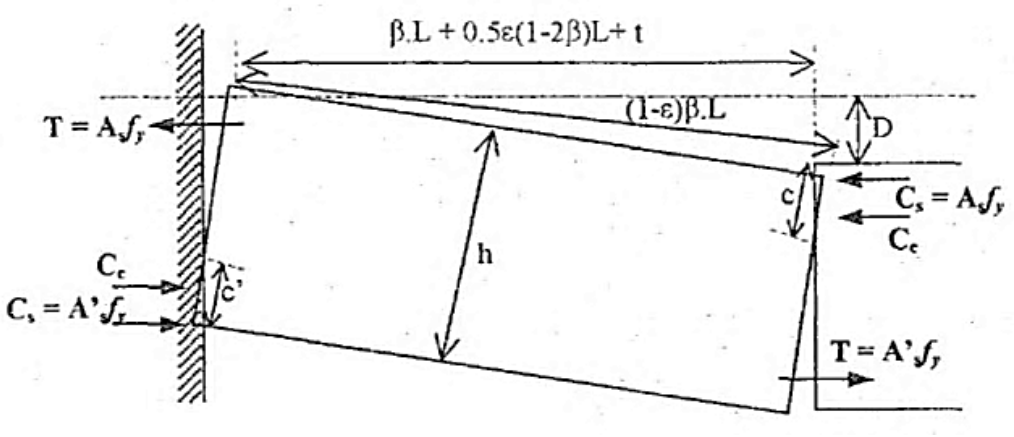

Figure 2-3. Park's geometry of slab strip portion between yield lines (Park and Gamble, 1980).

In Park's model, the moment at the yield section about the mid-depth is obtained from;

$$m_u + m'_u - n_u\delta \qquad \text{Equation 2}$$

where,

$$n_u = C_c + C_s - T \qquad \text{Equation 3}$$

$$m_u = C_c(0.5h - 0.5\beta_1 c) + C_s(0.5h - d') + T(d - 0.5\text{h}) \qquad \text{Equation 4}$$

where, m_u is, m'_u are sagging and hogging moment respectively.

To use this formula, the value of mid span deflection is required to be available. Considering the challenges of calculating the deflection, Park introduced an empirical value of half the slab thickness in his estimation to simplify the calculations. Park's analytical model showed that Johansen's yield line theory dramatically under-estimates the ultimate strength of restrained slabs. It is noteworthy that Parks' model cannot capture the load-deflection response and this is considered the major short coming of plastic theory models.

In a different study, the influence of sustained loads on the ultimate loading capacity of the partially restrained slabs was studied by Park (1964b). This study focused on the influence of lateral stiffness in development of compressive membrane action in slab-beam systems.

Membrane action in reinforced concrete slabs is induced in two forms; i.e. compressive membrane action (CMA) and tensile membrane action (TMA) or catenary action that typically takes place at large deflections. Development of CMA starts immediately after formation of cracks in the member, whereas TMA typically develops at large deflections when the neutral axis reaches the farthest compressive fibre in the concrete.

Desayi and Kulkarni (1977) performed an extensive literature review on several studies conducted to analyse CMA and TMA effects. They observed that most of studies prior to that time aimed at calculating the ultimate loading capacity of RC slabs either restrained or simply supported and no consideration was given to influence of CMA on the serviceability (e.g. deflection and crack width) of RC slabs.

To analyse the laterally restrained slabs, some researchers such as Wood (1961), Park (1964a), Sawzuck and Winnick (1965), Morley (1967), Hung and Nawy (1971), Ramesh and Datta (1973), and Datta and Ramesh (1975) proposed analytical methods based on rigid-plastic material models. Such models typically calculate the maximum loading capacity at zero deflection (Figure 2-4). However, the results obtained from these methods can be significantly influenced by the assumptions made regarding the mid-span deflection at ultimate loading capacity. For example, Park and Morley introduced the value of 0.5 times the slab thickness as the deflection at peak load, whereas Hung and Nawy (1971) considered it as (0.4-1.0) times the slab thickness.

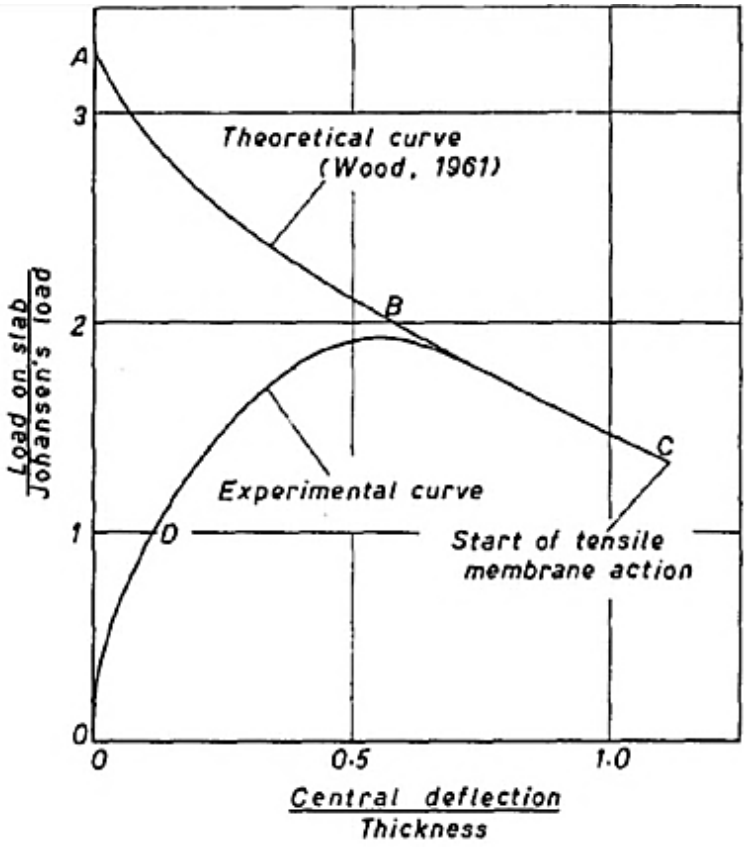

Figure 2-4. Typical theoretical & experimental load-deflection curves for a fixed slab (Wood, 1961).

In the case of simply supported slab, the analytical model of Wood (1961), Sawzuck and Winnick (1965), Morley (1967), Kemp (1967), and Hayes (1968) were able to capture the ultimate loading capacity of the slab as well as the catenary action. Since the enhancement of the loading capacity due to TMA occurs at large deflections, it is crucial to determine the deflection with reasonable accuracy, however, these rigid-plastic methods fail to provide a reasonable estimation for deflection at mid-span. As shown in Figure 2-5 the load-deflection curve of these rigid-plastic methods start from Johansen's yield line theory that is not realistic.

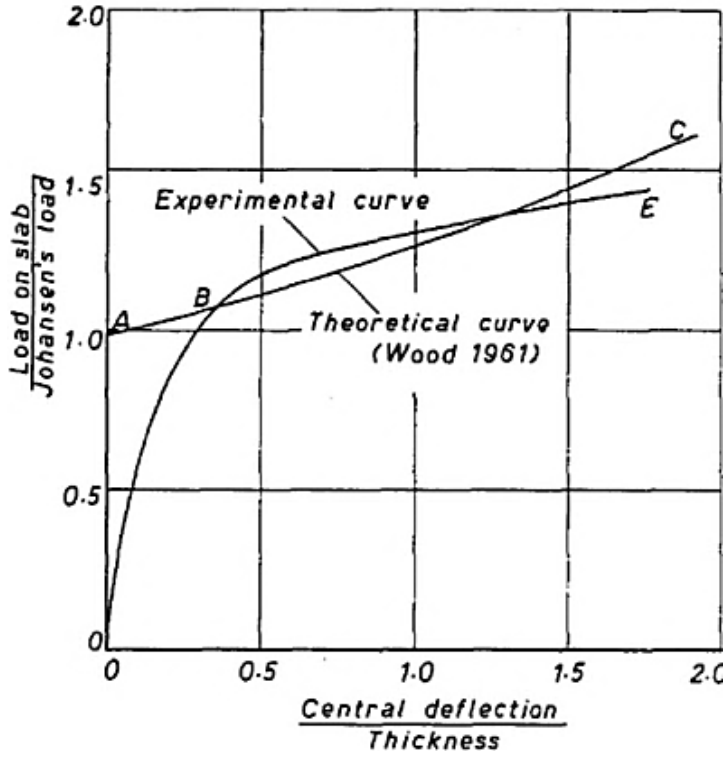

Figure 2-5. Typical theoretical & experimental load-deflection curves for a simple support slab (Wood, 1961).

2.1.3.2 ELASTIC-PLASTIC

The main advantage of elasto-plastic models over plastic ones is that they consider deflection of the structure in the calculations; hence such models can capture the whole load-deflection response of the slab. Almost in all the analysis conducted using elasto-plastic models, ultimate capacity of the structure has been considered as sum of the flexural failure caused by yielding of reinforcement and arching action strength induced in the model due to longitudinal restraint.

In 1963, Christiansen investigated effect of CMA on one- and two-way slabs both experimentally and analytically. Assuming that fully plastic hinges are developed at mid-span and supports of the beam, Christiansen (1963) equated the outward movement of the supports with the elongation of the beam that can expressed as, movement at support = elongation due to rotation – elastic shortening – plastic shortening,

$$\frac{k\delta CL}{2E_c h} = \frac{a_1 2\delta\Delta}{L} - \frac{\delta CL}{2E_c h} - \frac{4\Delta_p \delta C}{Lf_c} \quad \text{Equation 5}$$

where ***k*** is the ratio of the outward movement of the support to elastic shortening of the beam.

Finally, Christiansen (1963) defined the arching force as follows,

$$Ca = x(k_1 - y - x)h^2 f_c \quad \text{Equation 6}$$

where

$$k_1 h = h - \Delta_e - (T_1 + T_2)/f_c \quad \text{Equation 7}$$

and

$$k_2 = (1 + k)f_c L^2/8E_c h^2 \quad \text{Equation 8}$$

Due to complexity of this formulation, Christiansen (1963) proposed a graphical solution to determine the CMA force (Figure 2-6).

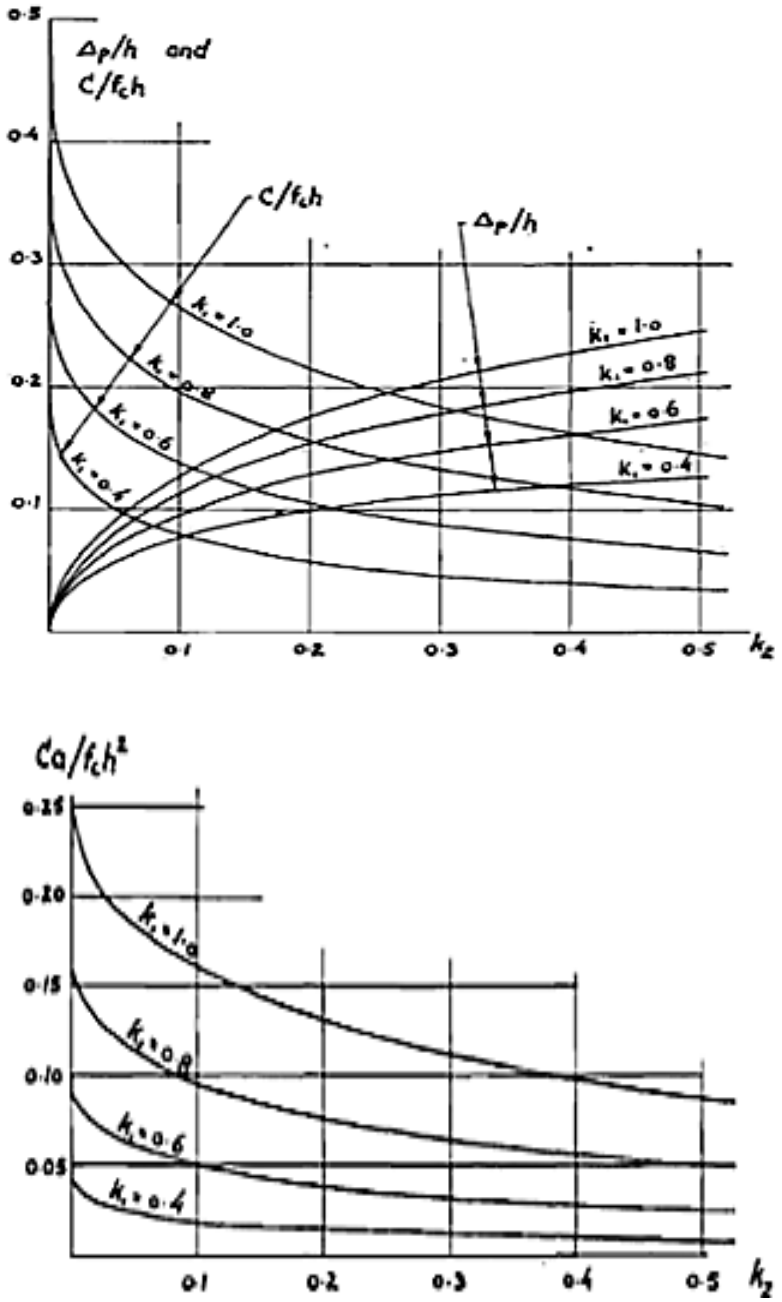

Figure 2-6. Graphical solution for calculating CMA force (Christiansen, 1963).

Besides, Christiansen conducted some tests to validate his model; Christiansen's model adequately captured the response and loading capacity of one-way slabs, but for two-way slabs his results were quite conservative. Later in another study, Christiansen and Fredriksen (1983) modified the definition of CMA force to,

$$P_m = P_{test} - P_j \quad \text{Equation 9}$$

P_m is load due to compressive membrane action, $P_{test}$is the maximum total load on the slab and P_j is the Johansen's loads (i.e. flexural capacity using yield line analysis).

Through their investigation on 2 full-scale slabs, Christiansen and Fredriksen (1983) realised that neither reinforcement ratio nor side ratio ($\boldsymbol{l/b}$) has any effect on CMA force, but slenderness proportion, $\boldsymbol{(l + b)/2h}$ can influence the arching action. An analytical model derived from the experimental study of 76 various samples in the literatures showed that the ultimate capacity of the slabs can be calculated from

$$P = P_j + k.h^2 f_{cyl} \quad \text{Equation 10}$$

where k can vary from 1 to 3 for rigidly restrained slabs. In case the load is not uniformly distributed, the CMA force was estimated as

$$P_M = (P_{test} - P_j)\,\bar{x}_p/\bar{x}_0 \quad \text{Equation 11}$$

This formula implies that the closer the load is to the supports, the larger the enhancing effect of arching action will be.

One of the research centres which have made a major contribution to the study of arching action in deck slab systems is School of Built Environment at Queen's University, Belfast. Various scholars at this research centre from early 1970s up to now have focused on experimental/analytical studies of the CMA in the restrained slabs.

In mid- late sixties, Long and Bond (1967) observed that full panel specimens have higher loading capacity compared to their conventional counterparts. Later, Masterton and Long (1974) investigated the enhancement in the punching shear of slabs due to development of CMA force in slab-column structures. Masterton and Long (1974) derived a formula that can accurately predict the punching shear strength of full panel specimens, assuming that portion of the slab inside the contraflexure line is laterally restrained by the surrounding slab.

Rankin (1982) in his PhD dissertation proposed a model for predicting the ultimate strength of laterally restrained slabs. In Rankin's model, the restrained RC member is simulated as a three-hinged arch with flexible end supports as shown in Figure 2-7.

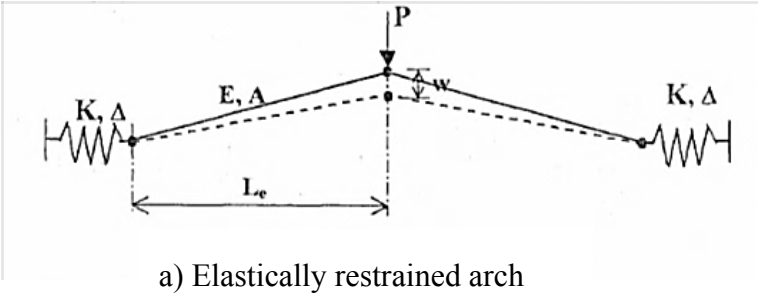

a) Elastically restrained arch

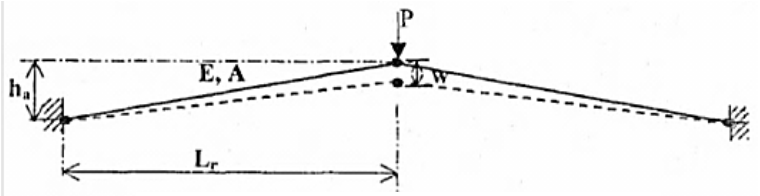

b) Equivalent rigidly restrained arch

Figure 2-7. Analogy of three-hinged arch (Rankin, 1982).

Following a two phase approach similar to what had been proposed earlier by Long (1975), the failure load of a two way slab under concentrated load can be calculated. To predict the failure load of the restrained RC structure, Long (1975) found the enhanced flexural and punching shear capacity separately and considered the lesser of these two as the ultimate loading capacity of the structure. Rankin and Long in a study conducted in 1987 proposed a novel approach for prediction of punching shear strength of conventional slab-column specimens (Rankin and Long, 1987a). The flowchart of method developed by Rankin and Long (1987a) is depicted in Figure 2-8. The proposed method was validated by considering the outcome of 27 slab-column test specimens and a good correlation was observed.

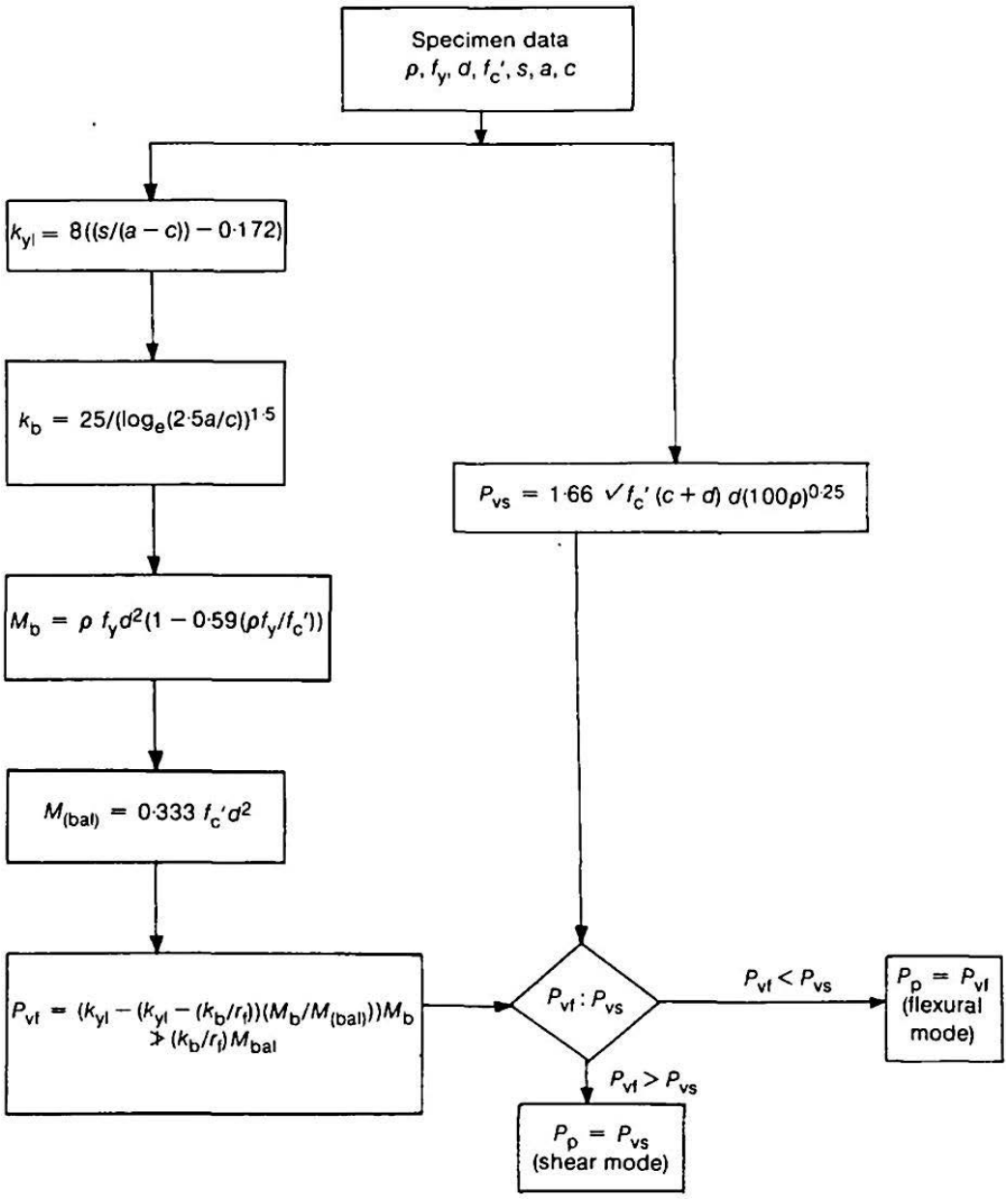

Figure 2-8. prediction of punching shear stress of conventional slab-column specimens (Rankin and Long, 1987a).

Later, Rankin and Long (1987b) refined the 3-hinged arch model to capture the flexural and punching shear capacity of full panel specimens in an interior column-slabs (Figure 2-9). The base of this refined model was the same as what was proposed for conventional slab-column systems. Rankin and Long (1987b) took into account the enhancing effect of membrane action on the punching shear capacity of full panel specimen. Figure 2-9 shows the mechanism of membrane action mobilised in a full panel specimen.

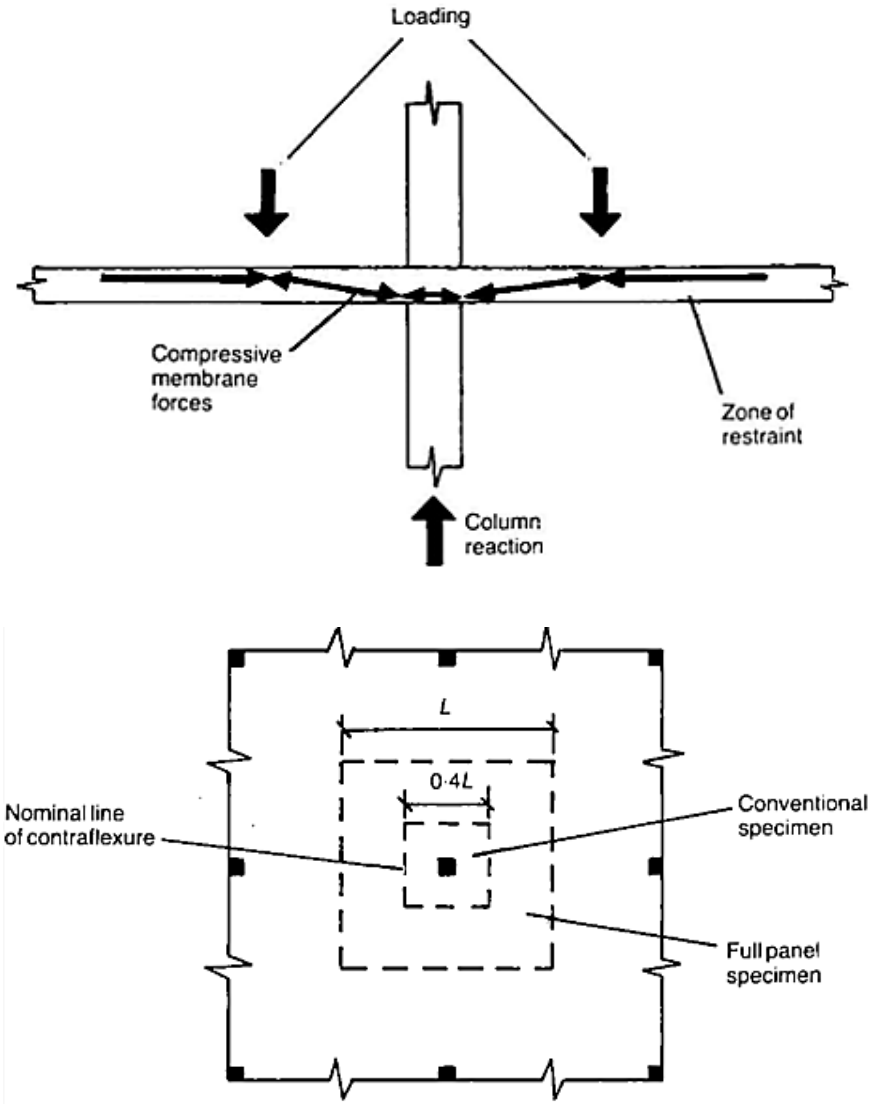

Figure 2-9. Concept of compresive membrane action in interior slab-column connections (Rankin and Long, 1987b).

Similar to Rankin's study in 1982, Rankin and Long (1987b) followed a two phase approach and stated flexural and punching shear strength of the slab as

$$P_{vf} = [3 + 16c/L - (3 - 8c/L)w^{0.5}]w^{0.5} f_c' d^2 \quad \text{Equation 12}$$

and

$$P_{vs} = 2.66\sqrt{f_c'(c + d)dw^{0.15}} \quad \text{Equation 13}$$

for the critical section at the distance of $d/2$ from the column face. The ultimate strength in this model is assumed to be the lesser of punching shear and flexural capacity. The punching shear capacity of 17 different interior slab-columns was predicted by Rankin and Long (1987b) analytical model and it was observed that the existing models in the design codes underestimate the capacity by 30-50% (see Figure 2-10). Also, the greatest enhancement was related to samples with lower reinforcing proportion and smaller span to depth ratios. The effects of prestressing and eccentric loading can also be satisfactorily taken into account, in the model developed by Rankin and Long (1987b).

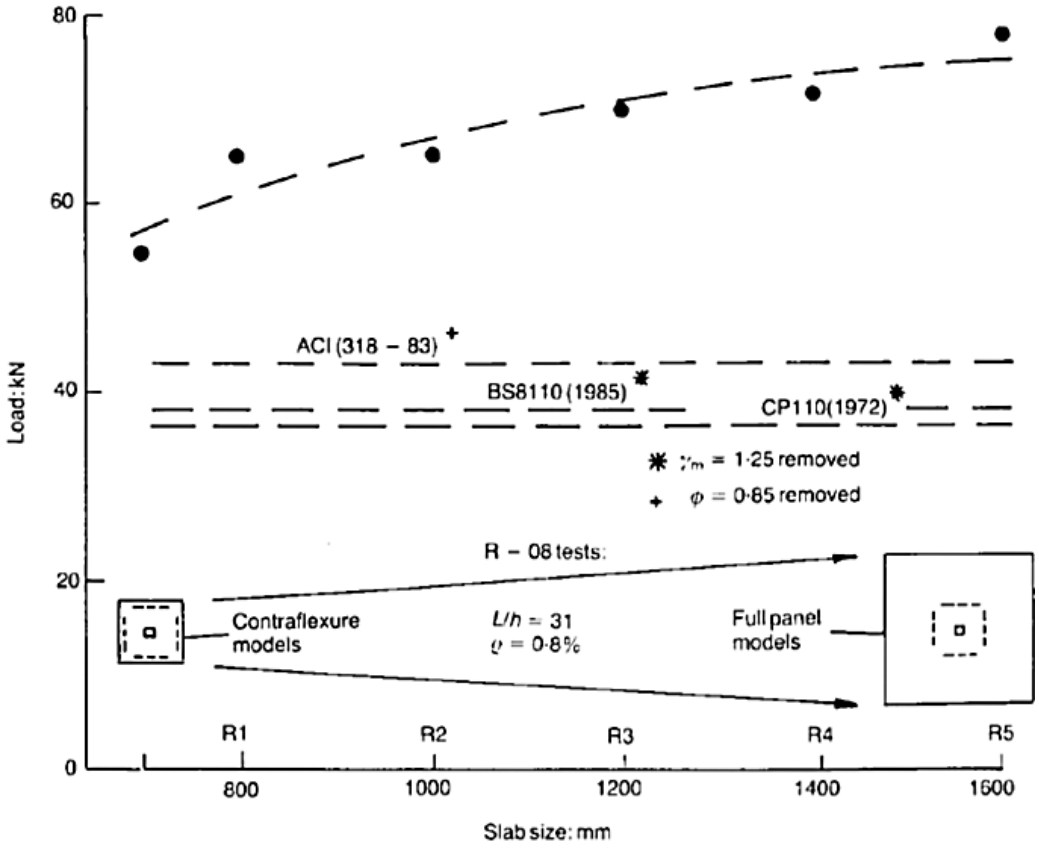

Figure 2-10. Comparison of the ultimate loading capacity predicted by desing codes with large panel test results (Rankin and Long, 1987b).

Kirkpatrick et al. (1984a) ran some experiments on 20 one-third scale M-beams that represent the bridge deck slabs. Although all deck slabs were reinforced assuming that flexural failure governs the design, but all the panels, even those with low reinforcing ratios failed in punching shear. Accordingly, it was concluded that the strength of slabs

is independent of their reinforcing ratio owing to significant strength enhancement provided by CMA.

In addition, Kirkpatrick et al. (1984a) refined the two-phase model of Long (1975) assuming that slabs are fully-restrained. The core idea in Kirkpatrick's model was that the arching action bending moments can be initially obtained from

$$M_{ar} = k f_c' h^2 \qquad \text{Equation 14}$$

where

$$k = \frac{0.21 M_r}{4} \qquad \text{Equation 15}$$

$$M_r = 4.3 - 16.1\sqrt{(3.3 \times 10^{-4} + 0.1243R)} \quad (0 < R < 0.26) \qquad \text{Equation 16}$$

$$R = \frac{\varepsilon_c L_r^2}{4 d_1^2} \qquad \text{Equation 17}$$

$M_r = 4$ for rigid plastic material
$M_r < 4$ for elasatic- plastic material

An equivalent percentage of reinforcement was introduced in this method that creates the same strength enhancement as CMA force. Finally, postulating that critical section is at the distance of $d/2$ from the edge of loading plate, the enhanced punching shear was calculated,

$$P_p = 1.52(\varphi + d) d \sqrt{f'_{cyl}(100 Q_e)^{0.25}} \qquad \text{Equation 18}$$

It should be noted that in this approach the effect of steel reinforcement in the loading capacity is neglected. Highest punching shear capacity was obtained for slabs with lower span to depth ratio and higher f_c'. Excellent correlation is achieved with experimental data, produced according to UK and North American bridge design codes (Figure 2-11).

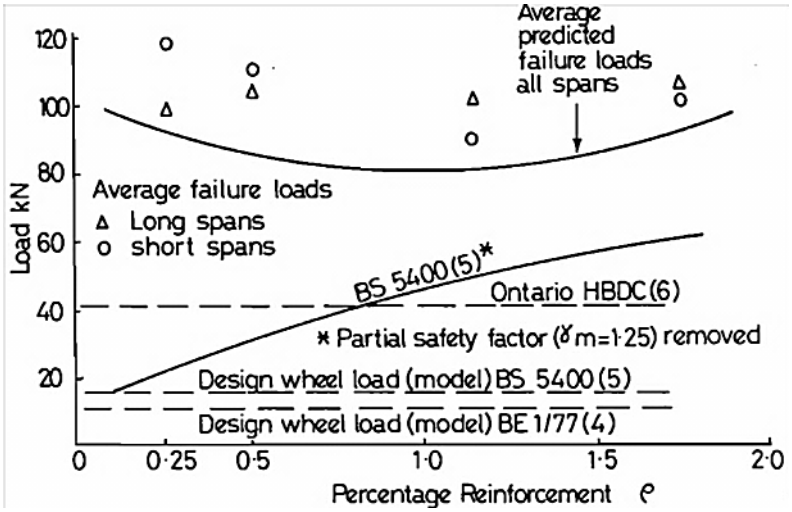

Figure 2-11. Comparison of the results with US and UK codes (Kirkpatrick et al., 1984a).

Later in 1986, Kirkpatrick and his colleagues evaluated the influence of CMA on the serviceability of M-beam bridge decks. They monitored the behaviour of an M-beam slab and concluded that even at low level of loading, arching action plays a role in controlling the cracks (Kirkpatrick et al., 1986).

As part of a research PhD project, Niblock (1986) evaluated different analytical approaches developed for predicting the strength of restrained slabs under uniformly distributed loading. Skates (1987) investigated the feasibility of utilising arching action in cellular structures and Ruddle (1990) appraised the effect of CMA on the laterally restrained rib slab systems.

Typically the existing analytical models can only capture the effect of arching action in fully restrained slabs and in these models less attention is paid to the significant influence of lateral stiffness on the magnitude of CMA force (Kirkpatrick et al., 1984a). However, there are elastic-plastic models based on three-hinged arch analogy (Rankin and Long, 1997) that can properly capture the CMA in laterally restrained slabs with flexible end connection. These models are based on deformation theory presented by McDowell et al. (1956) in which the bending capacity and arching strength are separately calculated and then superimposed to get the overall strength of the slab (Figure 2-12).

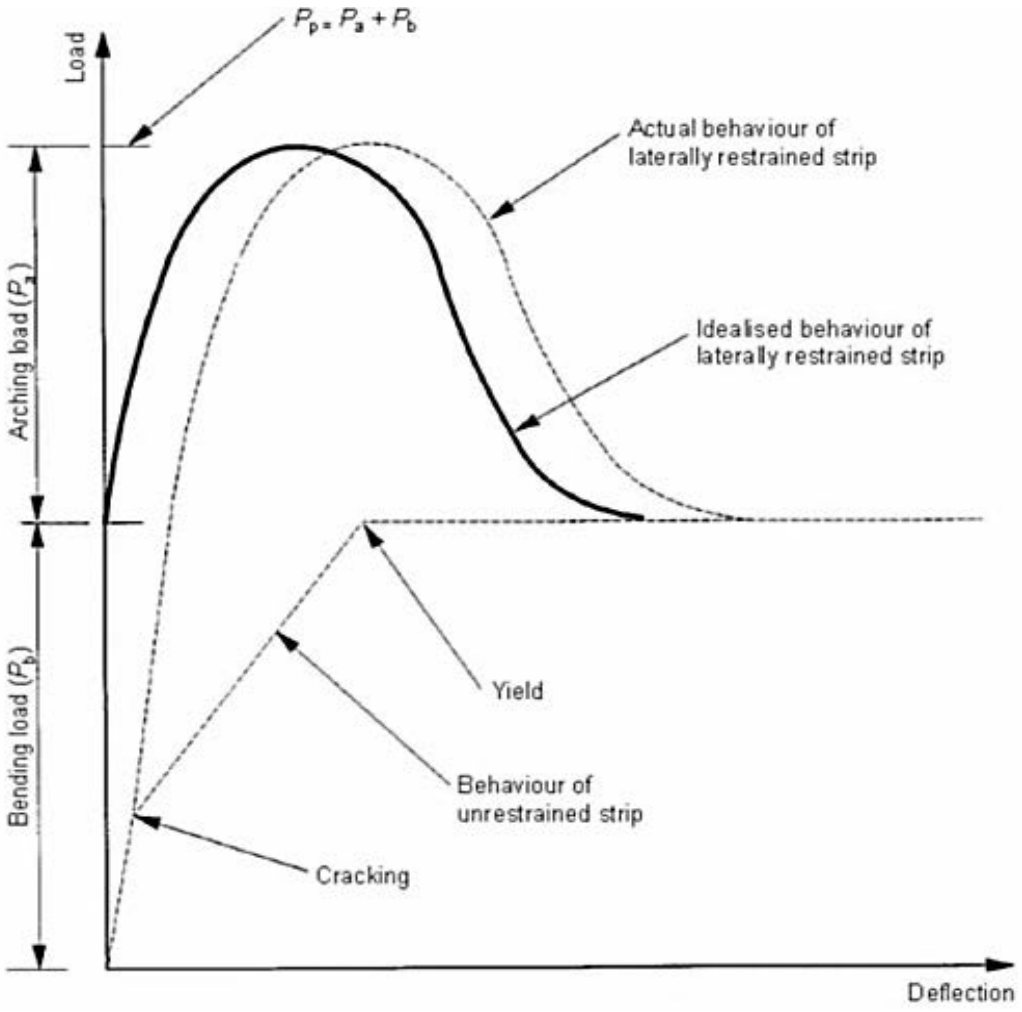

Figure 2-12. Actual and idealised behaviour of restrained RC member (Rankin and Long, 1997).

In reality, the flexural and arching strength of RC members are interrelated and development of compressive membrane action (CMA) is associated with the start of loading and formation of micro-cracks while the stress in steel bars is far less than f_y. However, in the model developed by Rankin and Long (1997), the enhanced ultimate load is expressed as

$$P_p = P_b + P_a \qquad \text{Equation 19}$$

where P_p and P_a are arching and bending resistance respectively and

$$P_a = kM_a \quad \leftarrow \quad \left(M_a = M_{ar}.{}^{L_e}/_{L_r}\right) \;\&\; \left(M_{ar} = M_r.\,0.85f_c'\,{}^{d_1^2}/_{4}\right) \qquad \text{Equation 20}$$

and

$$P_b = k(M_b + M_{-b}) \;\; \& \;\; M_b = \rho f_y d^2 \left(1 - 0.59 \frac{\rho f_y}{f_c'}\right)$$

Equation 21

(Mattock et al. (1961))

The ability of this analytical model for capturing the CMA has been demonstrated against a wide range of experimental data (see Figure 2-13). However, this model is only applicable for estimating the enhancing effect of CMA on the flexural capacity and no consideration is given to calculation of the enhanced punching shear strength.

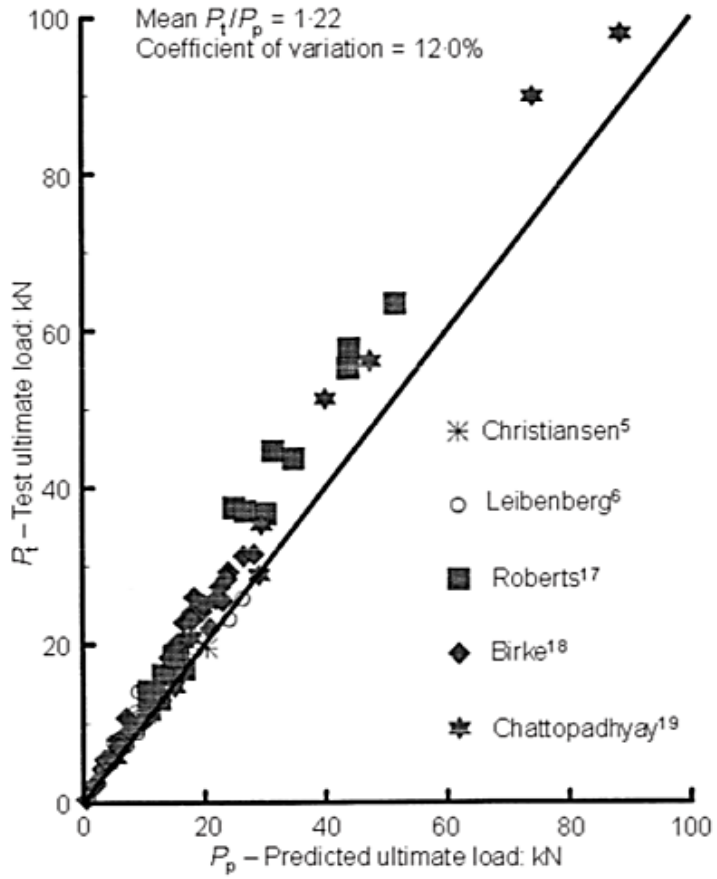

Figure 2-13. Comparison of test results with some literature (Rankin and Long, 1997).

In 2000, Taylor presented her PhD thesis focusing on CMA influence on high performance concrete (HPC) slabs (Taylor, 2000). In order to assess the degree of lateral restraint, Taylor et al. (2001) proposed a novel approach in which the supporting edge beams, end diaphragm and surrounding area of unloaded slab are replaced by springs with an equivalent stiffness.

$$K_r = 1/(1/K_b + 1/K_d)$$ Equation 22

Taylor's approach was based on integrated deflection theory of Rankin and Long (1997). In this approach, after calculation of the arching moment, the equivalent reinforcement was introduced to the model that cause the same amount of enhancement in the bending moment (Kirkpatrick et al., 1984a),

$$\rho_e = (\rho_a + \rho).\left(\frac{f_y}{320}\right) = \left(\frac{M_a+M_b}{M_b}\right).\left(\frac{f_y}{320}\right)\rho$$ Equation 23

Finally, the enhanced flexural and shear capacity of the slab calculated and the lesser of these two is considered as the ultimate loading capacity of the member. It should be noted in this model the critical section is assumed at the distance of $d/2$ from the edge of loaded area.

Ruddle et al. (2002) conducted some analytical and experimental studies to investigate the flexural and shear strength enhancement in rectangular and T-beams. Tee beams provide greater area of compression zone resulting in more flexural resistance. Also, at the same time T-beams have more potential for development of arching action due to increase in the lever arm. Ruddle adopted two assumptions, i.e. elastic and elastic-plastic stress distribution for calculating the lever arm of acting thrust force on the contact zones. Furthermore, in the model developed by Ruddle et al. (2002), no shear reinforcement was considered. The integrated method of Ruddle et al. (2002) showed better correlation with experimental results (see Figure 2-14) compared with the two-phase model of Rankin and Long (1997).

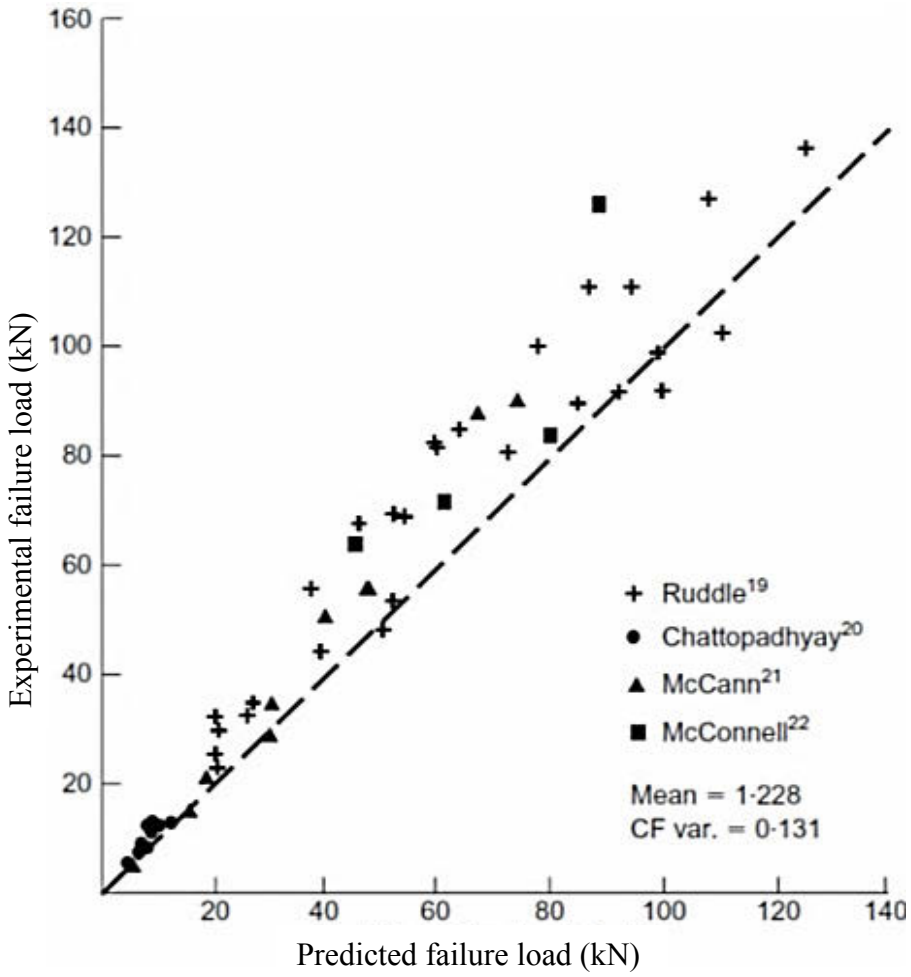

Figure 2-14. Comparison of test results from various sources with predicted failure loads.

Utilising the benefit of more durable high strength concrete slabs, Taylor (2000) extended Rankin and Long (1997) theory to incorporate high strength concrete by modifying the stress-strain block as follows

$$\varepsilon_0 = 2\varepsilon_u(1-\beta) \qquad \text{Equation 24}$$

$$\varepsilon_u = 0.0043 - [(f_{cu} - 60) \times 2.5 \times 10^{-5}] \qquad \text{Equation 25}$$

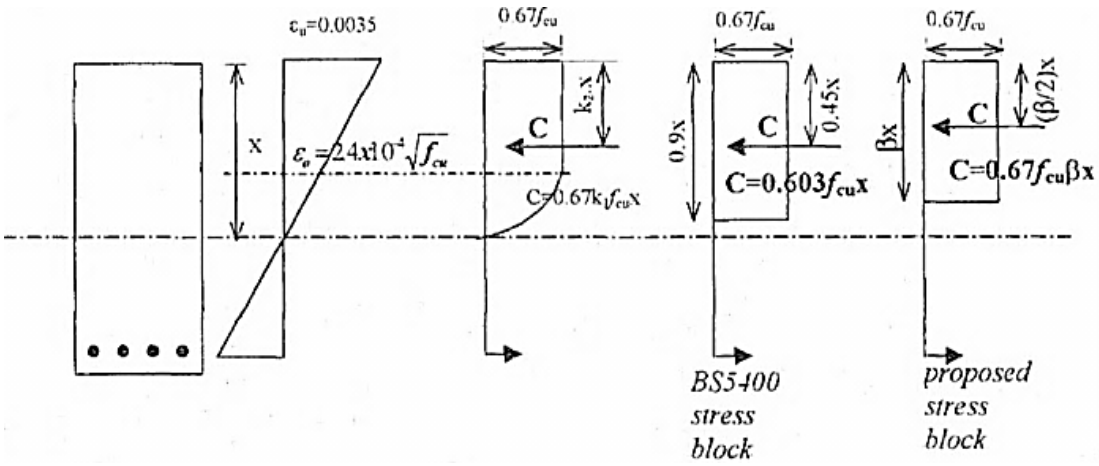

Figure 2-15. (BS 5400) conditions at ultimate flexural load for NSC ($f_{cu} < 60\ N/mm^2$) and Taylor (2000) approach.

Besides, fifteen full scale one way RC slabs with a wide range of boundary conditions (different stiffness along the member axis) and various reinforcement settings (including FRP reinforcement) and the setup shown in Figure 2-16 was tested by Taylor (2000).

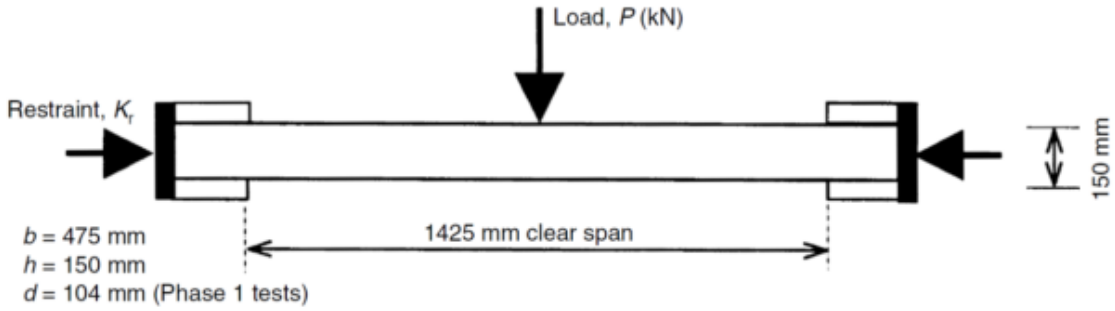

Figure 2-16. Model test load arrangement (Taylor, 2000).

It was realised that British Standard, BS 5400 (1990), is accurate in the case of simply supported slab. Besides, the crushing of concrete becomes more prominent as f_c' increases and a failure mode similar to over reinforced concrete slab was observable. In laterally-restrained slabs, the failure load increases in proportion to lateral stiffness of end supports and compressive strength of concrete. A flexural strength about 1.5 to 3.6 times of the pure flexural strength could be achieved. The deflection-based model developed by Rankin and Long (1997) was employed for predicting the behaviour of

slabs with high-strength concrete and a good correlation with the experimental results was observed.

$$M_b = A_s f_y d\left(1 - \left(0.746 A_s f_y / f_{cu} bd\right)\right)$$ Equation 26

2.1.3.3 Numerical simulations

Over the last two decades, several attempts have been made to develop simplified analytical methods that properly capture the membrane behaviour of RC members subjected to medium to large displacements (Izzuddin and Elghazouli, 2004, Omer et al., 2009). In addition to simplified analytical methods, advanced numerical methods, particularly finite element (FE) models, have been extensively used for nonlinear analysis of RC structures (Spacone et al., 1996, Bao et al., 2008). However, application of FE models for capturing the membrane behaviour of laterally restrained RC beams and slabs that can potentially develop membrane action has been hampered by numerical complexities such as spurious mesh sensitivity and lack of objectivity due to concrete crushing and cracking (Lahlouh and Waldron, 1992, Sasani and Kropelnicki, 2008, Valipour and Foster, 2010). Furthermore, existing continuum-based FE models are time demanding and rupture of reinforcing bars leads to discontinuity, which cannot be captured by such FE models. On the other hand, 1D frame FE models offer the accuracy and efficiency required for such studies (Izzuddin and Elghazouli, 2004, Valipour and Foster, 2010).

2.2 Steel-concrete composite structures

2.2.1 Introduction

The steel-concrete composite construction techniques generally tend to be the preferred method of construction in Australia, New Zealand and most developed countries. Except in long-span bridges, these composite floors or decks are usually made of reinforced concrete slabs connected to steel beams through some mechanical connectors such as shear studs or parallel flange channel welded to the steel girder flange and

embedded in concrete. These composite systems have low cost and high strength required for covering large floor and deck areas.

In the simply supported steel-concrete composite systems, the tensile force at the mid-span is taken by steel girders and the compression is assumed to be resisted mainly by an 'effective' breadth of RC slab.

Over the last century, a wide range of experimental and analytical studies have been devoted to development and design of composite system with higher level of composite action. Some researchers in Canada, such as Bakht and Mufti and their colleagues introduced the second generation steel-free deck slabs. Slabs devoid of steel are one solution which can resolve the corrosion of steel bars buried in the concrete slab. The corrosion of steel bars which is typically accelerated by ingress of chloride and other corrosive materials can significantly reduce the service life and loading capacity of the structures particularly the bridge decks exposed to harsh environmental conditions.

Composite slabs are usually constructed in two different forms, i.e. precast and cast-in-situ. Each of these methods has its own advantages. Due to fast fabrication and assembly of precast composite slabs, the use of these structures has gained huge popularity over the last decades. Moreover, these types of composite structure remove the need to design the main structure for withstanding the self-weight of formworks required during cast-in-situ construction. The structural behaviour of composite floors/decks and the interaction between steel beam concrete slabs can be categorised to 1) full interaction, 2) partial interaction and 3) no interaction.

From design point of view the full composite action provides the most efficient structural system, however, in practice the full composite action cannot be achieved and the existing methods for connecting the slab to steel beam can only provide partial interaction in which the slip between steel girder and concrete slab affects the stress distribution over different components (i.e. RC slab and girder).

The bond between steel and concrete is typically provided by mechanical shear connectors. Also, the bond can be provided by chemical adhesives. These mechanical or chemical bonds are designed to withstand the longitudinal shear flow developed on the

interface between slab and steel girder. This interface is a region of severe and complex stress regimes that defies any accurate analysis. Accordingly, the stiffness and strength of existing connections are empirically determined through lab tests. The most common tests used for characterising the bond between steel and concrete (i.e. mechanical behaviour of connectors) is the push-out test that can provide the full load-slip response of the composite connections.

The novel steel-precast concrete composite system to be proposed in this research project is inspired by steel-free bridge decks. Accordingly, in the next section a review of literature on steel-free bridge decks is carried out.

2.2.2 Previous studies

One of the recent novel ideas on composite bridge decks with concrete slab and steel girders have been proposed by Mufti et al. (1993). Mufti and his colleagues tested concrete decks devoid of internal reinforcement. The main objective was to resolve the corrosion of internal reinforcement accelerated by penetration of de-icing salt into the concrete. Hence, Mufti et al. (1993) replaced the internal steel bars with external transverse confining straps. The external straps were placed close to the soffit of deck slab and welded to the shear studs. The steel-free deck slabs mainly rely on development of arching action; in the longitudinal direction, the slabs are restrained by steel girders and in the transverse direction the slabs are restrained by straps connecting the top flanges of the adjacent girders running in parallel.

Since the welded strap is not suitable for all situations, Bakht and Mufti (1996) proposed several alternatives to the welded straps that conform to OHBD (1992) requirements. Figure 2-17 shows these transverse restraining options. Each of these systems has its own merits in terms of economy and durability. For instance threaded bars can be replaced easily. Besides, steel-free deck slab does not need waterproofing membrane and asphalt layer for wearing surface.

The behaviour of systems transversely restrained by cruciform strap and threaded bar have been experimentally investigated by Bakht and Lam (2000). In these system the arching action in the transverse direction is provided by,

1- Bottom transverse reinforcement which acts as tie (Bakht and Mufti, 1996).
2- External straps lying under the slab (Salmon River Bridge – welded straps).

Also, in the longitudinal direction, the restraint is provided mainly by the steel girders which are connected to the soffit of slab by the shear connectors.

The steel-free deck slab system exhibited failure loads of more than 10 times the theoretical bending failure load, owing to development of arching action.

Newhook et al. (2002) extended the idea of steel-free deck slabs in conjunction with cast-in-situ concrete slabs for rehabilitation of bridge decks in Canada. Newhook and his colleagues took advantage of the maximum possible arching action in slab on girder systems and they created a structure with lighter weight. Also, they overcame the issue of premature deterioration associated with corrosion of the internal reinforcement. However, application of cast-in-situ concrete slabs in conjunction with steel girders can hinder any future attempts for rehabilitation and repair of RC bridge decks.

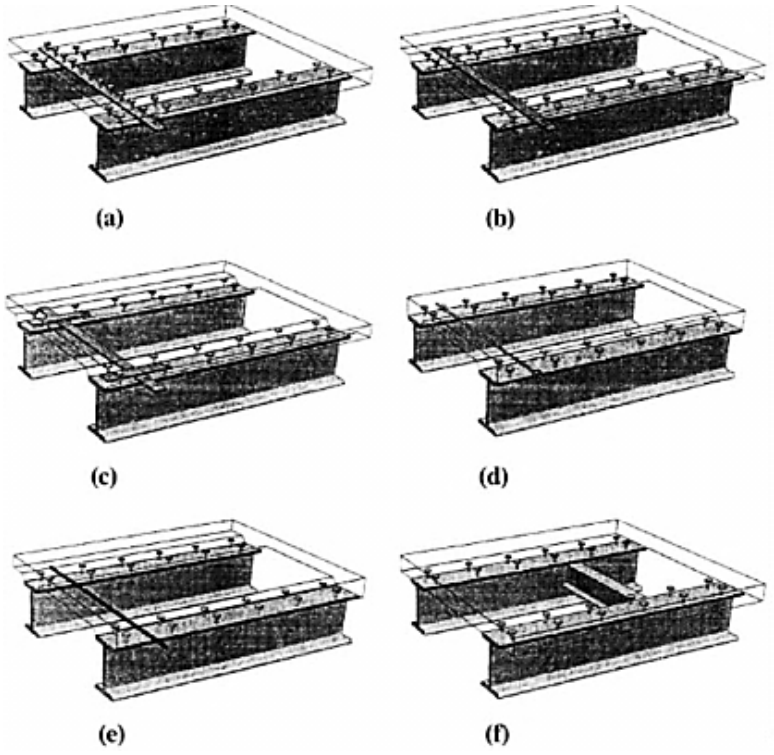

Figure 2-17. Various alternatives for transverse confining systems: (a) Fully studded strap; (b) Partially studded strap; (c) Crucisorm strap; (d) Mild steel threaded bar; (e) FRP bar; (f) Diaphragm (Bakht and Mufti, 1996).

More recently, Klowak et al. (2006) introduced the second generation steel-free bridge decks that takes advantage of internal CFRP/GFRP bars and external steel straps. The advantage of this system is that the CFRP or GFRP bars can control the cracks and eliminates corrosion in the deck and external steel straps prevents the growth of longitudinal cracks.

Over the last three decades many researchers have focused on the short- and long-term behaviour of steel-concrete composite structures with cast-in-situ slabs. However, less attention has been paid to application of steel-concrete composite decks with precast slabs.

Although there are countless studies on steel-concrete composite structures, but lack of a convenient composite system suitable for bridge decks, with the ability to be easily repaired/rehabilitated, is still apparent. The majority of composite systems which have been developed so far take advantage of conventional cast-in-situ structures. In these structural systems a strong bond between steel girder and concrete slab can be provided. To fabricate these structures, one should first make the formworks that increase the cost of the structure dramatically. In addition, the cast-in-situ slabs, with shear connectors permanently embedded in the concrete, are not conducive to easy maintenance and rehabilitations/repairs. Accordingly, some precast composite structures have been introduced through various studies. In the existing composite system, grouting has been largely used for connecting the precast deck slabs to steel girders. In both cases of precast and cast-in-situ composite decks, corrosion of internal reinforcement and the issues with repair and rehabilitation are still present and no applicable solution have been proposed to solve these issues. Besides, most previous research has been conducted on composite beams with welded shear studs that cannot be deconstructed easily.

In fact, it is just the shear connector that determines the ability of a composite system to be deconstructed or easily replaced. Few studies have been devoted to bolted shear connectors. Dallam (1968) and Dallam and Harpster (1968) reported push tests and beam tests undertaken with bolts embedded in the concrete. Marshall et al. (1971) undertook tests on embedded and post-installed bolts and, more recently, Kwon et al.

(2010) investigated the use of post-installed shear connectors under static and fatigue loading. However, none of those studies offered a complete understanding of the structural behaviour of concrete slabs in the bolted composite system, nor did they consider the issues of de-constructability. Lee and Bradford (2013a) and Lee and Bradford (2013b) examined in-detailed idea of bolted connectors in some push tests followed by an analytical model. The main focus of Lee and Bradford's tests is the level of composite action provided by the bolted shear connectors, however, the behaviour of concrete slab in such de-constructible systems has not been investigated which is one of the focus of this research project.

Chapter 3

Experimental Studies on Steel-Concrete Composite Decks with Precast RC Slabs: Behaviour of RC Slab

1. 3.1 Introduction
2. 3.2 Experimental procedure
3. 3.3 Testing (loading/unloading) procedure

3 EXPERIMENTAL STUDIES ON STEEL-CONCRETE COMPOSITE DECKS WITH PRECAST RC SLABS: BEHAVIOUR OF RC SLAB

3.1 Introduction

In this section, results of experimental tests on ten one-way half-scale precast RC slab strips that form part of a deconstructible composite bridge deck with different reinforcement arrangement and transverse restraints for steel girders are reported. The transverse restraints for steel girders are provided by using equal leg angle, $\mathrm{L}45 \times 45 \times 5EA$, as bracings and/or straps. The main objective is to investigate the behaviour of concrete slabs in the transverse direction (perpendicular to the direction of girders). Concrete slabs were casted in plywood formworks with minor defects occurred in the slabs due to warping of plywood formworks.

The steel girders used in these tests were Universal Beam $310UB40.4$ with $2100-mm$ long span. The tested concrete-steel composite sections represent composite bridge decks which typically have a span length of 1.5 m to 3.0 m based on Australian standards AS5100.5. Accordingly, a span length of 2.2 m was considered for the real bridge deck with a slab thickness of 200 mm which is consistent with minimum slab thickness requirements specified in Australian standards AS5100.5. Considering the standard specifications and owing to the available testing facilities at UTS structures laboratory the scale of ½ was selected for specimens. All these ten slabs were $1100-mm$ long, $600-mm$ wide, and $100-mm$ thick. This assures a span to depth ratio of 11 which is in the range of $10-15$ adopted by most of the bridge design codes. To connect the RC slab to steel girders, high-strength class 8.8 bolts were ordered. These bolts had a diameter of $16\,mm$ with a length of $150\,mm$, relevant nuts and washers were chosen for fastening the bolts. A pre-tensioning stress of approximately 360 MPa (equal to 40% of the bolt's ultimate strength) was induced in the bolts using torque meter wrench.

The main objective is to investigate the performance of the precast RC slabs in the bolted steel-concrete composite decks. Also, it is intended to evaluate the contribution of compressive membrane action in the ultimate loading capacity and failure mode of these precast slabs. To induce the CMA, two types of restraint were provided for the slabs;

1- X cross bracings

2- Horizontal straps

In addition, two dummy slabs were placed at the front and back of the steel girders (Figure 3-1). However, in the first four tests the contribution of these dummy slabs was found to be negligible. Accordingly, in the last six specimens these dummy slabs were removed. The configuration of samples and the test setup for two different set up (i.e. X cross bracings and straps) are shown in Figure 3-1.

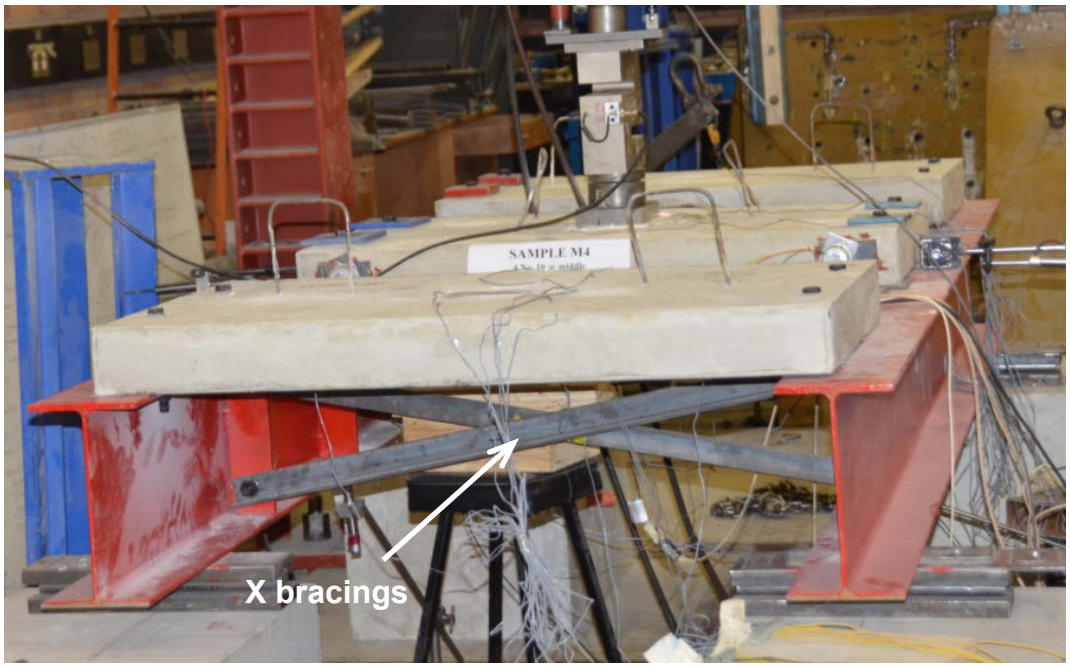

(a) Bracing with Dummies (samples 1-4)

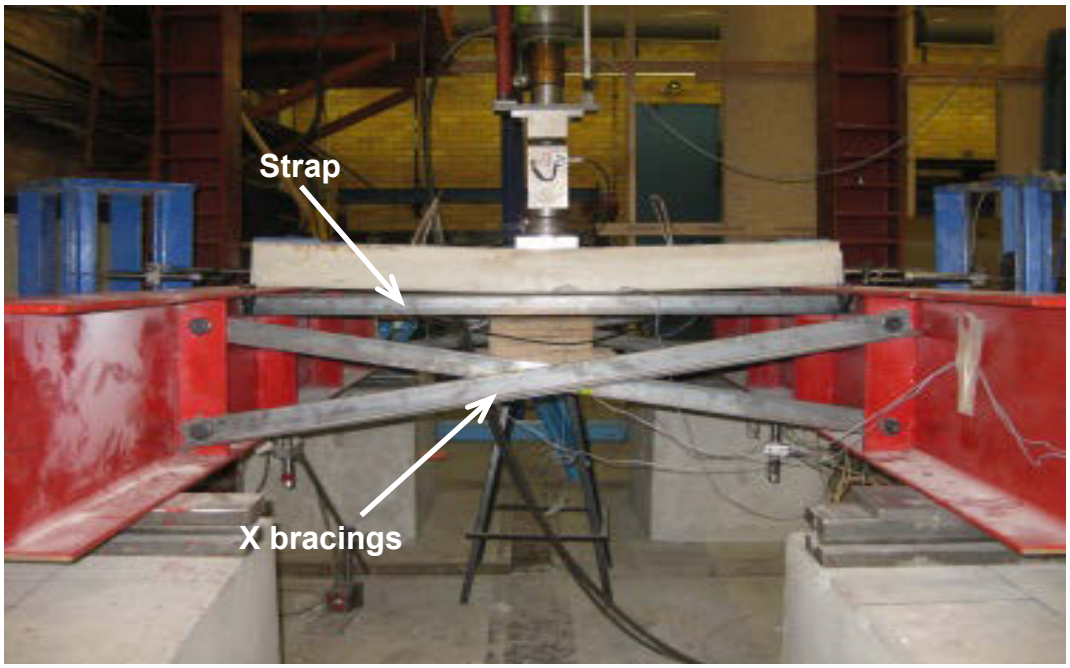

(b) Bracing with straps (samples 7-10)

Figure 3-1. Lateral restraining systems.

3.2 Experimental procedure

The following procedure was adopted for preparing and testing the specimens (Figure 3-2),

- Cutting plywoods

Plywoods were cut in specified dimensions to be used for building the formworks for concrete.

- Fabricating the formwork

Using the plywoods, ten $1100 \times 600 \times 100\ mm$ formworks were made for casting the slab strips.

- Drilling the moulds

To provide the holes in the slab for connection of girder and slab with high strength 8.8/FT bolts, a $20\ mm$ diameter hole was drilled in the moulds and a 20-mm PVC pipe was fixed in these holes before pouring the concrete.

- Sealing and oiling the moulds

To prevent the leakage of concrete mortar, corners of the moulds were sealed with silicon glue. At the same time, internal surface of the mould was oiled to provide a smooth surface for applying the load on the concrete decks and making the de-moulding job easier.

(a) Saw table for cutting the timbers

(b) Drill used for making holes in moulds

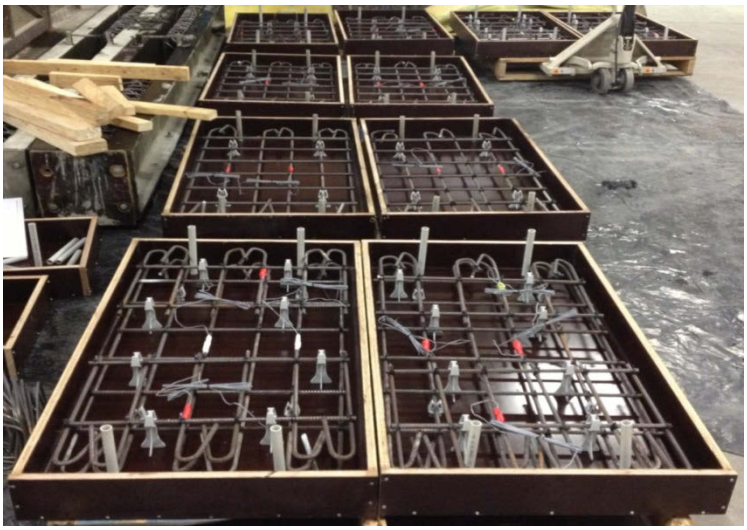

(c) All ten moulds with their located reinforcement mesh

Figure 3-2. Provision of the moulds for pouring.

- Cutting and bending of steel bar reinforcements (Figure 3-3)

After preparing the moulds, reinforcing bars were cut and bent according to (AS3600-2009) specifications. N10 reinforcing bars were used for preparing the steel meshes. A 180^{o} hook with diameter of $10d_b$ and an additional return length of $10d_b$ was used at the end of each longitudinal bar ($\boldsymbol{d_b}$ denotes the diameter of reinforcing steel bars).

(a) 50-tonne tensile test machine (b) Cutter (c) Bending utility

Figure 3-3. Steel processing apparatuses.

- Tensile tests on steel bars

Two sets of tensile tests on reinforcing steel bars were conducted and the mean value of yield strength (f_y) was determined, f_y= 684 MPa. A 50-tonne Universal testing machine was used for undertaking the uniaxial tension tests on the bars and ASTM A370-12a standard procedure was followed for preparation and uniaxial testing of the steel bars. The stress-strain diagram of steel bars obtained from uniaxial tension test is shown in Figure 3-4.

Table 3-1. Values of f_y from several Tensile test

	Test 1	***Test 2***	***Test 3***	***Test 4***
f_y (MPa)	704	689	658	6□6
			***Ave*:**	684 MPa

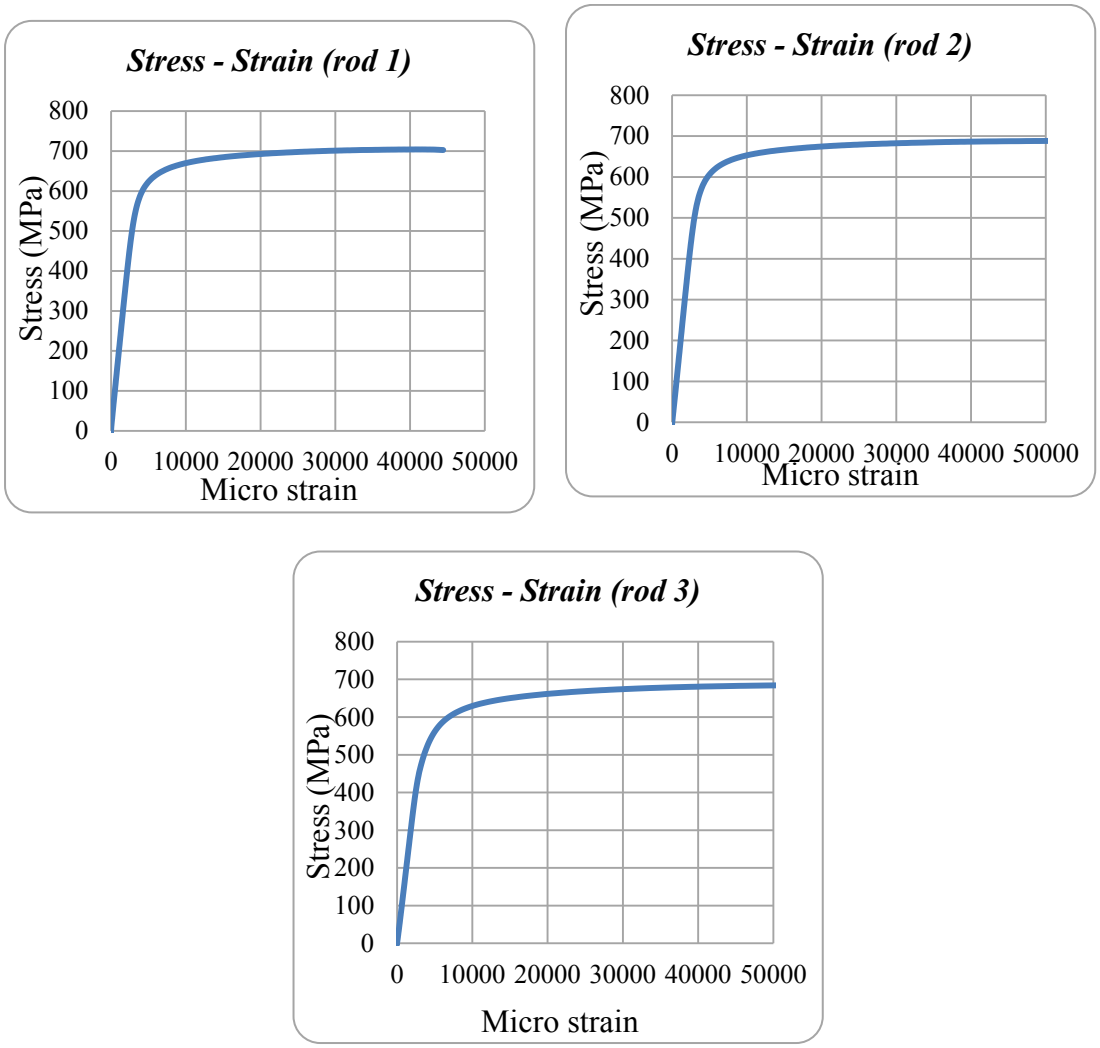

Figure 3-4. Uniaxial stress-strain diagram of reinforcing steel bars.

- Fabrication of the steel mesh

After cutting and bending the reinforcing steel bars to the desired length, the steel mesh were fabricated by the tying the steel bars as shown in Figure 3.4. In this study, four different sets of orthogonal reinforcing mesh with reinforcing proportion of $\rho =$ 0.5% and 0.8% (4 and 6 N10 bars, respectively, located in the middle and soffit of the slab) were considered. Figure 3-5 shows configuration of steel bars in different samples.

- Instrumentation of the specimens

Depending on the location of reinforcing mesh, $5-mm$ strain gauges were mounted on steel bars after grinding the bars (Figure 3-5). In various steps of the test, these strain gauges were tested to ensure that they work properly.

- Placing steel mesh in the mould using bar chairs and spacers

Bar chairs and spacers were used to provide the clear cover required on each side of the steel bars (Figure 3-5).

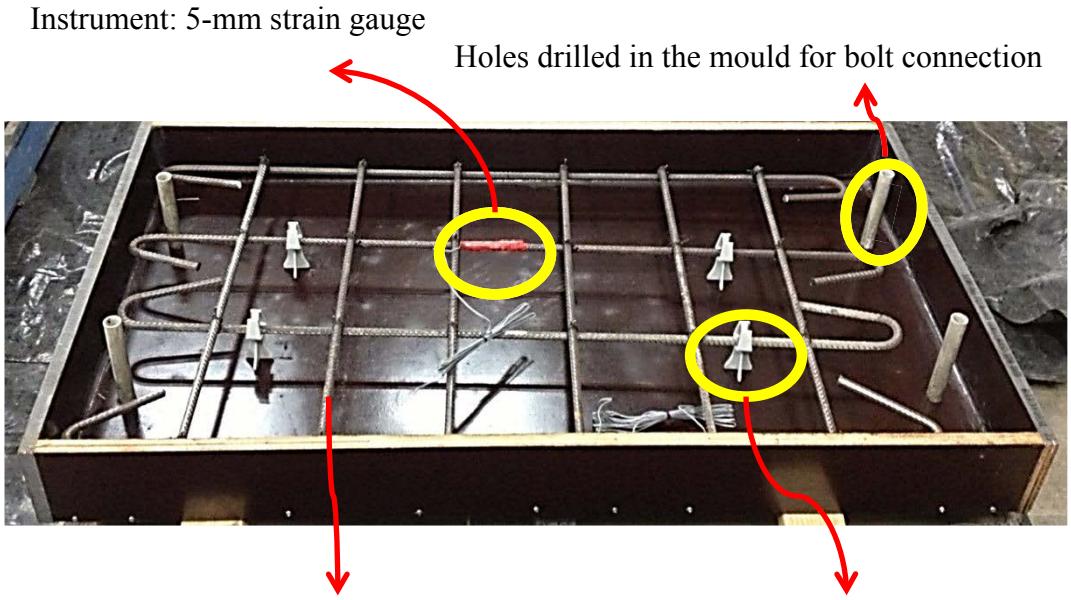

Figure 3-5. Fabrication and placing the reinforcing mesh in the mould .

- Pouring of concrete (Figure 3-6)

After placing the steel meshes in the moulds, the concrete was pouring in the moulds. A concrete mixture with nominal 28 day compressive strength of $f_c' = 32$ MPa, slump of 80 mm, and maximum aggregate size of 25 mm was used in all ten specimens. The concrete mixtures contained 20% fly ash as a replacement to Portland cement and accordingly the concrete continued to gain strength after 28 days and the compressive strength of concrete reached f_c'= 38 MPa on the testing day.

(a) Pouring of concrete

(b) Slump test

(c) Cylinders required for compressive test

Figure 3-6. Concrete pouring and slump test.

- Curing of concrete and de-moulding

All specimens were de-moulded after approximately 4 weeks.

- Concrete compressive test

In various occasions of curing and testing, uni-axial compressive tests on 300×150 mm cylinders were conducted using an Avery machine (Figure 3-7).

(a) Curing the concrete cylinders

(b) Compressive test Avery machine

Figure 3-7. Concrete Compressive test.

The compressive strength of concrete after 28 days was f_c'= 28 MPa, however, the concrete gained further strength over time and on the testing day the concrete compressive strength reached to 38 MPa.

Table 3-2. Values of f_c'

	Pouring	***28-Days***	***Test 01***	***Test 06***	***Test 09***
Day	30/07/2013	28 days	77 days	87 days	94 days
f_c' (MPa)		25	40	38	37
		31	□6	□9	36
		…	…	37	41
		…	…	….	39
Mean value (MPa)		28	38	38	38

- Instrumentation of specimens

Four 60 mm long concrete strain gauges were mounted on the soffit and top of the slab to measure compressive strain on the top-middle and bottom-edges of the concrete slab.

Table 3-3. Instrumentations on slabs

Position on slab	***Instrumentation type***	***Sample N□.***	
		1-7	***8-10***
Top side-1	60-mm strain gauge	✓	✓
Top side-2		✓	✓
Soffit, left		✓	…
Soffit, right		✓	…
Left side	Inclinometer	✓	✓
Right side	Inclinometer	✓	✓
Mid-span	LVDT	✓	✓

Two inclinometers were mounted on each end of the slab to measure the end rotations. The deflection at mid-span was monitored by means of a LVDT attached parallel to the loading ram (Figure 3-8).

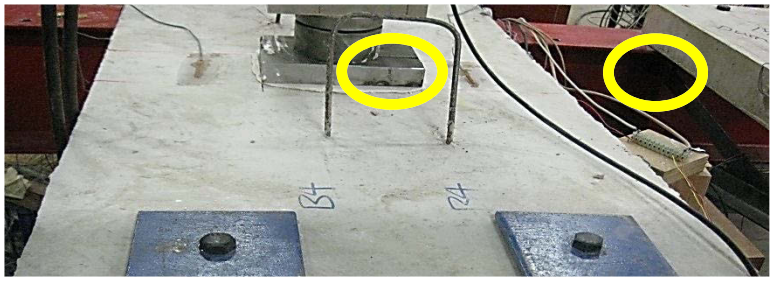

(a) Two 60-mm strain gauges

(b) Two Inclinometers

Figure 3-8. Instrumentation of the specimens.

Next phase of the experiment was to provide steel girders, X bracings, stiffeners, straps, and high strength bolts.

- Steel girders

Steel girders were cut to the specified length of 2700 mm, however, the beam length was limited to 2100 mm. The girders were made of universal beam 310UB40.4 as mentioned before. The steel beams were 310 mm deep and strong enough to ensure that the stress level remain well below the yield strength of steel during the test.

- Drilling the holes in the flange of steel girders (Figure 3-9)

The novel approach in connecting the RC deck slabs to steel girders through high-strength steel bolts required that some holes to be drilled in the top flange of the steel girders. Also, some of the holes drilled in the top flange of the girders were used for fastening the transverse straps to steel girders.

- Instrumentation of the steel girders

Three $5-$ mm long steel strain gauges were mounted on the web and flanges of each girder. Besides, two LVDTs were employed to measure the lateral drift and vertical movement of the steel girders (Figure 3-9).

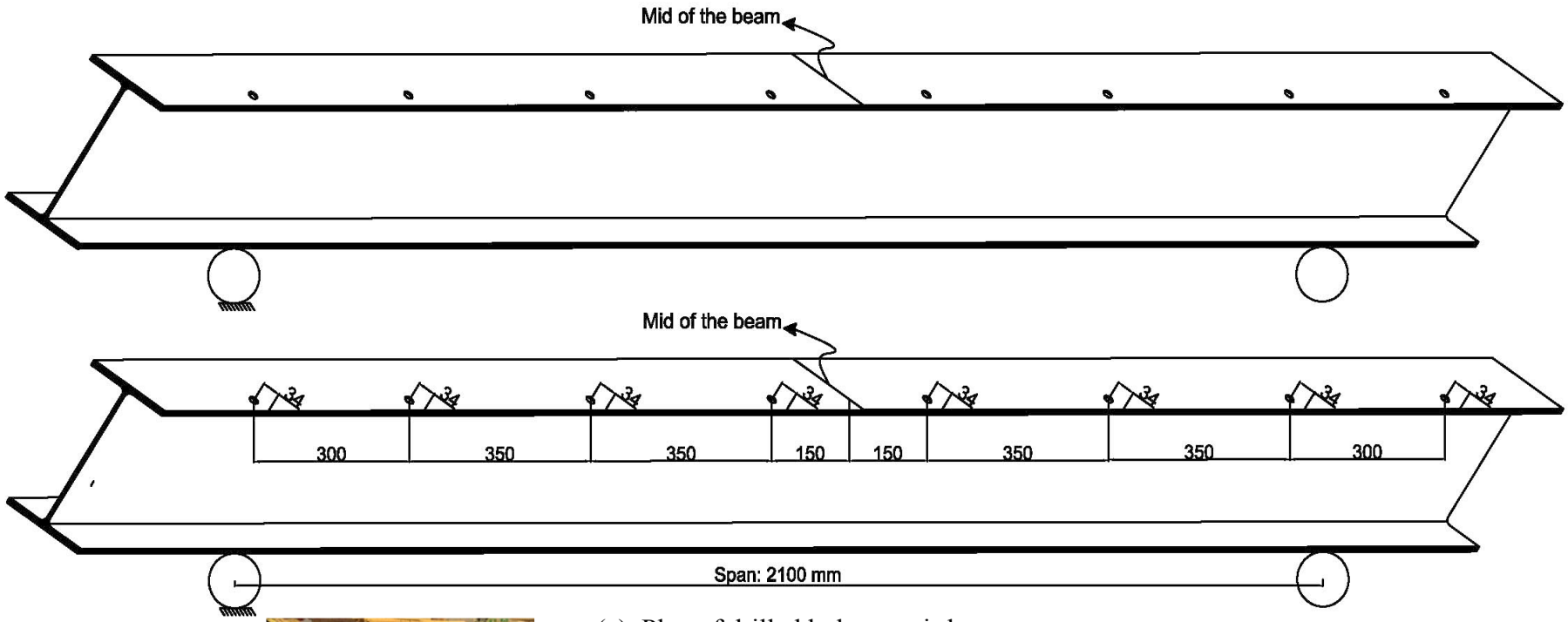

(a) Plan of drilled holes on girders

(b) Cutting girders

(c) Instruments on girders

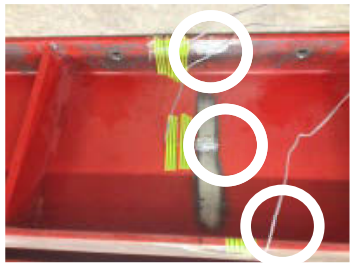

Figure 3-9. Preparation of the steel girders.

- Straps

One of the transverse restraints provided for the slabs was in the form of horizontal straps. Equal Leg Angles, L45X45X5EA were cut to the size and drilled at both ends.

- Instrumentation of straps

One 5-millimetre long steel strain gauge was attached to the middle of straps to measure the variation of axial strain in the straps. The axial strain in the straps will be used to determine the axial force developed in the straps during the test.

- Web stiffeners

Plates with thickness of 12 mm were cut and drilled to be used as stiffeners. These stiffeners were welded to the web and top flange of steel girders. Furthermore, these stiffeners provide the connection point for X cross bracings and horizontal straps.

- X cross bracings

Apart from horizontal straps, two X cross bracings were used to demonstrate the influence of lateral stiffness provided for the precast slab on the enhancement provided by CMA. The bracings were made of Equal Leg Angle, L45X45X5EA. The X cross bracings were bolted to the stiffeners using one high-strength 8.8 bolt with 16 mm diameter. These bolts were torqued up and a pre-tensioning stress equal to 40% of f_u was induced in these bolts.

- Instrumentation of bracings

One 5 mm long steel strain gauge was attached to the middle of each bracing to measure the axial strain in the bracings. This strain is used to calculate the axial force induced in each bracing.

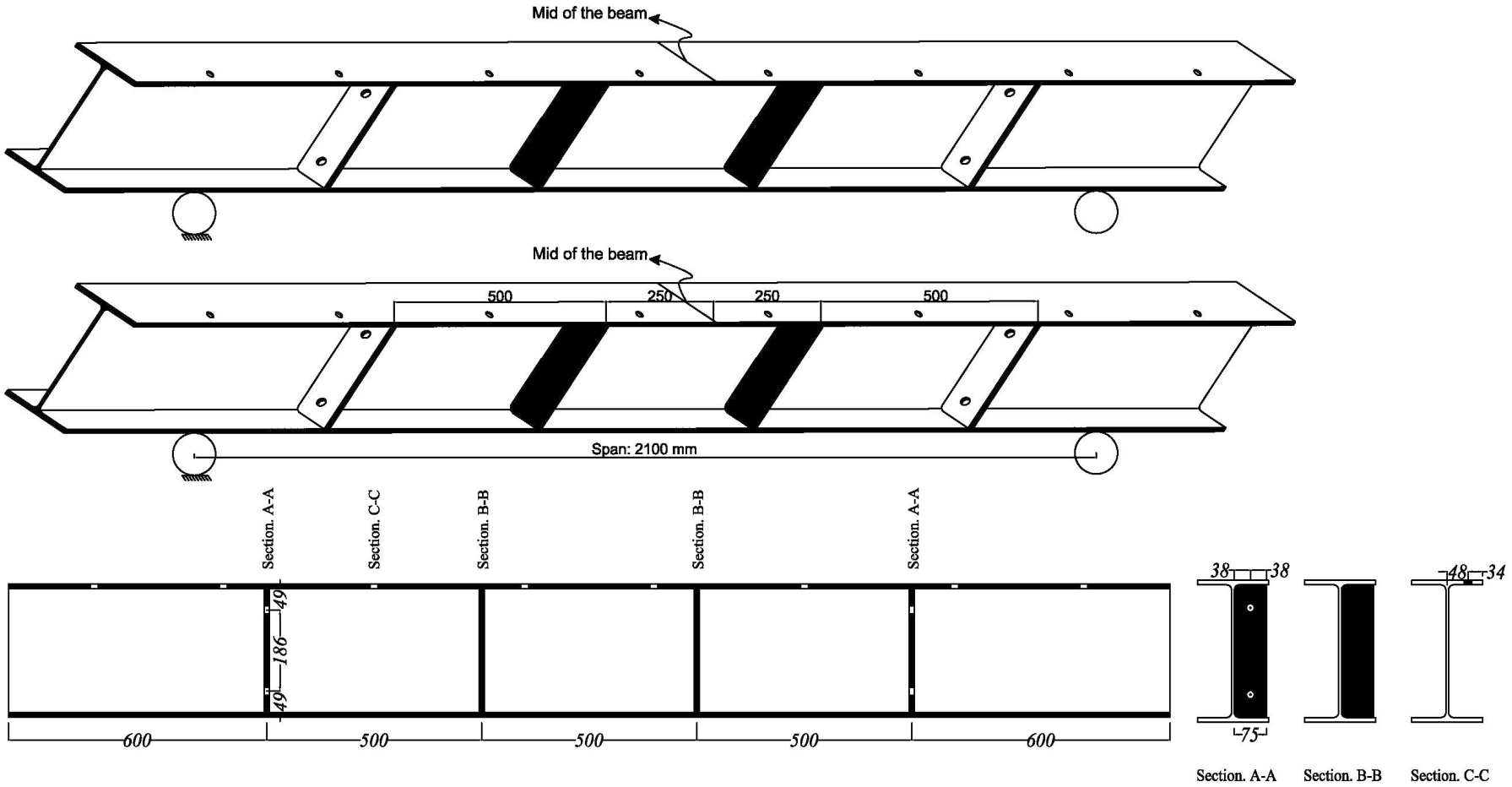

Figure 3-10. Configuration of the web stiffeners.

Following consideration were taken into account for using high-strength 8.8 bolts in the test setup:

- The mechanical characteristics of the bolts

Since the bolted shear connectors are of friction type, class 8.8/FT bolts were selected for this purpose. These bolts have an ultimate strength of $f_u = 800$ MPa and the yield strength of these bolts is about 80% of f_u, hence in this case, $f_y = 0.8 \times 800 = 640$ MPa.

- Tensile force in the bolts and the torque applied by torque meter wrench

Figure 3-11 depicts relationship between the torque applied on the bolt and the axial force induced in the bolt. Also, the most common methods for tightening up the bolts are summarised in Table 3-4.

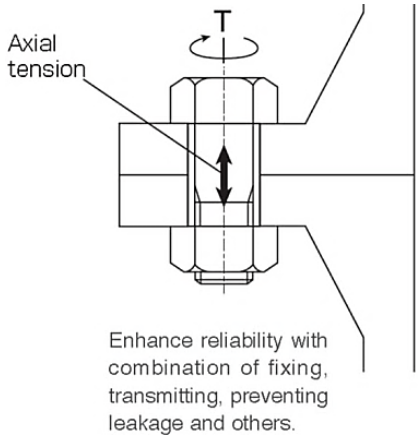

Figure 3-11. Torque vs induced pretensioing axial force in a bolt.

A pre-tensioning force of 65 kN was induced in the bolts that led to a tensile stress of $0.4f_u$. In the literature the relationship between the induced tensile force, F_t, in the bolt and the torque, T, applied by the wrench is, $T = 0.2 \times D \times F_t$ and a good correlation between this formula and the experimentally measured post-tensioning force in the bolts was observed in this study.

Table 3-4. Various tightening methods

Method	***Description***	***Advantages / disadvantages***
1. Torque control method	Bolt tightening is controlled by the torque value. This is the most widely used method.	Tightening control and operation is easy. Since the torque value does not change because of the bolt length, standardization is easy. The dispersion band of the axial tension is wide and bolt efficiency is low.
2. Rotation angle method	Bolt tightening is controlled by the angle. The bolt is tightened to a defined angle from the snug torque.	When bolts are tightened within the plastic zone, dispersion of axial tension is small and operation is easy. Since tightening will go beyond the yield point, there is a limitation on the threaded joint with additive load or retightening. It is difficult to define the tightening angle.
3. Torque gradient method	The bolt is tightened from the proportional point until the yield point is reached. An electronic circuit caries out arithmetic processing of the angle, torque, etc.	Since the dispersion width of the axial tension is small, the efficiency of the bolted joint is large. Inspection of the bolt itself is possible. Tightening will go beyond the yield point. The tightening device is expensive. In the service field, the tightening method is not available.
4. Elongation measurement method	Bolt tightening is controlled by the elongation of the bolt, generated by bolt tightening. Elongation is measured by micrometre, ultrasonically, or with a mandrel.	The dispersion of the bolt is very small. Tightening within elastic zone is available. The efficiency of the bolted joint is large. Additive loading and second-time tightening are possible. End face finishing of the bolt is required. The tightening cost is high.
5. Loading method	When the defined tensile load is applied to the bolt, tightening is controlled by the load given to the bolt.	Axial tension can be directly controlled. Torsion stress of the bolt is not generated. The tightening device and bolts are specially made. High cost.
6. Heating method	The bolt is heated to generate elongation. Tightening is controlled by the temperature.	Space and force are not required for tightening There is no clear relation between the heat and the axial tension. Temperature setting control is difficult.

Considering the available equipment at UTS structural laboratory and due to shortage of space, tightening of bolts performed by means of “Torque control method”. A wide

range of methods are available for tightening the bolts and each one of these tightening methods is applicable for a specific range of behaviour (i.e. elastic/plastic) for bolts (Figure 3-12).

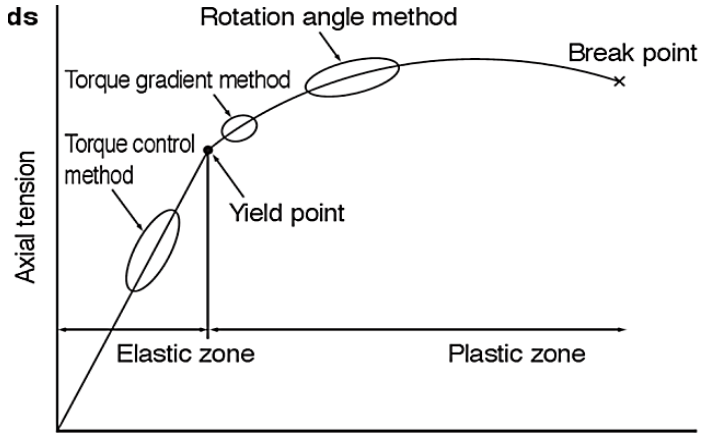

Figure 3-12. Various approaches of tightening the bolts and the corresponding range of induced axial force.

- Verifying the relationship between Torque (T) and tensile force (F_t), $T = 0.2 \times D \times F_t$

To ensure that this equation provides a good correlation between T and F_t, before tightening the bolts in actual tests, a simple test was carried out on a few bolts (Figure 3-13). In this simple test, $5-$ mm steel strain gauges mounted on the bolt shank and connected to the data acquisition. Two torque wrenches available in the lab were calibrated for applying 206 N. m torque that produces 65 kN post-tensioning force (40% of the bolts f_u) according to the above formula. The instrumented high-strength bolts were placed between two C channels (see Figure 3-13d) and tightened up using the calibrated torque meter wrenches. During the tightening process and after that the strain in the bolts was measured and the axial stress induced in the bolt was calculated using Hook's law and assuming an elastic modulus of $E = 200$ GPa for high strength steel bolts.

(a) Mounting strain gauges on bolts

(b) Placement of bolt in the channel

(c) Wrenches

(d) Connecting the instrument to data acquisition machine & tightening the bolts

Figure 3-13. Verifying the performance of torque metre wrench.

The results of torque wrench calibration on four different samples are given in Table 3-5. It is observable that both torque meter wrenches can induce the desired tensile force in the bolts with sufficient accuracy.

Table 3-5. Output of Wrench check-up test

	Wrench 1						***Wrench 2***	
Test	***Test 1***		***Test 2***		***Test 3***		***Test 4***	
strain (μ)	1553.99		882.63		1596.24		1586.85	
Unit	kN	% F_u	kN	% F_u	kN	% F_u	kN	% F_u
Theoretical Force (F_t)	64.34	40	32.17	20	64.34	40	64.34	40
Experimental Force (F_t)	62.49	38□9	35.49	22.1	64.19	39.9	63.81	39.7
Unit	N.m							
Theoretical Torque (T)	206		103		206		206	
Experimental Torque (T)	199.96		113.57		205.40		204.19	
Ratio (Exp/The)	0.97		1.1		1.0		0.99	

- Push-out test

Push out test is required to characterise the load-slip behaviour of shear connectors including bolted composite connections. In this study, no push out test has been conducted yet; however, two push-out tests will be done in near future to determine the mechanical characteristic of the frictional connection between concrete slab and steel girders. The results of push-out tests are employed to characterise the contact element between concrete and steel in the finite element (FE) models. Figure 3-14 shows the outline of the specimens to be used in push-out tests. In the absence of load-slip data, the results of push-out tests undertaken by Lee and Bradford (2013a) are used for characterising the contact elements in the FE models.

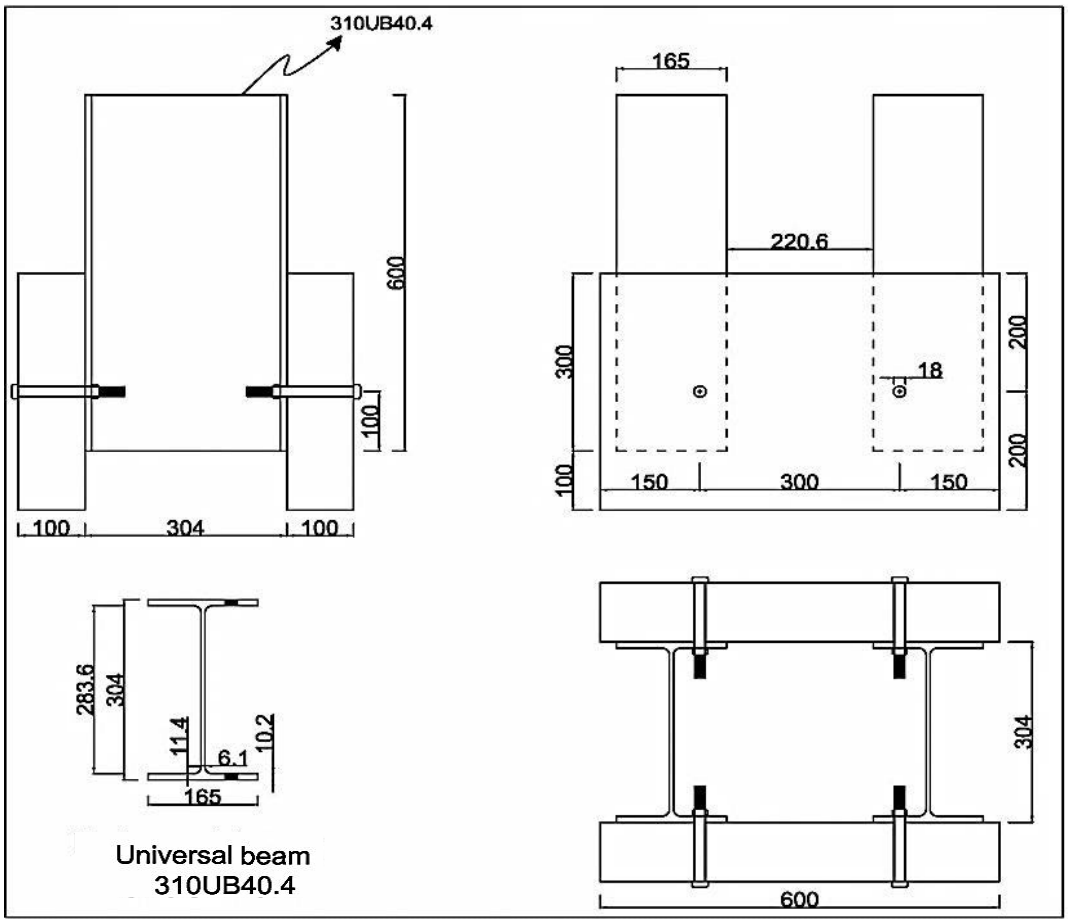

Figure 3-14. Details of the specimens in the push-out tests.

- Levelling the supporting blocks and steel girders

The test setup typically needs to be adjusted with respect to the adopted construction tolerances. One of the issues that require adjustment of test setup is related to levelling of the steel girders with sufficient accuracy.

- Placement of the steel girders on the testing rig

Test set-up was made up of two steel girders, one main concrete slab and two dummy slabs (which were removed after the first four tests because the effect of dummy slabs on the response of the restrained slab strips was found to be negligible). Two X cross bracings were used in 8 samples and horizontal straps in 5 samples.

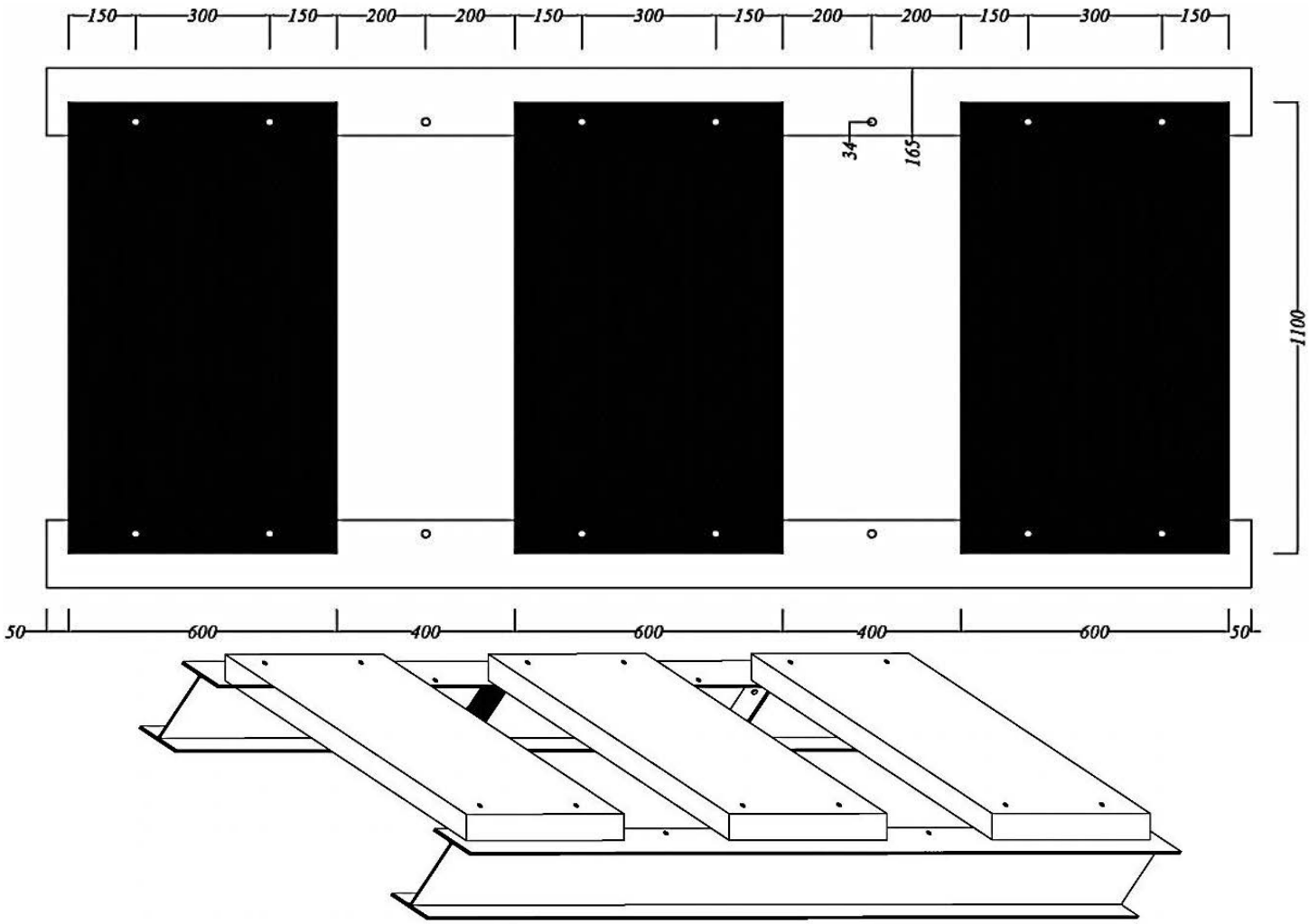

Figure 3-15. Configuration of slab (samples No. 1-4).

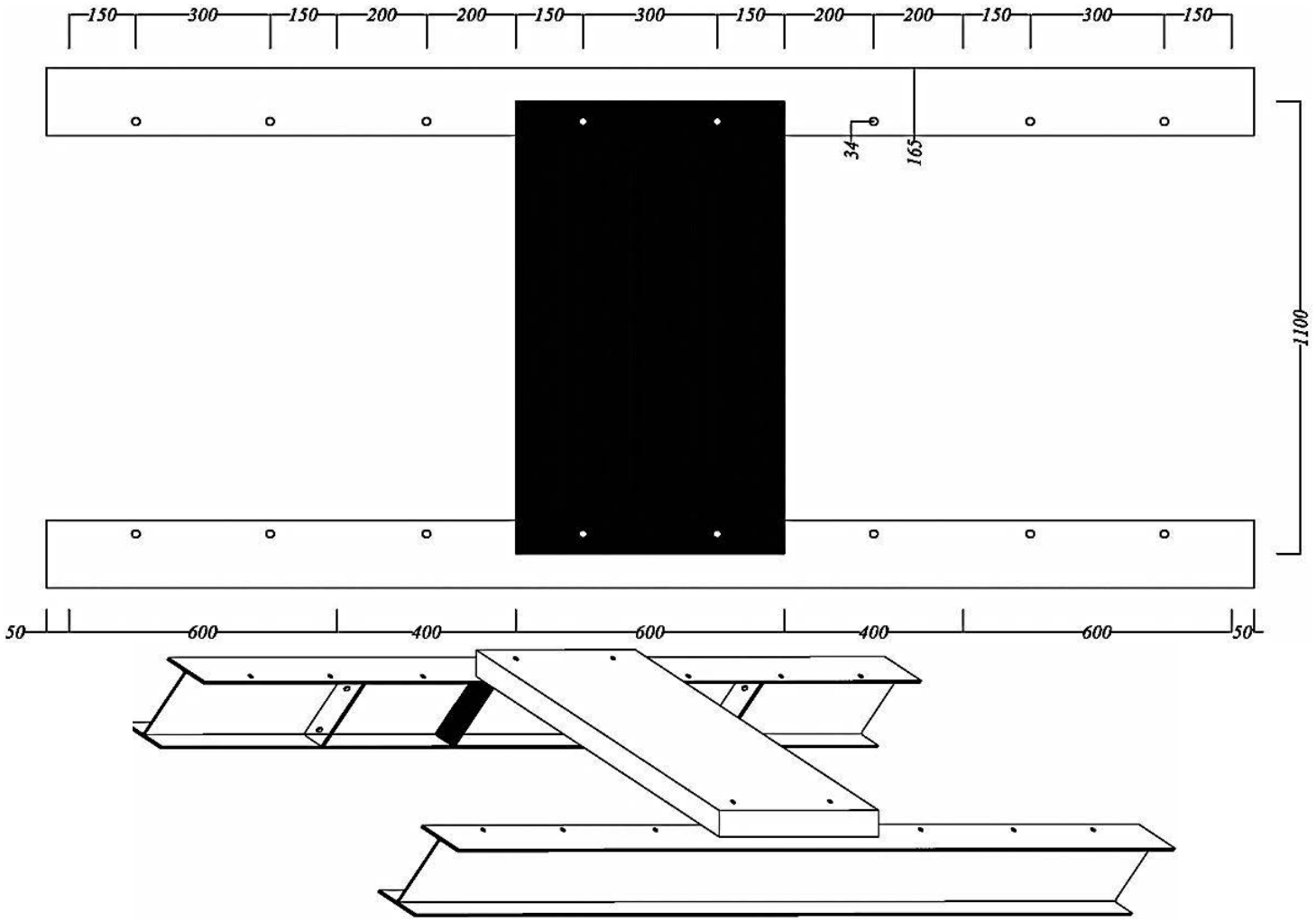

Figure 3-16. Configuration of slab (samples No. 5-10).

- Assembling the hydraulic jack, load cell, spherical seat and loading plate and the data acquisition (Figure 3-17).

A hydraulic jack was used to push-down the loading ram and apply the displacement controlled load on the restrained slab strips.

A $30-$ tonne S-shaped load cell was used in this test and for all ten samples a loading rate of 0.05 mm/sec was adopted.

A rectangular 200×125 mm plate with 30 mm thickness was used to simulate half a standard wheel according to Australian standard, ***AS 5100.1-2004: Bridge design code***.

A spherical seat was placed between the load cell and loading plate to allow for possible rotation associated with mid-span deflection.

A displacement-controlled loading regime was employed and the load applied on the slab was monitored by the load cell.

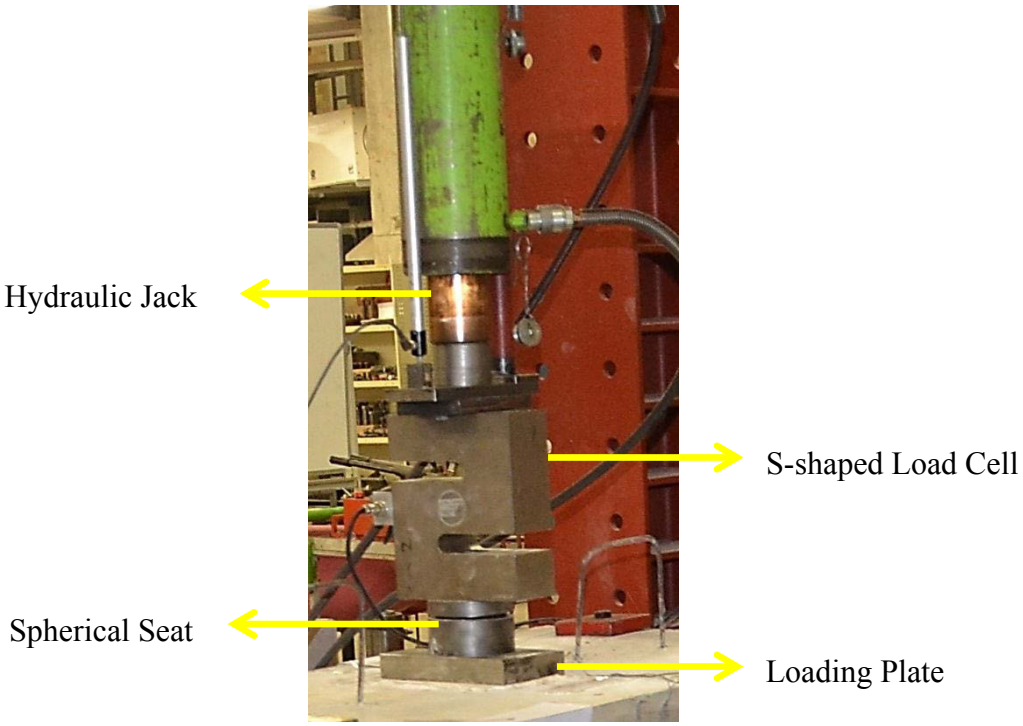

Figure 3-17. Loading equipment.

3.3 Testing (loading/unloading) procedure

As mentioned earlier, ten one-way slabs (slab strips) with various lateral fixities were tested. Samples were monotonically loaded up to the rupture of reinforcing bars followed by failure of the slab. Mainly the failure of samples was associated with formation of wide cracks running between two bolts and parallel to girders. Also, major crushing of concrete occurred under the loading plate at the mid-span. The LVDT mounted on the loading ram and placed at mid-span (Figure 3-17) monitored deflection of the samples at mid-span. Rotation of the two ends of the samples was recorded by means of two inclinometers. To provide more detailed benchmark data required for verification and calibration of FE models, 3 strain gauges were mounted on each girder, i.e. on top and bottom flanges and at the middle of the web. In all ten specimens, these six strain gauges reported strains within elastic range of steel behaviour which were negligible. Except specimen No. 5 (with no transverse strap and X cross bracings), in the rest of the specimens no major tilting was observed in the girders. The details of reinforcing proportion and steel bar configurations in all 10 specimens are shown in Table 3-6 and Figure 3-18.

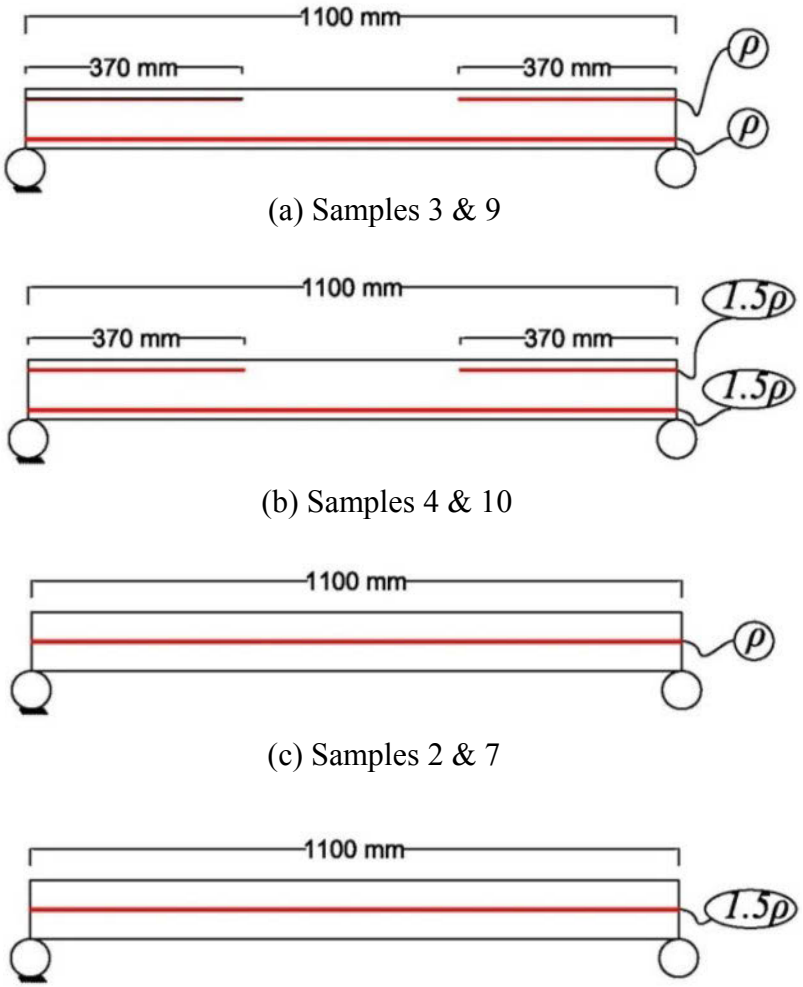

Figure 3-18. Reinforcement arrangements in various samples.

The parameters considered and monitored within each test are as below;

- ✓ Ultimate loading capacity of the RC slab strips
- ✓ Mode of failure
- ✓ Effect of lateral restraint and stiffness on the ultimate loading capacity
- ✓ Mid-span deflection of the specimens
- ✓ Effect of reinforcing bar arrangements

- ✓ Behaviour of steel girders
- ✓ Performance of high strength bolts as shear connectors
- ✓ Structural response of straps and X cross bracings as well as the enhancement provided by development of compressive membrane (arching) action

No sign of bending or deformation was observed in the high strength bolted shear connectors even at the ultimate stages of loading. Depending on the reinforcing proportion and configuration and the provided transverse stiffness (i.e. X cross bracings and/or transverse straps), different specimens showed different ultimate loading capacity. Table 3-6 summarises the specimen names, bar configuration and transverse stiffnesses for each specimen. The ten specimens are divided into two categories with respect to the provided transverse stiffness; specimens No. 1 to 4 with X cross bracings only and specimens No. 7 to 10 with X cross bracings and horizontal straps. Specimen No. 5 has no transverse stiffness and in specimen No. 6 only horizontal straps were used.

To evaluate the structural behaviour of transverse restraining systems and supporting steel girders, the strains from strain gauges mounted on the steel girders, transverse straps and X bracings were regularly acquired throughout the test. The strains induced in the transverse X cross bracings and straps were small and within the elastic range of steel behaviour. The supporting steel girders exhibit neither considerable axial strain nor horizontal/vertical deflections. In addition, the concrete strain gauges attached to the soffit of the slab adjacent to the steel girders recorded negligibly small strains. In the following section the experimental results of different specimens are presented in full details.

Table 3-6. Specimen names, bar configuration and transverse stiffnesses

		Rebar arrangement								***Lateral system***		
Sample	***f'_c (MPa)***	***Rebar No.***	***ρ (%)***	***d (mm)***	***Clear cover (mm)***	***f_y (MPa)***	***Side cover (mm)***	***Reinforcing layers***	***Bar Spacing (mm)***	***Bracing****	***Dummy slabs***	***Strap****
M6B	38	10	0.79	50	45	684	20	1@ middle	112	✓	✓	…
M4B	38	10	0.52	50	45	684	20	1@ middle	187	✓	✓	…
B4B	38	10	0.52	75	20	684	20	2@ bottom & $1/3$ top edges	187	✓	✓	…
B6B	38	10	0.79	75	20	684	20	2@ bottom & $1/3$ top edges	112	✓	✓	…
M6SS	38	10	0.79	50	45	684	20	1@ middle	112	…	…	…
M6S	38	10	0.79	50	45	684	20	1@ middle	112	…	…	✓
M4BS	38	10	0.52	50	45	684	20	1@ middle	187	✓	…	✓
M6BS	38	10	0.79	50	45	684	20	1@ middle	112	✓	…	✓
B4BS	38	10	0.52	75	20	684	20	2@ bottom & $1/3$ top edges	187	✓	…	✓
B6BS	38	10	0.79	75	20	684	20	2@ bottom & $1/3$ top edges	112	✓	…	✓

* Cross section area of the equal angles, $45 \times 45 \times 5$EA , was 394 mm^2.

3.3.1 Sample M6B

This specimen with six N10 bars at the mid-level of the slab ($\rho = 0.79\%$), represents a case of heavily-reinforced slab with only one layer of reinforcement. As the load is gradually increased, the first cracks appear on the soffit of the concrete slab at the mid-span (Figure 3-19a) followed by hair cracks around the bolted shear connectors (Figure 3-19b). These cracks are initiated due to stress concentration and eventually give way to wide cracks running between two adjacent bolts (Figure 3-19c).

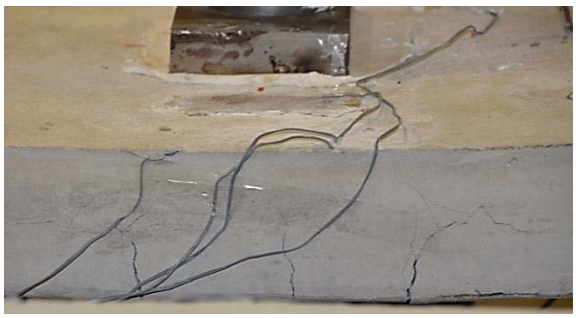

(a) Formation of flexural cracks

(b) Initial cracks around the bolt

(c) Connection failure accompanied by crushing of concrete

Figure 3-19. Structural response of sample M6B.

The major cracks running between two adjacent bolts (Figure 3-19c) developed at a load of 89.3 kN causing a sharp drop in the load-deflection diagram (Figure 3-20). After this drop in the load, the specimen did not fail completely and it gained some strength and continued to carry the load until extensive crushing of concrete at the mid-span deflection of 2.7 mm took place (Figure 3-20). Development of compressive membrane action in the specimen enhanced the loading capacity and finally at a deflection of 24.2 mm the CMA reached its peak.

The mid-span deflection of slab corresponding with the 1^{st} and 2^{nd} peak loads (Figure 3-20) are 18.8 and 24.2 mm, respectively, however, the deflection of supporting girders are 1.6 and 1.2 mm. The maximum relative lateral movement of girders in the horizontal direction (ultimate elongation of the RC slab) is1.8 mm. Rotations of slab recorded at each end have a near linear relationship with mid-span deflection. The end rotations reached 2.5 and 3.0 degrees at the peak load.

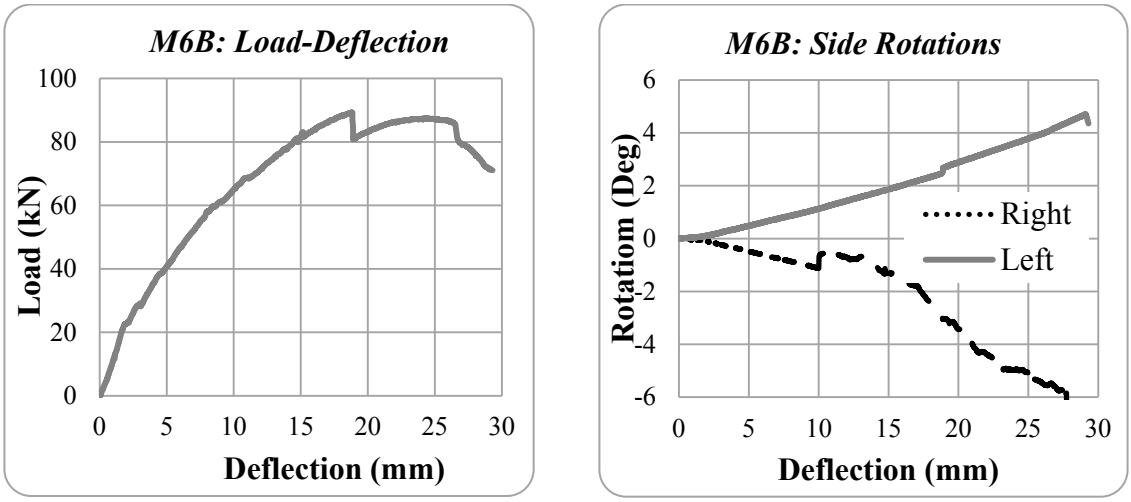

(a) (b)

Figure 3-20. (a) Load-deflection and (b) rotation-deflection graphs for specimen M6B.

3.3.2 Sample M4B

In this sample, four N10 rebars were placed in one layer at the mid-height of slab thickness providing a reinforcing proportion of $\rho = 0.52\%$. This specimen represents a

moderately-reinforced slab strip. Specimen M4B exhibited the same crack pattern and behaviour as M6B (Figure 3-21). The CMA was mobilised in this specimens owing to provided transverse restraints. This specimen reached a peak load of $69.8\,kN$ at displacement of $15.0\,mm$. The pattern of cracks and the compressive thrust for this specimen are outlined in Figure 3-21.

(a) (b)

Figure 3-21. Structural response of sample M4B; (a) Connection's rupture, (b) Arching thrust & concrete's crushing.

The 1^{st} and 2^{nd} peak of loading occurred at mid-span displacement of 15.0 and $20.8\,mm$, respectively. The maximum vertical deflection of supporting steel girders are 1.5 and $1.0\,mm$. Also, the maximum relative movement of the steel girders was $1.9\,mm$ in the sideway direction. Figure 3-22 shows the load versus mid-span deflection and end rotation versus mid-span deflection of the specimen M4B. It is observable that inclinometers captured the end rotations that have a nearly linear relationship with mid-span deflection (Figure 3-22).

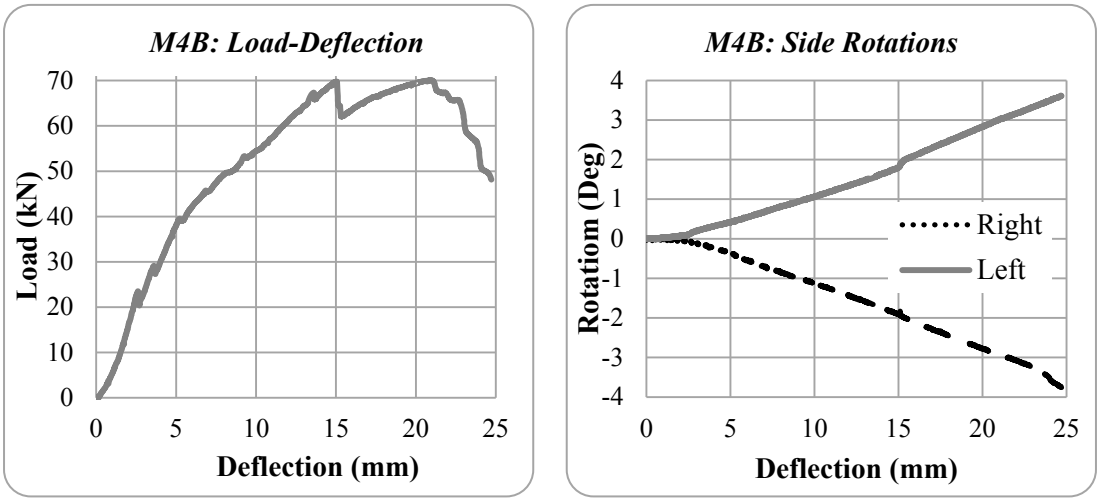

(a) (b)

Figure 3-22. (a) Load-deflection and (b) rotation-deflection graphs for specimen M4B.

3.3.3 Sample B4B

This sample had the same reinforcing ratio as M4B (i.e. $\rho = 0.52\%$) but the reinforcing bars were placed on the bottom of the slab. The structural response and mode of failure of M4B was similar to M6B and M4B specimens (see Figure 3-23).

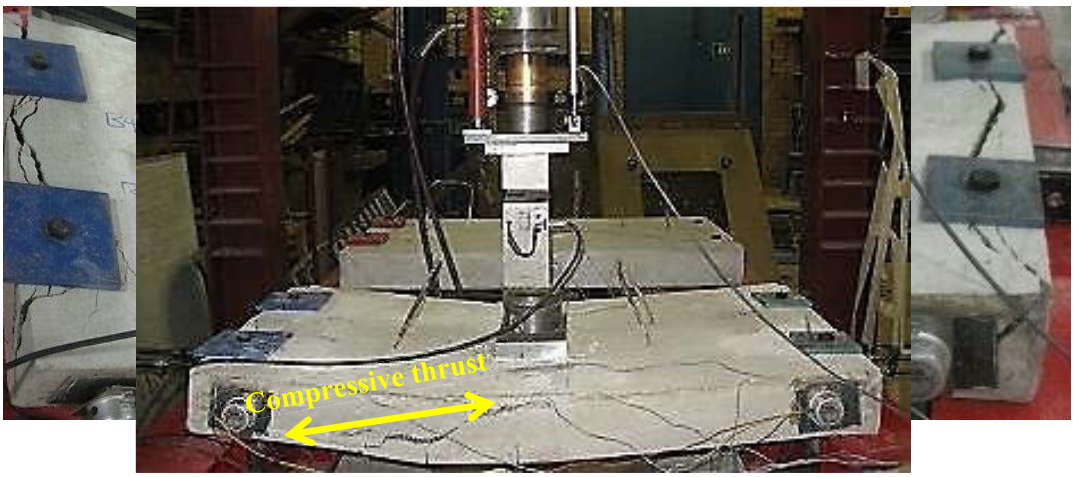

Figure 3-23. Structural response of sample B4B (Cracks between holes, large deflection and distortion, and formation of arching thrust).

The first peak load of this specimen was 107.9 kN occurred at deflection of 16.5 mm. The cracks developed around the bolts led to a sharp drop in the load-deflection response. The second peak load was 103.6 kN and occurred at mid-span deflection of 19.5 mm (Figure 3-24). Comparing the peak load of specimen B4B with M4B, a 55% increase in the loading capacity was observed by only changing the location of reinforcements from mid-height to the bottom of RC slab. However, the ductility and failure mode of the specimen B4B was similar to M4B and M6B specimens.

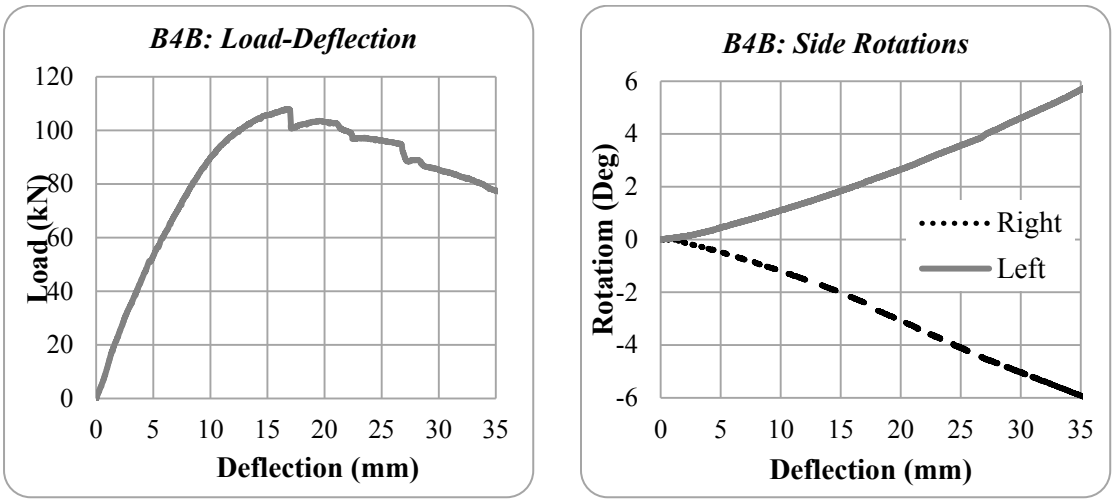

(a) (b)

Figure 3-24. (a) Load-deflection and (b) rotation-deflection graphs for specimen B4B.

The vertical displacement of steel girders was small compared with the mid-span deflection of the slab. The maximum relative movement of steel girders in the lateral direction was (ultimate elongation of the RC slab) 2.5 mm. The nearly linear relationship between end rotations and mid-span deflections is shown in Figure 3-24.

3.3.4 Sample B6B

Specimen B6B had steel ratio of $\rho = 0.79\%$ with the same reinforcing bar configuration as B4B. Although this sample had similar mode of failure as 3 previous ones, but the ultimate loading capacity of this specimen was 58% higher than other

specimens. The 1st and 2nd peak load for this specimens were 141.1 and 136 kN, respectively.

Figure 3-25. Structural response of specimen B6B.

The deflections corresponding with the peak loads were 22.4 and 19.5 mm (Figure 3-26). The maximum relative transverse movement of the steel girders was 2.4 *mm* that is within the same range as previous specimens. As shown in Figure 3-26, the end rotations of the specimen were 2.8 and 3.1 degrees at the maximum load.

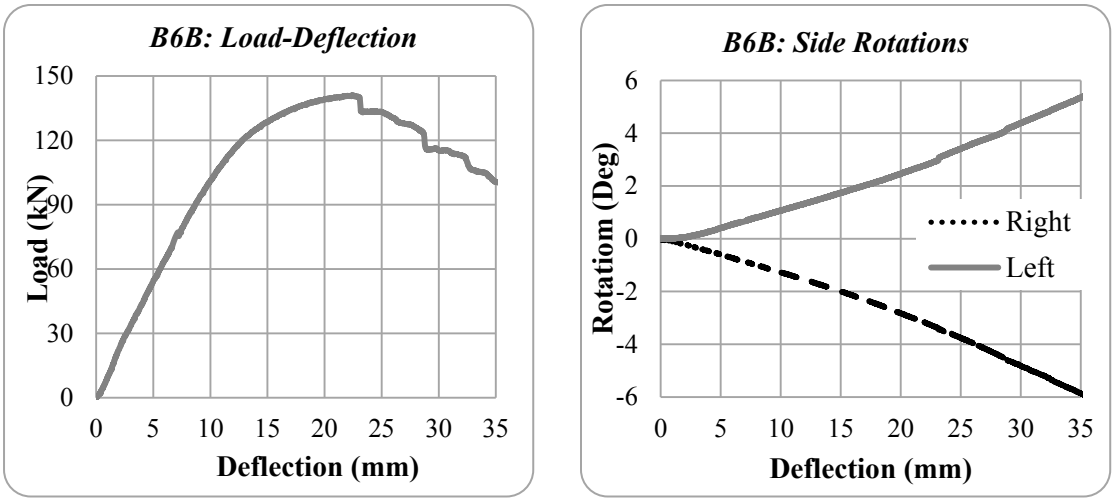

(a) (b)

Figure 3-26. (a) Load-deflection and (b) rotation-deflection graphs for specimen B6B.

3.3.5 Sample M6SS

Specimen M6SS was designed to simulate the behaviour of a slab on steel girders with no restraint in the transverse direction. Accordingly, no transverse X cross bracing or strap was provided for the slab. The slab had a reinforcing proportion of $\rho = 0.79\%$. This specimen behaved differently from 4 previous samples in that, only some minor cracks developed in the vicinity of bolted shear connections and mode of failure for specimen M6SS was basically associated with yielding of reinforcing steel bars followed by crushing of compressive concrete at the mid-span as shown in (Figure 3-27).

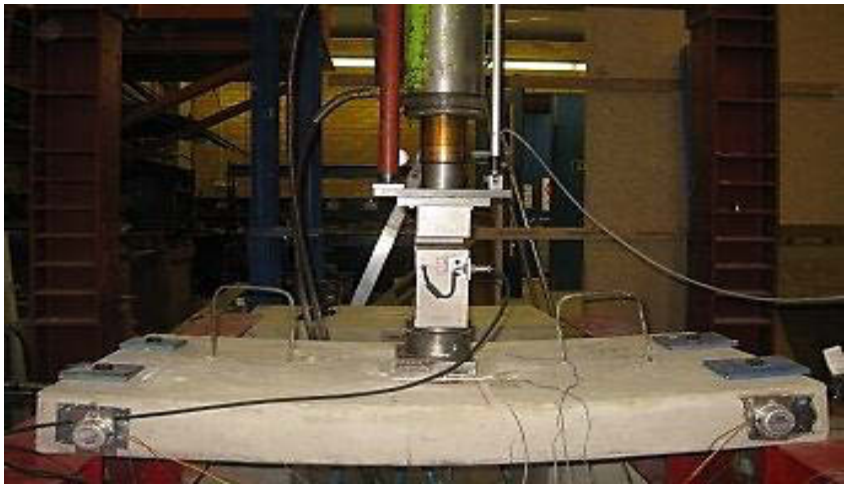

Figure 3-27. (a) Load versus deflection and (b) rotation versus deflection for specimen M6SS.

For specimen M6SS the peak load is 68 kN and occurred at mid-span displacement of 24.3 mm (see Figure 3-28). Relative lateral movement of steel girders was larger compared with previous tests as 4.6 mm, but negligible. Rotations of sample sides were 2.8 and 3.6 degrees in max load (Figure 3-28).

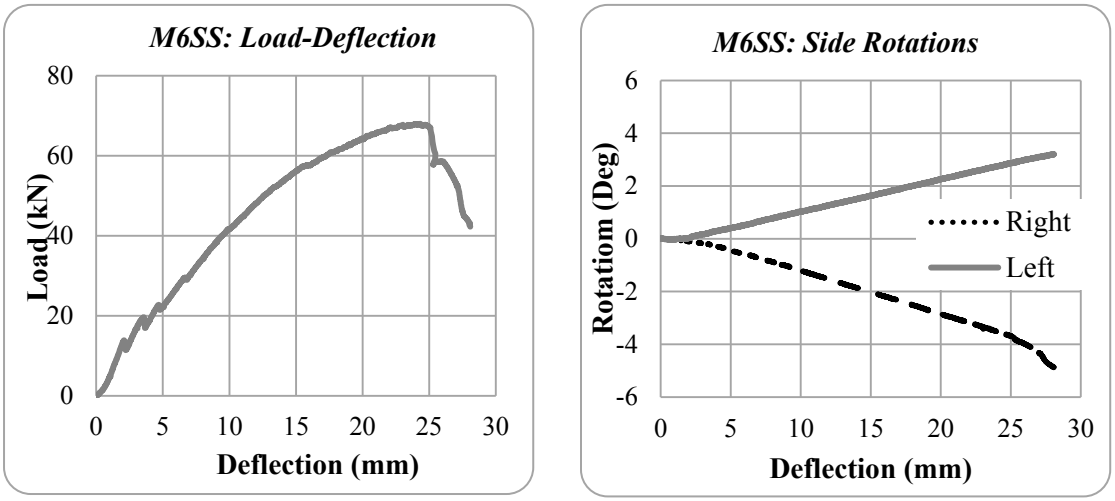

(a) (b)

Figure 3-28. (a) Load-deflection and (b) rotation-deflection graphs for specimen M6SS.

3.3.6 Sample M6S

In order to evaluate the effect of transverse straps on the lateral stiffness and loading capacity of the slabs, specimen M6S was tested with only straps provided for the specimen. The reinforcing proportion and configuration for specimen M6S was similar to M6B, except that in M6S specimen, only straps were used whereas in M6B only X cross bracings were used. Looking at below pictures, it can be concluded that M6S had the same structural response as M6B, but mode of failure was different. M6S failed due to yielding of reinforcement followed by crushing of concrete (Figure 3-29).

Figure 3-29 Structural response of specimen M6S.

The first peak load of 88.7 kN and second peak load of 87.8 kN were observed at mid-span displacements of 23.3 and 25.0 mm, respectively (Figure 3-30). The relative lateral movement of steel girders (elongation of RC slab at ultimate state) was quite small (1.3 mm), showing the effectiveness of straps to provide lateral restraint for slabs. The maximum rotation occurred at each end of the sample corresponding to peak load was about 3 degrees (Figure 3-30).

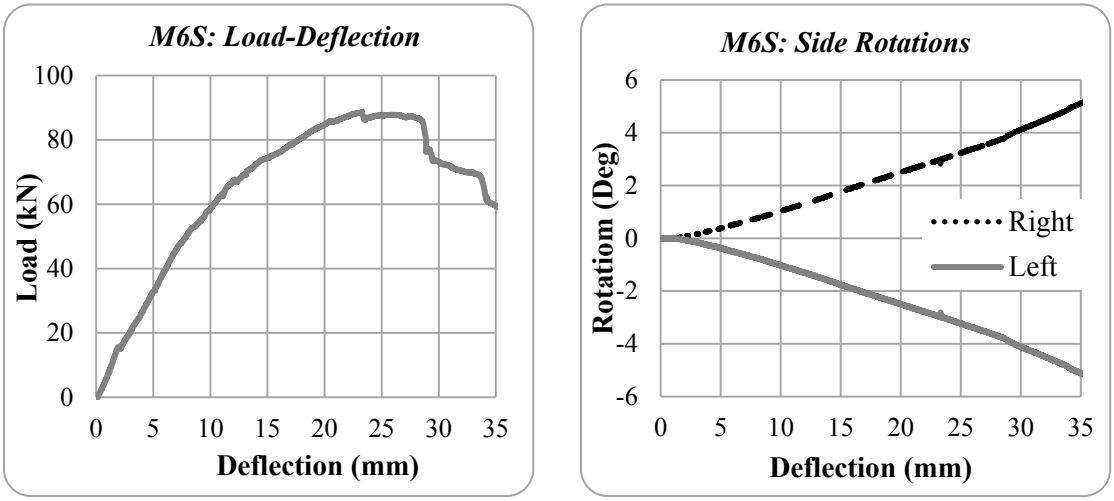

(a) (b)

Figure 3-30. (a) Load-deflection and (b) rotation-deflection graphs for specimen M6S.

3.3.7 Sample M4BS

The transverse stiffness in specimen M4BS was provided by both horizontal straps and X cross bracings. Compared with sample M4B which only had X cross bracings, specimen M4BS had higher loading capacity (around 21% higher) owing to larger CMA force. Having 1st and 2nd peak load of 84.1 and 75.6 kN at mid-span deflection of 23.9 and 25.0 mm, this sample showed the same structural response and mode of failure as specimen M4B.

Figure 3-31. Structural response of specimen M4BS.

The load versus mid-span deflection of specimen M4BS is shown in Figure 3-32. The relative movement of the steel girders in the transverse direction (elongation of RC slab) in specimen M4BS was relatively small (only1.3 mm) compared with specimen M4B (relative transverse movement of 1.9 mm). Rotations of slab end points were about 3 degrees at the peak load.

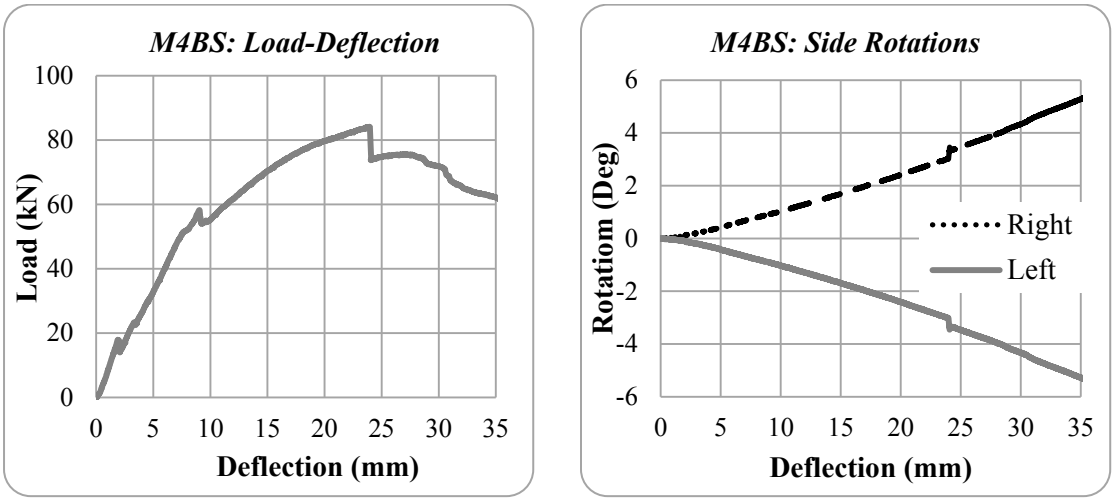

(a) (b)

Figure 3-32. (a) Load-deflection and (b) rotation-deflection graphs for specimen M4BS.

3.3.8 Sample M6BS

Alike M4BS, sample M6BS failed due to major cracks developed in the proximity of bolted shear connectors (Figure 3-33). The maximum loading capacity of the specimen was 102.7 kN at the displacement of 25.42 mm (Figure 3-34).

Figure 3-33. Structural response of sample M6BS.

Both specimens M6B and M6BS had the same reinforcing bar proportion and configuration, however, the peak loading capacity of M6BS was 15% higher than M6B. As shown in Figure 3-34b, at peak load the maximum rotation at the end of slab and the maximum relative movement in the transverse direction were approximately 3 degrees and 1.3 mm, respectively. Accordingly, the horizontal straps proved to be effective in providing longitudinal restraint to the slab and accordingly inducing CMA in the RC slab.

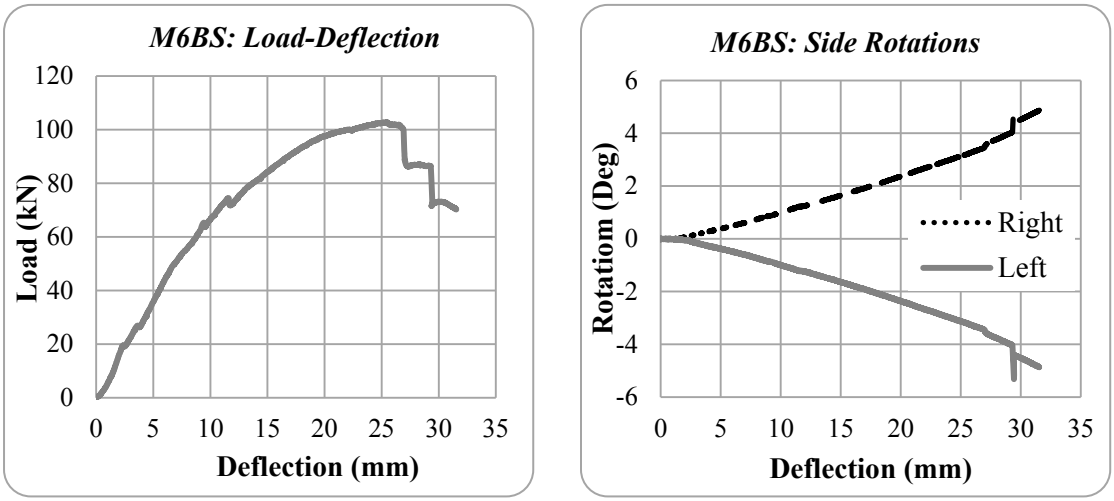

(a) (b)

Figure 3-34. (a) Load-deflection and (b) rotation-deflection graphs for specimen M6BS.

3.3.9 Sample B4BS

This specimen had both X cross bracing and strap and it showed the same behaviour as M6SS and M6S in that, it failed due to yielding of steel bar accompanied with crushing of concrete. Apart from some minor cracks, no major crack was observed in the proximity of bolted shear connectors (Figure 3-35).

Figure 3-35. Structural response of sample B4BS

The peak loading capacity of specimen B4BS was 114.0 kN (Figure 3-36) which is around 6% higher than specimen B4B (with only X cross bracing). The rotation at peak load recorded at the end of the slab was 3 degrees and the maximum relative transverse movement of steel girders was 3.6 mm. This value was slightly higher than what was expected that can be attributed to some relaxation occurred in the straps or cross bracings. Initial expectation was that the peak load of B4BS would be much larger than B4B. However, the relatively low compressive strength of concrete didn't allow for full development of the CMA, even with fairly large lateral stiffness provided for the slab.

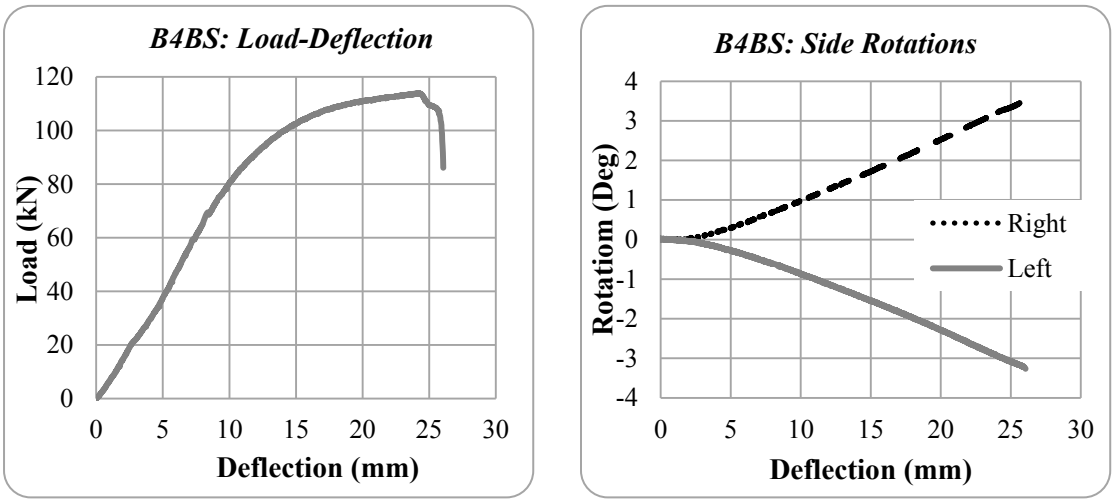

(a) (b)

Figure 3-36. (a) Load-deflection and (b) rotation-deflection graphs for specimen B4BS.

3.3.10 Sample B6BS

The failure of this specimen was associated with major crushing of concrete as shown in Figure 3-37. The specimens M6SS, M6S, B4BS and B6BS behaved similarly in that, all of them failed due to concrete crushing with no sign of major cracks running between two adjacent bolted shear connectors.

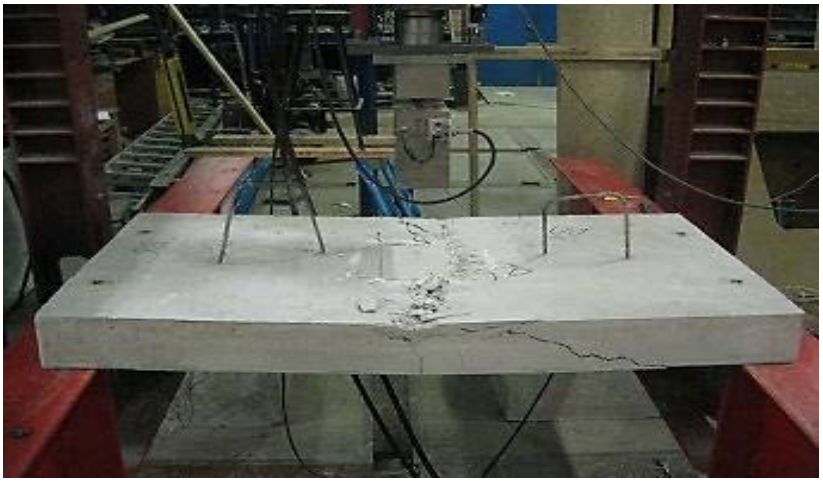

Figure 3-37. Structural response of sample B6BS.

The peak load for this specimen was 136.6 kN that was almost the same as peak load of sample B6B (Figure 3-38). Similar to specimen B4BS and despite very stiffness transverse restraints (X cross bracing and straps together), the CMA did not fully develop owing to low compressive strength of concrete. The relative transverse movement between girders was only 1.1 mm that clearly demonstrates the rigidity of restrains provided for the RC slab.

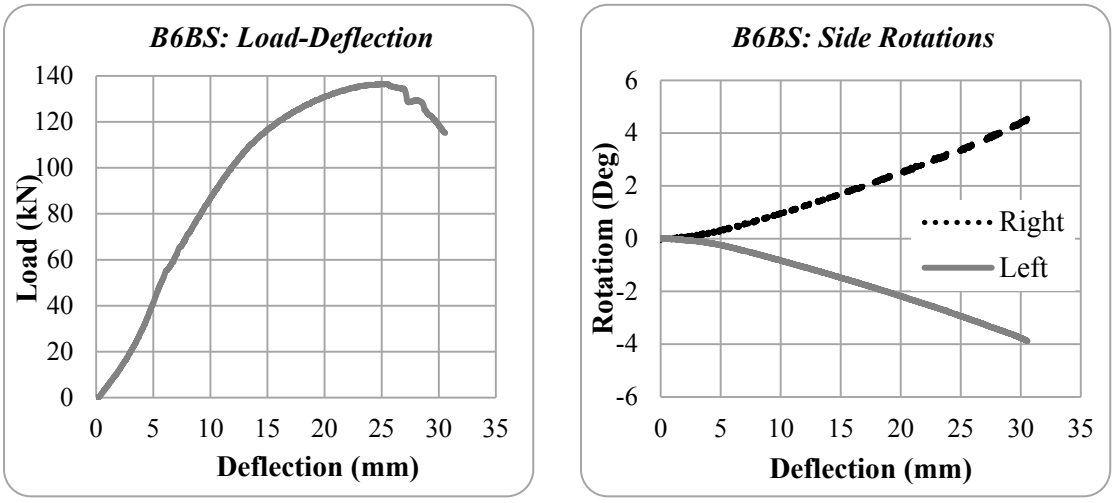

(a) (b)

Figure 3-38. (a) Load-deflection and (b) rotation-deflection graphs for specimen B6BS.

The modes of failure for all 10 samples are reported Table 3-7.

Table 3-7. Mode of failure for different samples.

Sample	***1-M6B***	***2-M4B***	***3-B4B***	***4-B6B***	***5-M6SS***
Mode of Failure	1	1	1	1	2
Sample	***6-M6S***	***7-M4BS***	***8-M6BS***	***9-B4BS***	***10-B6BS***
Mode of Failure	2	1	1	2	2

1- Refers to failure of connection due to extensive cracks between two holes accompanied with crushing of concrete

2- Refers to crushing of concrete only

Error! Reference source not found. and Table 3-9 highlight all the significant experimental results obtained throughout this study.

Table 3-8. Summary of experimental results.

					Lateral Restraint System									
		Instrument Type		***Unit***	***Bracing***				***…***	***Strap***	***Bracing & Strap***			
	Sample				*M6B*	*M4B*	*B4B*	*B6B*	*M6SS*	*M6S*	*M4BS*	*M6BS*	*B4BS*	*B6BS*
	1st Peak Load	…		kN	89.3	69.8	107.9	141.1	68.0	88.7	84.1	102.7	114.0	136.6
	2nd peak Load	…		kN	87.5	70.1	103.6	136.0	58.6	87.8	75.6	86.8	111.0	129.3
	Deflection in 1st max Load	LVDT		mm	18.8	15.0	16.5	22.4	24.3	23.3	23.9	25.4	24.2	24.8
At Max Load	***Bracing 1***	Strain Gauge	5-mm	μ strain	192.1	198.6	239.4	267.3	0.0	0.0	196.6	172.6	210.9	216.1
	Bracing 2				172.0	86.3	188.8	214.8	0.0	0.0	53.2	73.3	48.7	66.2
	Bracing 3				97.3	70.7	248.6	180.4	0.0	0.0	42.2	25.3	11.0	56.5
	Bracing 4				219.3	204.4	254.4	266.0	0.0	0.0	194.0	183.0	247.2	210.2
	Girder 1 - Bottom				-360.1	-236.8	-416.6	-420.5	-330.9	-434.1	-475.6	-430.2	-387.4	-382.8
	Girder 1 - Middle				-131.1	-90.8	-96.7	-129.8	-57.1	-81.8	-149.3	-138.9	-112.9	-114.9
	Girder 1 - Top				-319.9	-610.0	-741.1	-926.0	41.5	-536.7	-822.2	-522.4	-716.4	-562.0
	Girder 2 - Bottom				-240.1	-233.0	-249.9	-285.5	-190.1	-406.3	-427.0	-404.3	-433.5	-411.4
	Girder 2 - Middle				-87.6	-66.2	-68.1	-109.0	-27.3	-87.6	-112.9	-121.4	-97.3	-99.9
	Girder 2 - Top				-457.5	-300.4	-557.4	-526.9	51.9	-454.9	-651.5	-542.5	-704.0	-510.0
	Tensile Rebar 1				yielded	yielded	yielded	yielded	yielded	yielded	yielded	yielded	yielded	yielded
	Tensile Rebar 2				yielded	yielded	yielded	yielded	yielded	yielded	*NAN*	yielded	NAN	yielded
	Compressive Rebar 1				…	…	131.7	64.2	…	…	…	…	104.4	18.2
	Compressive Rebar 2				…	…	…	-34.4	…	…	…	…	196.6	-42.2

Table 3-9. Summary of experimental results (continue).

					Lateral Restraint System									
		Instrument Type		***Unit***	***Bracing***				***…***	***Strap***	***Bracing & Strap***			
	Sample				*M6B*	*M4B*	*B4B*	*B6B*	*M6SS*	*M6S*	*M4BS*	*M6BS*	*B4BS*	*B6BS*
At Max Load	***Concrete Compressive 1***	Strain Gauge	60-mm	µ strain	-3500.7	-3847.7	-1639.4	-1304.0	-3654.9	-2831.1	-2592.4	-3952.2	-3947.6	-2318.0
	Concrete Compressive 2	Strain Gauge	60-mm	µ strain	-2765.7	-3426.1	-2861.1	-1416.2	-3308.7	-2331.0	-3326.9	-2853.3	-3800.5	-3701.2
	Concrete soffit - edge 1	Strain Gauge	60-mm	µ strain	-82.4	-402.9	-522.9	339.9	-47.4	-83.0	-1167.1	…	…	…
	Concrete soffit - edge 2	Strain Gauge	60-mm	µ strain	-82.4	-186.2	-254.4	-213.5	36.3	-127.8	-228.4	…	…	…
	Strap 1	Strain Gauge	5-mm	µ strain	…	…	…	…	…	631.9	277.7	273.8	231.6	105.8
	Strap 2	Strain Gauge	5-mm	µ strain	…	…	…	…	…	467.8	291.3	323.1	374.4	192.1
	Inclinometer Left	Inclinometer		Deg	2.5	1.8	2.1	2.8	-2.8	-3.0	-3.0	-3.2	-3.0	-2.9
	Inclinometer Right	Inclinometer		Deg	-3.0	-1.9	-2.3	3.1	-3.6	-0.9	0.5	0.9	3.2	3.3
	Girder 1 Vertical Disp.	LVDT		mm	1.6	1.5	1.4	2.0	2.3	1.4	1.6	1.6	1.7	1.8
	Girder 2 Vertical Disp.	LVDT		mm	1.2	1.0	1.3	1.7	3.1	2.1	1.2	1.6	1.4	1.8
	Relative Disp. Of Girders	LVDT		mm	1.8	1.9	2.5	2.4	4.6	1.3	1.3	1.3	3.6	1.1

Chapter 4

Analysis of Results and Numerical Modelling

4.1 Ductility index and energy-based ductility

4.2 Numerical modelling

4.3 Finite element analysis (FEA) of samples

4 ANALYSIS OF THE RESULTS AND NUMERICAL MODELLING

4.1 Ductility index and energy-based ductility

One of the important factors in design of reinforced concrete structure is ductility. Ductility is the ability of a structure to undergo increasing deformation beyond yield point while still sustaining gravity and other loads (Sharpe, 1977). In other words, ductility is the ability of structural member to sustain inelastic deformation prior to collapse (Naaman et al., 1986).

To measure the ductility of a structure, different approaches have been introduced by researchers, however, in this study only:

1. Ductility (toughness) index
2. Energy-based ductility

are employed to determine and compare the ductility of tested RC concrete slabs.

Ductility Index

Ductility index is usually proposed as the ratio of deformation at ultimate state to deformation at first yield. However, not every reinforced concrete member contains conventional steel reinforcement with distinctive yielding point. For example, fibre reinforced polymer (FRP) bars and tendons do not yield, and accordingly the conventional definition of ductility index is not applicable for such concrete members reinforced by FRP bars (Jeong and Naaman, 1995). The FRP materials show linear stress-strain relationship up to the failure point with no distinctive yield point and no post yield plastic deformations. The load-deflection response of concrete beams reinforced by FRP bars is linear up to failure (with no distinctive yield point) and it is different from that for beams reinforced by conventional steel bars (Alsayed and Alhozaimy, 1999).

Energy-based Ductility

Modulus of toughness represents the amount of energy per unit volume of a material required to bring that material to verge of failure under static loading. Toughness index is an energy-based ratio (related to definition of modulus of toughness) proposing ratio of area under $\sigma - \varepsilon$, or $F - \delta$, or even $F - \varepsilon$ graphs up to ultimate load to the area of the graph related to elastic deformation. Independent of material type, this index can provide a measure of the ductility of structural system.

4.1.1 Ductility index

Several measures of ductility have been used in the past. They are generally expressed as a ratio called ductility index or ductility factor. Most common ductility indices are given either in terms of curvatures, rotations or deflections as follows:

$$\mu_{\emptyset} = \frac{\emptyset_u}{\emptyset_y} \qquad \text{Equation 27}$$

$$\mu_{\theta} = \frac{\theta_u}{\theta_y} \qquad \text{Equation 28}$$

$$\mu_{\Delta} = \frac{\Delta_u}{\Delta_y} \qquad \text{Equation 29}$$

where μ is the ductility index, $\emptyset$ is the curvature, θ is the rotation, and Δ is the deflection; the subscript y stands for yielding of the reinforcement and u denotes the ultimate.

4.1.2 Energy-based ductility

ACI Committee 544 (1998) defined the toughness index as the measure of the amount of energy required to deflect the concrete sample used in the modulus of rupture test by

a given amount compared to the energy required to bring the concrete to the point of first crack. The definition of the toughness index is illustrated in Figure 4-1.

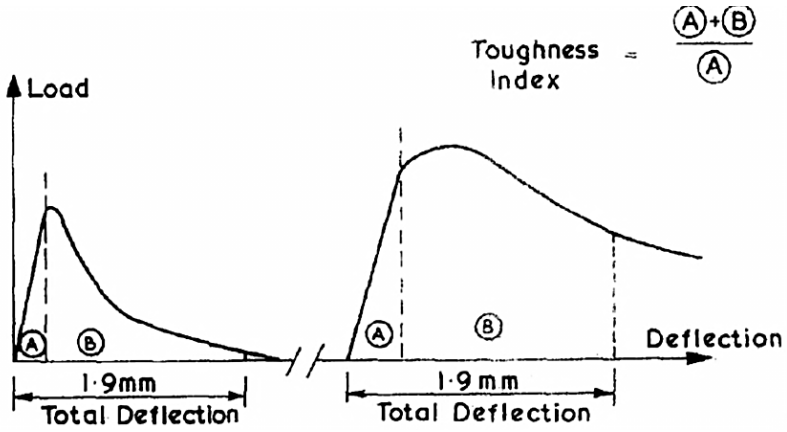

Figure 4-1. Definition of toughness index (ACI Committee 544).

Jeong and Naaman (1995) were among the first group of researchers who proposed idea of energy-based ductility. They suggested an energy-based ductility as follows

$$\mu_E = \frac{1}{2}\left(\frac{E_{tot}}{E_{el}} + 1\right) \qquad \text{Equation 30}$$

where E_{tot} is the total energy, i.e. the area under the load deflection curve up to the load defined as the failure load, and E_{El} is the elastic energy which is part of the total energy and it can be computed as the area of the triangle formed at failure. The graph in Figure 4-2 shows elastic and inelastic energy for different types of tendons.

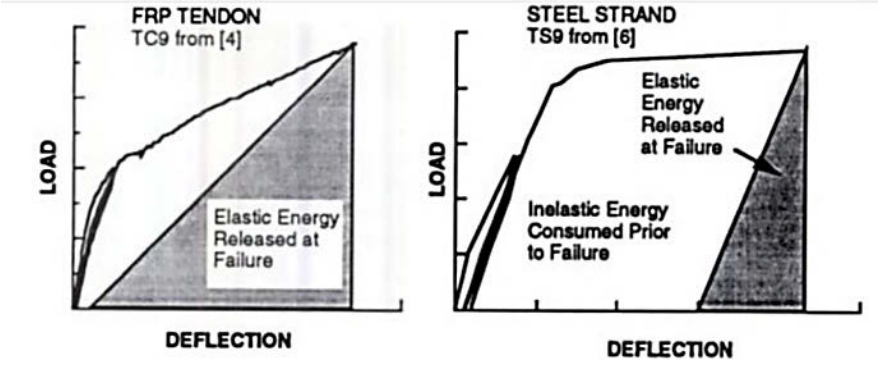

Figure 4-2. Elastic and inelastic energy in beams with different types of tendons.

Later, Spadea et al. (1997) proposed a new method of finding energy ductility as follows:

$$\mu_E = \frac{E_{tot}}{E_{0.75pu}} \qquad \text{Equation 31}$$

where E_{tot} is the total area under the load-deflection diagram up to the failure load and $E_{0.75pu}$ is the area under the load deflection diagram up to 75% of the ultimate load.

Foster and Attard (1997) proposed a new measure of ductility for RC columns subject to bending and compression. Foster and Attard's ductility is calculated with respect to the amount of work done in the plastic zone. This measure of ductility has been inspired by the definition of flexural toughness as set out in ASTM C 1018 (ASTM 1992)[1], where the level of ductility is defined using the I_{10} ductility index. The I_{10} ductility measure is defined as area OACEF (see Figure 4-3) divided by the area OAB, where B corresponds to the point ξ_y and F to the point $5.5\xi_y$. In this definition the elastic-perfectly plastic material has a ductility index $I_{10} = 10$ and for an elastic-brittle material $I_{10} = 1$.

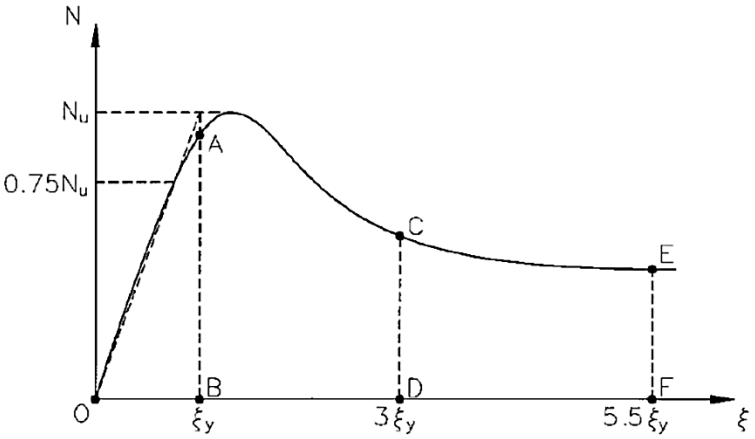

Figure 4-3. Energy ductility measure in eccentrically loaded columns.

[1] It is noteworthy that ASTM C 1018 (ASTM 1992 Standard test for flexural toughness and first-crack strength of fibre-reinforced concrete (using beam with third-point loading). *C 1018, West Conshohocken, Pa.*, 514-520.) was withdrawn in 2006.

In case of combined axial force and flexural loading, this approach is applicable as the ductility measure adopted is based on the area under the load versus ε curve, where $\xi = \varepsilon_{av} + \kappa e$, and, thus, both axial and bending components are considered.

In this section, ductility of 10 one-way restrained RC slabs is calculated based on the aforementioned approaches. Ductility index is calculated as the ratio of ultimate displacement over displacement at yielding point, $\mu_\Delta = \frac{\Delta_u}{\Delta_y}$ or $\mu_\theta = \frac{\theta_u}{\theta_y}$ (Figure 4-4). The value of ductility indices obtained from these formulas is given in Table 4-1.

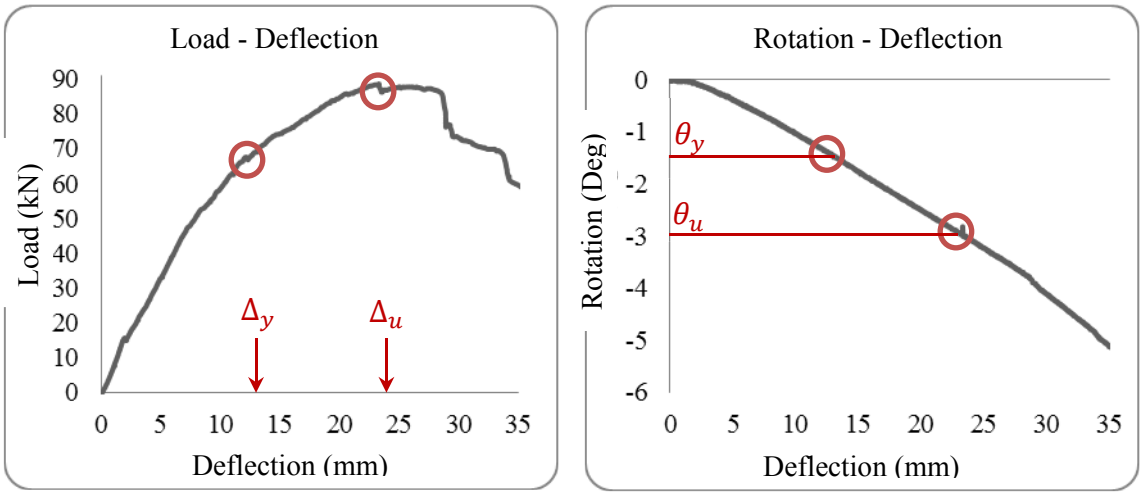

Figure 4-4. Ductility Index concept.

Table 4-1. Deformation-based ductility index values for the tested RC slabs.

Sample Name	M6B	M4B	B4B	B6B	M6SS	M6S	M4BS	M6BS	B4BS	B6BS
μ_Δ	1.42	1.04	1.77	1.96	1.69	1.77	1.41	1.62	1.95	1.94
μ_θ	1.53	1.07	2.08	2.25	1.77	2.01	1.55	1.83	2.5	2.47

Energy ductility is calculated based on the area under the $P - \Delta$ (load-deflection) graph. It is the proportion of the region OABC area to area of triangle OAD as shown in Figure 4-5 .

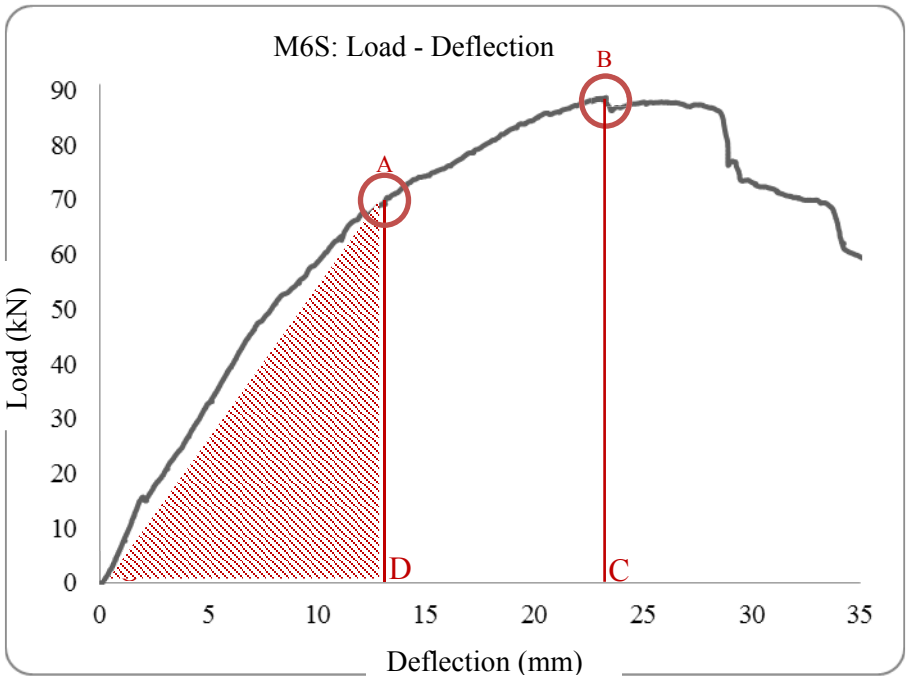

Figure 4-5. Energy ductility concept.

Values of energy toughness are presented in Table 4-2. As it can be seen, this energy-based approach provides higher ductility indices compared with 1D ductility index calculated based on deformation itself.

Table 4-2. Energy-based ductility indices for tested RC slabs.

Sample Name	M6B	M4B	B4B	B6B	M6SS	M6S	M4BS	M6BS	B4BS	B6BS
Energy Ductility	2.57	1.76	3.30	3.24	2.66	2.92	1.98	2.51	3.17	3.71

With regard to the ductility indices given in Tables 4-1 and 4-2, it is concluded that specimens with reinforcing bars located at the soffit of the slab show higher ductility compared with samples with one layer of isotropic reinforcement placed in the middle depth. In addition, use of horizontal straps together with bracing as restraining system (last four samples) does not make significant change in the ductility indices; however, by looking at the load-deflection diagrams of these four specimens, it is concluded that

the lateral fixity provided by X bracings and straps can postpone rupture of the reinforcing bars and accordingly the 2nd peak load in these specimens occurs at higher mid-span deflections.

4.2 Numerical modeling

4.2.1 Overview

The finite element method (FEM) is a numerical technique that can be used for finding approximate solutions to governing differential equations of engineering problem. The finite element analysis of any structure usually follows three well defined steps. First, the constitutive model of the material should be specified, that includes stress-strain behaviour and the associated failure criteria for the materials. Second, the finite element discretization of the structure is carried out, in which the structure to be analysed is divided into a finite number of elements, connected only at their nodes. Third, the simultaneous set of equations representing the model is assembled and solved.

In this study, FEM is used to find the numerical results and approximate behaviour of tested one way reinforced concrete slabs under monotonically increasing displacement controlled load. The results obtained from the FE models are compared with experimental data to demonstrate the adequacy of FE models for capturing the load-deflection and ultimate loading capacity of RC slabs in the proposed deconstructible steel-concrete composite bridge decks.

The computer program (software) used for FE analysis of RC slabs is 'ATENA'. This software has been utilised in this study, mainly because it has been specifically developed for nonlinear analysis of concrete structures and is known to have more options for 2D and 3D constitutive modelling of concrete. ATENA software takes advantage of continuum-based finite element models for solving the nonlinear governing equations. The concrete constitutive model in ATENA to be used in this study is called SBETA which is described further in details below. Furthermore, the

ATENA software takes advantage of an update Lagrangian formulation to capture geometrical nonlinearities.

4.2.2 Constitutive model SBETA[2]

Basic assumptions

The SBETA model is a 2D constitutive law formulated under a plane stress state. In SBETA, a smeared approach is used to model the material properties, such as cracks or distributed reinforcement. This means that material properties defined for a material point are valid within a certain material volume, which in this case, is associated with the entire finite element. The constitutive model is based on the stiffness and is described by the equation of equilibrium at a material point as follows:

$$s = De, s = \{\sigma_x, \sigma_y, \tau_{xy}\}^T, e = \{\varepsilon_x, \varepsilon_y, \gamma_{xy}\}^T \quad \text{Equation 32}$$

where s is the stress vector, D is the material stiffness matrix and e is a strain vector. The stress and strain vectors are composed of the stress components of the plane stress state σ_x, σ_y, τ_{xy} (Figure 4-6) and the strain components ε_x, ε_y, γ_{xy} (Figure 4-7), where γ_{xy} is the engineering shear strain. The stress vector (s) and the material matrix (D) can be decomposed into the material components due to concrete and reinforcement as:

$$s = s_c + s_s, D = D_c + D_s \quad \text{Equation 33}$$

The stress vector s and both component stress vectors s_c, s_s are related to the total cross sectional area. The concrete stress s_c is acting on the material area of concrete A_c, which is approximately set equal to the cross section of the composite material, $A_c \approx A$ (the area of concrete occupied by reinforcement is not subtracted).

[2] The contents of this section is derived from the ATENA handbook guide ČERVENKA, V., JENDELE, L. & ČERVENKA, J. 2012. ATENA Program Documentation-Part 1-Theory *Cervenka Consulting Ltd.*

The matrix *D* has a form of the Hooke's law for either isotropic or orthotropic material, as will be shown later.

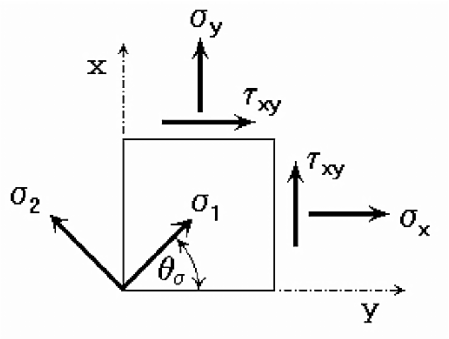

Figure 4-6. Components of plane stress state (Červenka et al., 2012).

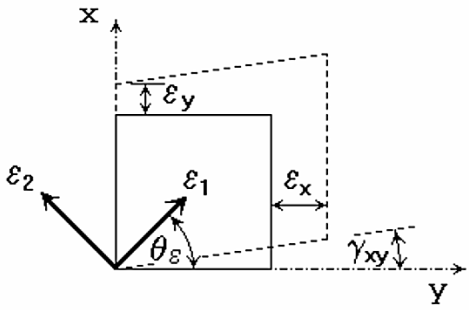

Figure 4-7. Components of plane strain state (Červenka et al., 2012).

The reinforcement stress vector s_s is the sum of stresses of all the smeared reinforcement components:

$$s_s = \sum_{i=1}^{n} s_{si} \qquad \text{Equation 34}$$

where n is the number of the smeared reinforcement components. For the i^{th} reinforcement, the global component reinforcement stress s_{si} is related to the local reinforcement stress σ_{si} by the transformation:

$$s_{si} = T_\sigma p_i \sigma_{si}$$ Equation 35

where p_i is the reinforcing ratio $p_i = \frac{A_{si}}{A_c}$, A_{si} is the reinforcement cross sectional area. The local reinforcement stress σ_{si} is acting on the reinforcement area A_{si}.

The stress and strain vectors are transformed according to the Equation 36 to Equation 38 in the plane stress state. New axes *u*, *v* are rotated from the global *x*, *y* axes by the angle α. The angle α is positive in the counter clockwise direction, as shown in Figure 4-8.

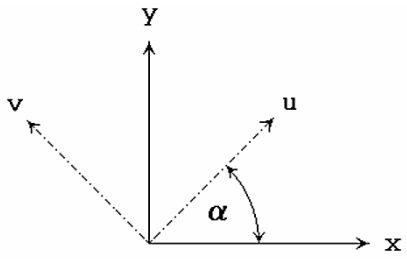

Figure 4-8. Rotation of reference coordinate axes (Červenka et al., 2012)

The transformation of the stresses is governed by,

$$s_{(u)} = T_\sigma s_{(x)}$$ Equation 36

$$\mathbf{T}_\sigma = \begin{bmatrix} \cos(\alpha)^2 & \sin(\alpha)^2 & 2\cos(\alpha)\sin(\alpha) \\ \sin(\alpha)^2 & \cos(\alpha)^2 & -2\cos(\alpha)\sin(\alpha) \\ -\cos(\alpha)\sin(\alpha) & \cos(\alpha)\sin(\alpha) & \cos(\alpha)^2 - \sin(\alpha)^2 \end{bmatrix}$$ Equation 37

$$s_{(u)} = \{\sigma_u, \sigma_v, \tau_{uv}\}^T, s_{(x)} = \{\sigma_x, \sigma_y, \gamma_{xy}\}^T$$ Equation 38

The transformation of the strains is governed by,

$$e_{(u)} = T_\sigma e_{(x)}$$ Equation 39

$$\mathbf{T}_\varepsilon = \begin{bmatrix} \cos(\alpha)^2 & \sin(\alpha)^2 & \cos(\alpha)\sin(\alpha) \\ \sin(\alpha)^2 & \cos(\alpha)^2 & -\cos(\alpha)\sin(\alpha) \\ -2\cos(\alpha)\sin(\alpha) & 2\cos(\alpha)\sin(\alpha) & \cos(\alpha)^2 - \sin(\alpha)^2 \end{bmatrix}$$ Equation 40

$$e_{(u)} = \{\varepsilon_u, \varepsilon_v, \tau_{uv}\}^T, s_{(x)} = \{\varepsilon_x, \varepsilon_y, \gamma_{xy}\}^T$$ Equation 41

The angles of principal axes of the stresses and strains, Figure 4-6, Figure 4-7, are found from the equations:

$$\tan(2\vartheta_\sigma) = \frac{2\tau_{xy}}{\sigma_x - \sigma_y}, \tan(2\vartheta_\varepsilon) = \frac{\gamma_{xy}}{\varepsilon_x - \varepsilon_y}$$ Equation 42

where ϑ_σ is the angle of the first principal stress axis and ϑ_ε is the angle of the first principal strain axis.

In case of isotropic material (un-cracked concrete) the principal directions of the stress and strains are identical; in case of anisotropic material (cracked concrete) they can be different. The sign convention for the normal stresses, employed within this program, uses the positive values for the tensile stress (strain) and negative values for the compressive stress (strain). The shear stress (strain) is positive if acting upwards on the right face of a unit element.

The material model SBETA includes the following effects of concrete behaviour:

- Non-linear behaviour in compression including hardening and softening,
- Fracture of concrete in tension based on the nonlinear fracture mechanics,
- Biaxial strength failure criterion,
- Reduction of compressive strength after cracking,

- Tension stiffening effect,
- Reduction of the shear stiffness after cracking (variable shear retention),
- Two crack models: fixed crack direction and rotated crack direction.

Perfect bond between concrete and reinforcement is assumed within the smeared concept. No bond slip can be directly modelled except for the one included inherently in the tension stiffening. However, on a macro-level, a relative slip displacement for reinforcement with respect to concrete over a certain distance can arise, if concrete is cracked or crushed. This corresponds to a real mechanism of bond failure in case of the bars with ribs. The reinforcement in both forms, smeared and discrete, is in the uniaxial stress state and its constitutive law is a multi-linear stress-strain diagram.

The material matrix is derived using the nonlinear elastic approach. In this approach the elastic constants are derived from a stress-strain function called here the "equivalent uniaxial law". This approach is similar to the nonlinear hypoelastic constitutive model, except that different laws are used here for loading and unloading, causing the dissipation of energy exhausted for the damage of material. The detailed treatment of the theoretical background of this subject can be found, for example, in the book by Chen (1982). This approach can also be regarded as an isotropic damage model, with the unloading modulus representing the damage modulus.

Stress-Strain Relations for Concrete

The nonlinear behaviour of concrete in the biaxial stress state is described by means of the so-called effective stress σ_c^{ef} , and the equivalent uniaxial strain ε^{eq} . The effective stress is in most cases a principal stress.

The equivalent uniaxial strain is introduced in order to eliminate the Poisson's effect in the plane stress state.

$$\varepsilon^{eq} = \frac{\sigma_{ci}}{E_{ci}}$$ Equation 43

The equivalent uniaxial strain can be considered as the strain, that would be produced by the stress σ_{ci} in a uniaxial test with modulus E_{ci} associated with direction i. Within this assumption, the nonlinearity representing damage is caused only by the governing stress σ_{ci}. The details can be found in Chen (1982).

The complete equivalent uniaxial stress-strain diagram for concrete is shown in Figure 4-9.

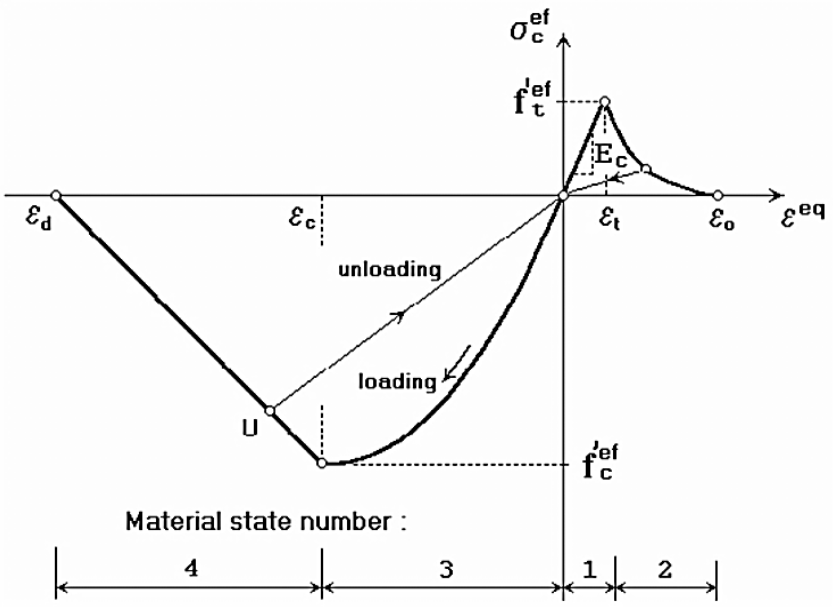

Figure 4-9. Concrete uniaxial stress-strain diagram (Červenka et al., 2012).

The numbers on the diagram in Figure 4-9 (material state numbers) are used in the results of the analysis to indicate the state of damage of concrete.

Unloading is a linear function to the origin. An example of the unloading point U is shown in Figure 4-9. Thus, the relation between stress σ_c^{ef} and strain ε^{eq} is not unique and depends on a load history. A change from loading to unloading occurs when the

increment of the effective strain changes the sign. If subsequent reloading occurs the linear unloading path is followed until the last loading point U is reached again. Then, the loading function is resumed. The peak values of stress in compression $f_c'^{ef}$ and in tension $f_t'^{ef}$ are calculated according to the biaxial stress state as will be shown later. Thus, the equivalent uniaxial stress-strain law reflects the biaxial stress state.

The above defined stress-strain relation is used to calculate the elastic modulus for the material stiffness matrices. The secant modulus is calculated as

$$E_c^s = \frac{\sigma_c}{\varepsilon^{eq}} \qquad \text{Equation 44}$$

It is used in the constitutive equation to calculate stresses for the given strain state.

The tangent modulus E_c^t is used in the material matrix D_c for construction of an element stiffness matrix for the iterative solution. The tangent modulus is the slope of the stress-strain curve at a given strain which is always positive. In cases when the slope of the curve is less than the minimum value $E_{\min}^t$, the value of the tangent modulus is set at $E_c^t = E_{\min}^t$. This occurs in the softening ranges and near the compressive peak.

Detailed description of the concrete stress-strain law is given in the following subsections.

Tension before Cracking

The behaviour of concrete in tension without cracks is assumed linear elastic. E_c is the initial elastic modulus of concrete, $f_t'^{ef}$ is the effective tensile strength derived from the biaxial failure function.

$$\sigma_c^{ef} = E_c \varepsilon^{eq}, \qquad 0 \le \sigma_c \le f_t'^{ef}$$ Equation 45

Tension after Cracking

Two types of formulations are used for the crack opening:

1. A fictitious crack model based on a crack-opening law and fracture energy. This formulation is suitable for modelling of crack propagation in concrete. It is used in combination with the crack band.

2. A stress-strain relation in a material point. This formulation is not suitable for normal cases of crack propagation in concrete and should be used only in some special cases.

In the following, five softening models included in SBETA material model are described.

- *Exponential crack opening law*

This function of crack opening was derived experimentally by HORDIJK (1991).

$$\frac{\sigma}{f_t'^{ef}} = \left\{1 + \left(c_1 \frac{w}{w_c}\right)^3\right\} exp\left(-c_2 \frac{w}{w_c}\right) - \frac{w}{w_c}(1 + c_1^3) exp(-c_2)$$ Equation 46

where w is the crack opening, $w_c = 5.14 \frac{G_f}{f_t'^{ef}}$ is the crack opening at the complete release of stress, σ is the normal stress in the crack (crack cohesion). Values of the constants are, $c_1 = 3$, $c_2 = 6.93$. G_f is the fracture energy needed to create a unit area of stress-free crack, $f_t'^{ef}$ is the effective tensile strength derived from a failure function. The crack opening displacement w is derived from strains according to the crack band theory.

- *Linear crack opening law*

$$\frac{\sigma_c^{ef}}{f'^{ef}_t} = \frac{f'_t}{w_c}(w_c - w), \qquad w_c = \frac{2G_f}{f'_t}$$ Equation 47

- *Linear softening based on local strain*

The descending branch of the stress-strain diagram is defined by the strain c_3 (Figure 4-10) corresponding to zero stress (complete release of stress).

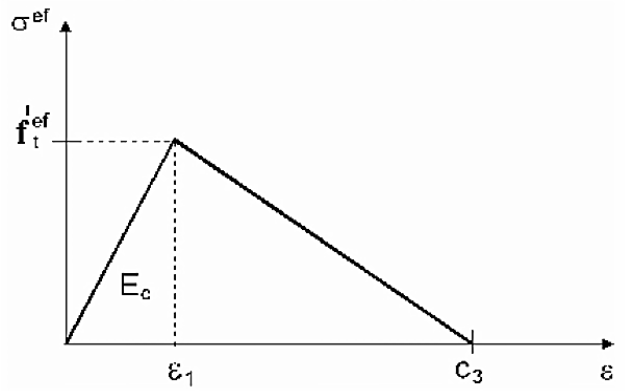

Figure 4-10. Linear softening based on strain (Červenka et al., 2012).

- *SFRC based on fracture energy (see)*

Parameters:

$$c_1 = \frac{f_1}{f'^{ef}_t}, \qquad c_2 = \frac{f_2}{f'^{ef}_t}, \qquad w_c = \frac{2G_f}{f_1 + f_2}$$ Equation 48

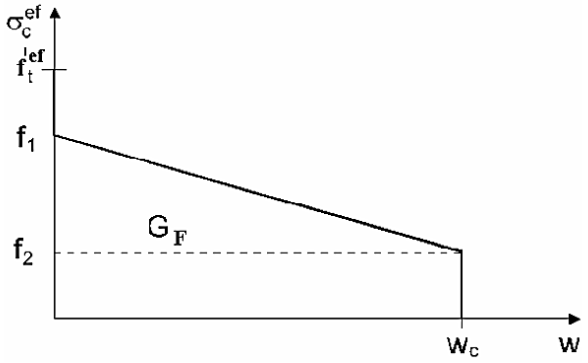

Figure 4-11. Steel fibre reinforced concrete based on fracture energy (Červenka et al., 2012).

- *SFRC based on strain*

Parameters:

$$c_1 = \frac{f_1}{f'^{ef}_t}, \qquad c_2 = \frac{f_2}{f'^{ef}_t} \qquad \text{Equation 49}$$

Parameters c_1 and c_2 are relative positions of stress levels, and c_3 is the end strain as seen in Figure 4-12.

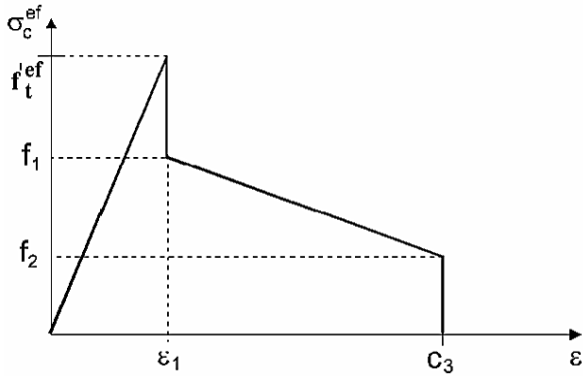

Figure 4-12. Effective stress versus strain for steel fibre reinforced concrete under tension (Červenka et al., 2012).

Compression before peak stress

The formula recommended by CEB-FIP Model Code 90 has been adopted for the ascending branch of the concrete stress-strain law in compression (see Figure 4-13). This formula can fit within a wide range of curves and it is applicable for normal as well as high strength concrete.

$$\sigma_c^{ef} = f'^{ef}_c \frac{kx - x^2}{1 + (k-2)x}, \qquad x = \frac{\varepsilon}{\varepsilon_c}, \qquad k = \frac{E_0}{E_c} \qquad \text{Equation 50}$$

where σ_c^{ef} denotes concrete compressive stress, f'^{ef}_c is effective compressive strength of concrete, x is normalized strain, ε denotes strain, ε_c is strain at the peak stress f'^{ef}_c, k is a shape parameter, E_o is the initial elastic modulus and E_c is the secant elastic

modulus at the peak stress, $E_c = \frac{f_c'^{ef}}{\varepsilon_c}$. Parameter *k* may take any positive value greater than or equal to 1. Examples, *k* = 1 linear and *k* = 2 parabola.

As a consequence of the above assumptions, distributed damage is considered before the peak stress is reached, contrary to the localized damage, which is considered that occur after the peak.

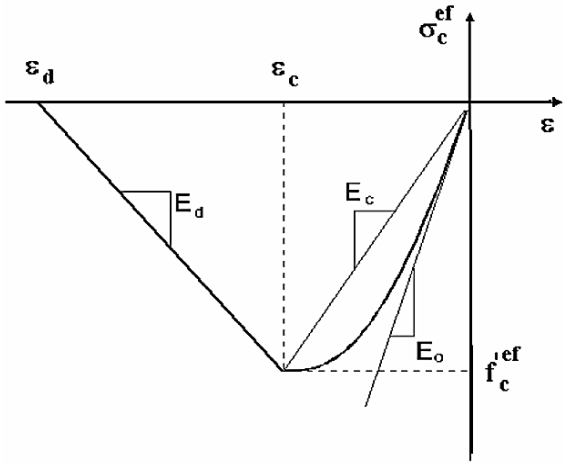

Figure 4-13. Outline of the stress-strain diagram for concrete under compression (Červenka et al., 2012).

Compression after peak stress

The concrete under compression follows a linear descending post-peak (softening) branch. In ATENA, two models of strain softening for concrete under compression are available, i.e. one based on dissipated energy, and the other based on local strain softening.

- *Fictitious Compression Plane Model*

The fictitious compression plane model is based on the assumption that compression failure is localized in a plane normal to the direction of compressive principal stress. All post-peak compressive displacements and energy dissipation are localized in this plane.

It is assumed that this displacement is independent of the size of the structure. This hypothesis is supported by experiments conducted by Van MIER (1986).

The fictitious compression plane model is based on the assumption that compression failure is localized in a plane normal to the direction of compressive principal stress. All post-peak compressive displacements and energy dissipation are localized in this plane. It is assumed that this displacement is independent of the size of the structure. This hypothesis is supported by experiments conducted by Van MIER (1986).

This assumption is analogous to the Fictitious Crack Theory for tension, where the shape of the crack-opening law and the fracture energy are defined and are considered as material properties. It is noteworthy that both material modelling techniques can adequately alleviate the spurious mesh sensitivity and lack of objectivity associated with softening of materials.

In case of compression, the end point of the softening curve is defined by means of the plastic displacement w_d. In this approach, the energy needed for generating a unit area of the failure plane is indirectly defined. From the experiments of Van MIER (1986), a value of w_d = 0.5 mm for normal concrete can be adopted. This value is used as default for the defining the concrete softening under compression.

The softening law can be transformed from a fictitious failure plane model (**Error! Reference source not found.**) to the stress-strain relation valid for the corresponding volume of continuous material (Figure 4-13). The slope of the softening part of the stress-strain diagram is defined by two points, i.e. peak of the diagram at the maximal stress and a compressive strain limit ε_d at the zero stress. This strain is calculated from a plastic displacement w_d and a band size L'_d according to the following expression,

$$\varepsilon_d = \varepsilon_c + \frac{w_d}{L'_d} \qquad \text{Equation 51}$$

This formulation provides a softening law which is independent of finite element mesh size.

- *Compression Strain Softening Law*

In this approach the slope of softening law is defined by means of the softening modulus E_d. This formulation is also dependent of the finite element mesh size.

4.2.3 Localization limiters

The so-called localization limiter controls localization of deformations in the failure state. It is a region (band) of material which represents a discrete failure plane in the finite element analysis. In tension it is a crack, in compression it is a plane of crushing. In reality these failure regions have some dimensions. According to the experiments, the dimensions of the failure regions are independent of the structural size and they are assumed as fictitious planes. In case of tensile cracks, this approach is known as "crack band theory", BAZANT, OH (1983). In ATENA the same concept is also used for the compression failure. The purpose of the failure band is to eliminate two deficiencies, which occur in connection with the application of the finite element model, i.e. element size effect and element orientation effect (Figure 4-14).

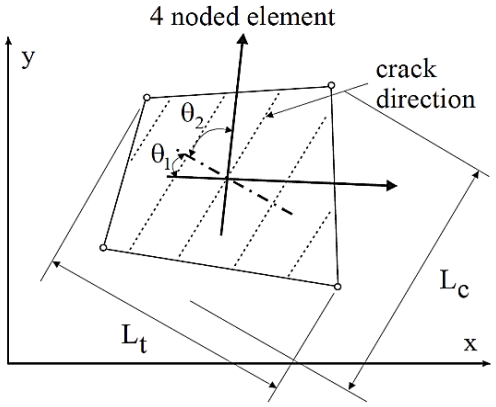

Figure 4-14. Definition of localization bands (Červenka et al., 2012).

4.2.4 Fracture process, crack width

The process of crack formation in concrete can be divided into three stages (Figure 4-15). The uncracked stage is before tensile strength is reached. The crack formation takes place in the process zone of a potential crack with decreasing tensile stress on a crack face due to a bridging effect. Finally, after a complete release of the stress, the crack opening continues without the stress.

The crack width *w* is calculated as a total crack opening displacement within the crack band.

$$w = \varepsilon_{cr} L'_t \qquad \text{Equation 52}$$

where w_{cr} is the crack opening strain, and it is equal to the strain normal to the crack direction in the cracked state after the complete stress release.

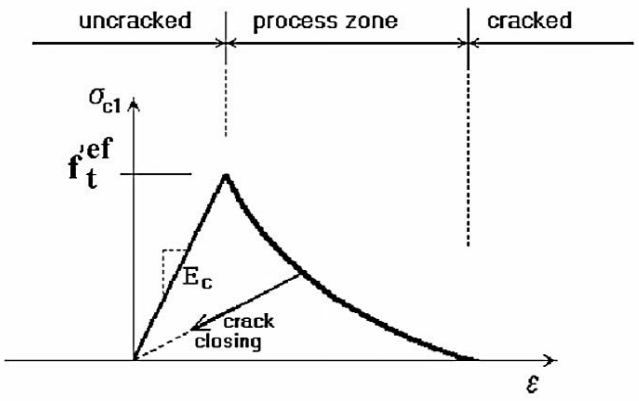

Figure 4-15. Stages of crack opening (Červenka et al., 2012).

It has been shown that the smeared model based on the refined crack band theory can successfully describe the discrete crack propagation in plain as well as reinforced concrete (CERVENKA et al. 1991, 1992, and 1995).

It is also possible that the second stress, parallel to the crack direction, exceeds the tensile strength. Then the second crack, in the direction perpendicular to the first one, is formed using the same softening model as the first crack. (Note: The second crack may not be shown in the post-processing interface of ATENA software. The exact state (uncrack, one or more than one crack) of concrete can be determined by the state number provided at the numerical output.

4.2.5 Biaxial stress failure criterion of concrete

Compressive Failure

A biaxial failure criterion according to KUPFER et al. (1969) is used for capturing concrete failure under plane stress states as shown in Figure 4-16.

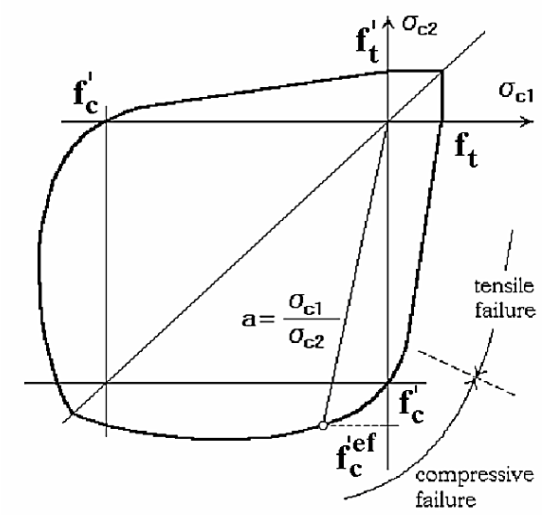

Figure 4-16. Biaxial failure function for concrete (Červenka et al., 2012).

In the compression-compression stress state the failure function is

$$f'^{ef}_c = \frac{1+3.65a}{(1+a)^2} f'_c, \qquad a = \frac{\sigma_{c1}}{\sigma_{c2}} \qquad \text{Equation 53}$$

where σ_{c1} and σ_{c2} are the principal stresses in concrete and f_c' is the uniaxial cylinder strength. In the biaxial stress state, the strength of concrete is predicted under the assumption of a proportional stress path.

In the tension-compression stress state, the failure function continues linearly from the point $\sigma_{c1} = 0$ and $\sigma_{c2} = f_c'$ into the tension-compression region with linearly decreasing strength:

$$f'^{ef}_c = f_c' r_{ec}, \qquad r_{ec} = \left(1 + 5.3278 \frac{\sigma_{c1}}{f_c'}\right), \qquad 1.0 \geq r_{ec} \geq 0.9 \qquad \text{Equation 54}$$

where r_{ec} is the reduction factor of the compressive strength in the principal direction 2 due to the tensile stress in the principal direction 1.

Tensile Failure

In the tension-tension stress state, the tensile strength is constant and equal to the uniaxial tensile strength f_t'. In the tension-compression state, the tensile strength is reduced by the relation:

$$f'^{ef}_{t} = f' r_{et} \qquad \text{Equation 55}$$

where r_{et} is the reduction factor of the tensile strength in the direction 1 due to the compressive stress in the direction 2. The reduction function has one of the following forms, Figure 4-17.

$$r_{et} = 1 - 0.95\frac{\sigma_{c2}}{f'_c} \qquad \text{Equation 56}$$

$$r_{et} = \frac{A + (A-1)B}{AB}, \qquad B = Kx + A, \qquad x = \frac{\sigma_{c2}}{f'_c} \qquad \text{Equation 57}$$

In Equation 56 the tensile strength of concrete decreases linearly with respect to the compressive stress perpendicular to the tensile stress direction, whereas in Equation 57 this relation is hyperbolic. Two predefined shapes of the hyperbola are given by the position of an intermediate point *r* and *x*. Constants *K* and *A* control the shape of the hyperbola. The values of the constants for the two positions of the intermediate point are given in Table 4-3.

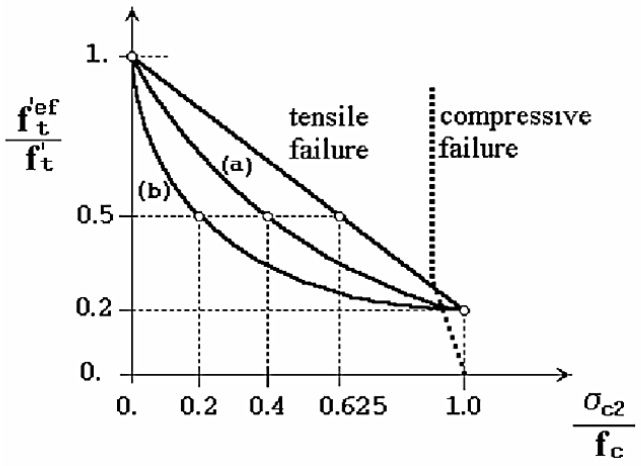

Figure 4-17. Tension-compression failure function for concrete (Červenka et al., 2012).

Two predefined shapes of the hyperbola are given by the position of an intermediate point *r* and *x*. Constants *K* and *A* define the shape of the hyperbola. The values of the constants for the two positions of the intermediate point are given in the following table.

Table 4-3. The values of constants related to Equation 57.

Type	Point		Parameters	
	r	x	A	K
a	0.5	0.4	0.75	1.125
b	0.5	0.2	1.0625	6.0208

4.2.6 Crack modelling

The smeared crack approach for modelling of the cracks is adopted in the SBETA model. Within the smeared concept, two options are available for crack modelling; the fixed crack model and the rotated crack model. In both models the crack is formed when the principal stress exceeds the tensile strength. It is assumed that the cracks are uniformly distributed within the material volume. This is reflected in the constitutive model by an introduction of orthotropy. In this study the rotated crack approach is adopted for modelling cracked concrete.

4.2.7 Compressive strength of cracked concrete

A reduction of the compressive strength after cracking in the direction parallel to the cracks is considered in the FE models by adopting the Vecchio and Collins (1982) approach that has been already formulated in the Compression Field Theory. However, in ATENA software a different function is used for the reduction of concrete strength, in order to allow for further adjustment of this effect. This function has the form of the Gauss's function, Figure 4-18. The parameters of the function were derived from the experimental data published by Kolleger et al. (1988), which included also data of Vecchio and Collins (Vecchio et al. 1982).

$$f'^{ef}_{c} = r_c f'_c, \qquad r_c = c + (1-c)e^{-(128\varepsilon_u)^2} \qquad \text{Equation 58}$$

For the zero normal strain (ε_υ) there is no strength reduction, and for the large strains, the strength is asymptotically approaching to the minimum value $f_c'^{ef} = cf_c'$. The constant *c* represents the maximal strength reduction under the large transverse strain. From the experiments by Kolleger et al. (1988), the value *c* = 0.45 was derived for the concrete reinforced with the fine mesh. The other researchers (Dyngeland 1989) found the reductions not less than *c* = 0.8. The value of *c* can be adjusted by input data according to the actual type of reinforcements.

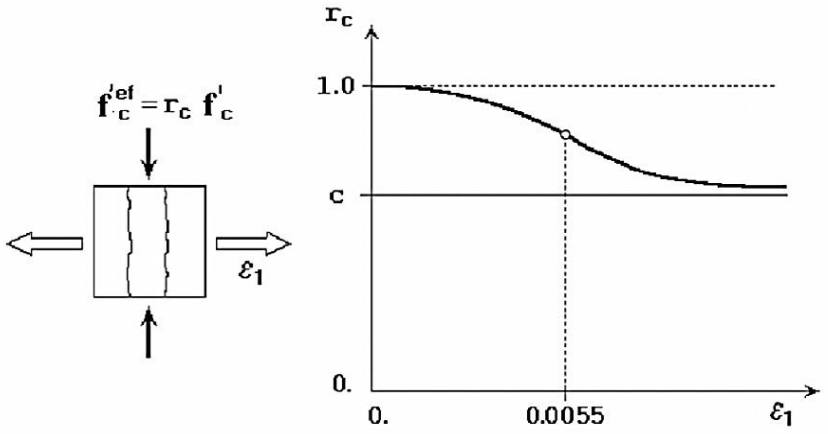

Figure 4-18. Compressive strength reduction of cracked concrete (Červenka et al., 2012).

It is noteworthy that the reduction of compressive strength of the cracked concrete does not have to be effected only by the reinforcements. In the plain concrete, when the strain localises in one main crack, the compressive concrete struts can cross this crack, causing so-called "bridging effect". The compressive strength reduction of these bridges can be also captured by the above model.

4.2.8 Tension stiffening in cracked concrete

The tension stiffening effect can be described as a contribution of cracked concrete to the tensile stiffness of reinforcing bars. This stiffness is provided by the uncracked concrete or not fully opened cracks and is generated by the strain localization process. It was verified by simulation experiments of Hartl, G. (1977) and discussed in details by Margoldova et al. (1998).

It is well established that including an explicit tension stiffening model would result in an overestimation of this effect. Therefore, in the ATENA software no explicit tension stiffening factor has been implemented, however, the tension stiffening effect can be implicitly captured by adjusting the softening part of stress-strain relationship for tensile concrete.

4.2.9 Material stiffness matrices

Uncracked concrete

The material stiffness matrix for the uncracked concrete has the form of an elastic matrix of an isotropic material. It is written in the global coordinate system *x* and *y* as,

$$\mathbf{D}_c = \frac{E}{1-\nu^2}\begin{bmatrix} 1 & \nu & 0 \\ \nu & 1 & 0 \\ 0 & 0 & \frac{1-\nu}{2} \end{bmatrix} \qquad \text{Equation 59}$$

where E is the concrete elastic modulus derived from the equivalent uniaxial law and ν is the Poisson's ratio that is assumed to be constant throughout the analysis.

Cracked concrete

For the cracked concrete, the matrix has the form of the elastic matrix for the orthotropic material. The matrix is formulated in a coordinate system $m1$ and $m2$, which is coincident with the crack direction. This local coordinate system is referred to with superscript L later. The direction 1 is normal to the crack and the direction 2 is parallel to the crack. The definition of the elastic constants for the orthotropic material in the plane stress state follows from the flexibility relation,

$$\begin{Bmatrix} \varepsilon_1 \\ \varepsilon_2 \\ \gamma \end{Bmatrix} = \begin{bmatrix} \frac{1}{E_1} & -\frac{\nu_{21}}{E_2} & 0 \\ -\frac{\nu_{12}}{E_1} & \frac{1}{E_2} & 0 \\ 0 & 0 & \frac{1}{G} \end{bmatrix} \begin{Bmatrix} \sigma_1 \\ \sigma_2 \\ \tau \end{Bmatrix} \qquad \text{Equation 60}$$

In the equivalent uniaxial strain approach adopted in the ATENA software, first the orthotropic Poisson's ratios are eliminated for the cracked concrete, because they are

commonly not known. Furthermore, the relation $\nu_{12}E_2 = \nu_{21}E_1$ is adopted to preserve the symmetry of material stiffness matrix. Therefore, in Equation 60 there are only three independent elastic constants E_1, E_2 and ν_2. Assuming that $\nu_{21} = \nu$ is the Poisson's ratio of the uncracked concrete and using the symmetry relation,

$$\nu_{12} = \frac{E_1}{E_2}\nu \qquad \text{Equation 61}$$

The stiffness matrix D_c^L is found as the inverse of the flexibility matrix in Equation 61:

$$\mathbf{D}_c^{\ L} = H\begin{bmatrix} \xi & \nu\xi & 0 \\ \nu\xi & 1 & 0 \\ 0 & 0 & G \end{bmatrix} \qquad \text{Equation 62}$$

where;

$$\xi = \frac{E_1}{E_2}, \qquad H = E_1(1 - \xi\nu^2) \qquad \text{Equation 63}$$

In the above relation E_2 must be non-zero. If E_2 is zero and E_1 is non-zero, then an alternative formulation is used with the inverse parameter; $\frac{1}{\zeta} = \frac{E_2}{E_1}$. In the case that both elastic moduli are zero, the matrix D_c^L is set equal to the null matrix.

The matrix D_c^L is transformed into the global coordinate system using the transformation matrix T_ε from Equation 40.

$$D_c = T_\varepsilon^T D_c^L T_\varepsilon \qquad \text{Equation 64}$$

The angle α is between the global axis x and the 1st material axis m_1, which is normal to the crack.

Smeared Reinforcement

In case the reinforcing steel bars are smeared across the concrete cross section, then te material stiffness matrix of the i^{th} smeared reinforcement can be obtained from;

$$\mathbf{D}_{si} = p_i E_{si} \begin{bmatrix} \cos(\beta_i)^4 & \cos(\beta_i)^2 \sin(\beta_i)^2 & \cos(\beta_i)^3 \sin(\beta_i) \\ \cos(\beta_i)^2 \sin(\beta_i)^2 & \sin(\beta_i)^4 & \cos(\beta_i) \sin(\beta_i)^3 \\ \cos(\beta_i)^3 \sin(\beta_i) & \cos(\beta_i) \sin(\beta_i)^3 & \cos(\beta_i)^2 \sin(\beta_i)^2 \end{bmatrix} \quad \text{Equation 65}$$

The angle β is between the global axis x and the i^{th} reinforcement direction, and E_{si} is the elastic modulus of reinforcement. p_i is the reinforcing ratio and $p_i = A_s / A_c$.

Stiffness of composite material (reinforced concrete)

The total material stiffness of the reinforced concrete is the sum of material stiffness of concrete and smeared reinforcement as follows

$$D = D_c + \sum_{i=1}^{n} D_{si} \quad \text{Equation 66}$$

where D_c and D_{si} are the stiffness matrix of concrete and smeared reinforcements, respectively. The summation is over n smeared reinforcing components. In ATENA the smeared reinforcement is not added at the constitutive level, but is modelled by separate layers of elements whose nodes are connected to those of the concrete elements. This corresponds to the assumption of perfect bond between the smeared reinforcement and concrete.

It is noteworthy that the material stiffness matrices can be calculated based on either secant or tangent modulus of materials depending on the adopted scheme for solving the governing equations (e.g. direct iteration or Newton-Raphson).

4.2.10 Analysis of stresses

The stresses in concrete are obtained using the actual secant component material stiffness matrix

$$S_c = D_c^s e \qquad \text{Equation 67}$$

where D_c^s is the secant material stiffness matrix for the uncracked or cracked concrete depending on the material state. The stress components are calculated in the global as well as in the local material coordinate (the principal stresses in the uncracked concrete and the stresses on the crack planes).

The stress in reinforcement and the associated tension stiffening stress is calculated from the strain in the direction of reinforcing bars.

4.2.11 Input parameters for constitutive modelling of materials

The SBETA constitutive model of concrete includes 20 material parameters. These parameters can be specified for the problem under consideration by the user. In case the parameters are not known, automatic generation can be done using the default formulas (some of which are given in Table 4-4). In such a case, only the cube strength of concrete f'_{cu} (nominal strength) needs to be specified and the remaining parameters are calculated as functions of the concrete cube strength. The formulas for these functions have been mainly taken from the CEB-FIP Model Code 90. SI units are used in the formulas given in Table 4-4.

Table 4-4. Default formulas for calculating the material input parameters (Červenka et al., 2012).

Parameter	Formula
Cylinder strength	$f_c' = -0.85 f_{cu}'$
Tensile strength	$f_t' = 0.24 f_{cu}'^{2/3}$
Initial elastic modulus	$E_c = \left(6000 - 15.5 f_{cu}'\right)\sqrt{f_{cu}'}$
Poisson's ratio	$\nu = 0.2$
Compressive strength in cracked concrete	$c = 0.8$
Tension stiffening stress	$\sigma_{st} = 0$
Fracture energy G_f according to VOS 1983	$G_F = 0.000025 f_t'^{ef}\ [\mathrm{MN/m}]$

4.3 Finite element analysis (FEA) of samples

4.3.1 Overview

In order to conduct FE analysis, ATENA 2D software package was used. All ten one-way RC slabs were simulated assuming a plane stress state for the structural components, including steel girders and their web stiffeners. Lateral restraining systems such as X cross bracings and straps were modelled by means of uniaxial truss elements. 2D interface gap elements were applied to create contact elements between concrete & steel and steel & steel plates. During the tests, no slip between RC slab and steel girders was observed, accordingly, the 8.8/FT shear connector bolts were modelled using post-tensioned truss elements with the same diameter as bolts.

As mentioned in previous chapter, a strain gauge was placed on each strap and X cross bracing to monitor the response of lateral restraining system during the tests. Since no slip was observed in straps and X bracings, a full-bond connection between straps and girder & X bracings and web stiffeners were considered in the FE models. This

assumption is also consistent with the fact that friction 8.8/FT bolts were used for fastening straps and X bracings to the top flange and the web stiffeners. Needless to say these friction bolts did not allow any slip in the connections that is also consistent with the assumption of perfect bond between steel girders and lateral restraining system. Following figures depict six different classes of steel-concrete composite decks modelled using ATENA software.

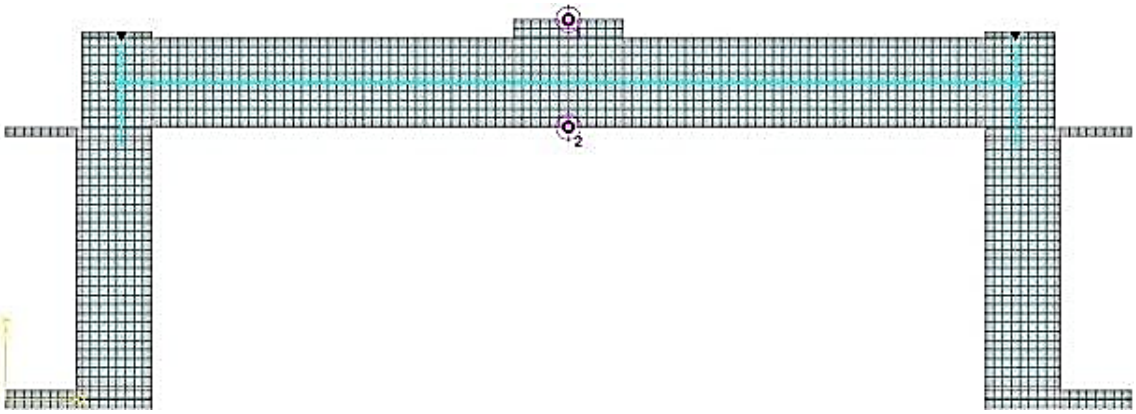

a) Sample M6SS– Simply Supported – Control Sample

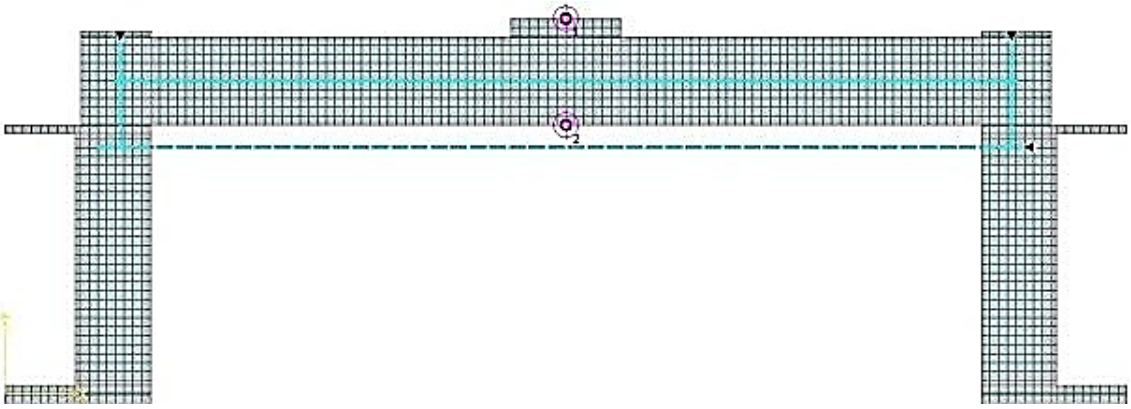

b) Sample M6S

Figure 4-19. Reinforcement arrangement/lateral restraining systems modelled in ATENA 2D- samples M6S and M6SS.

Samples with bracing only have the following reinforcement arrangements and lateral restraining system as shown in Figure 4-20.

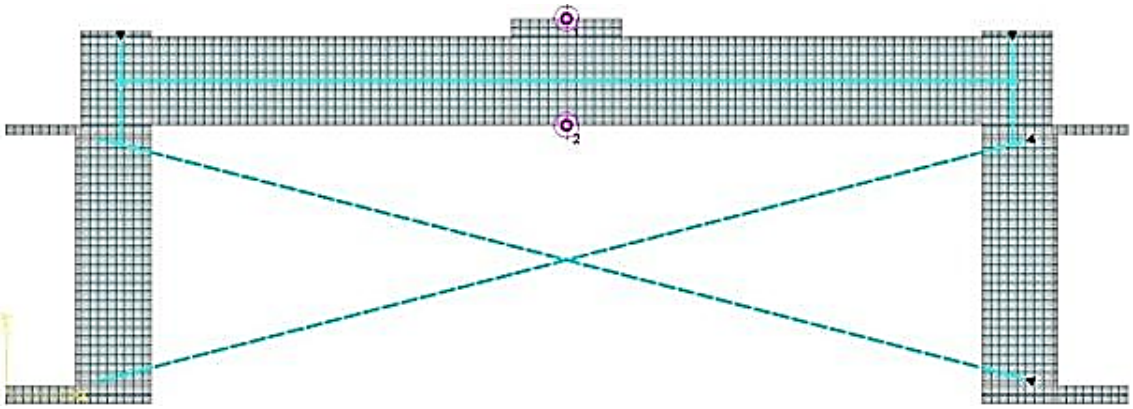

c) Samples M6B & M4B

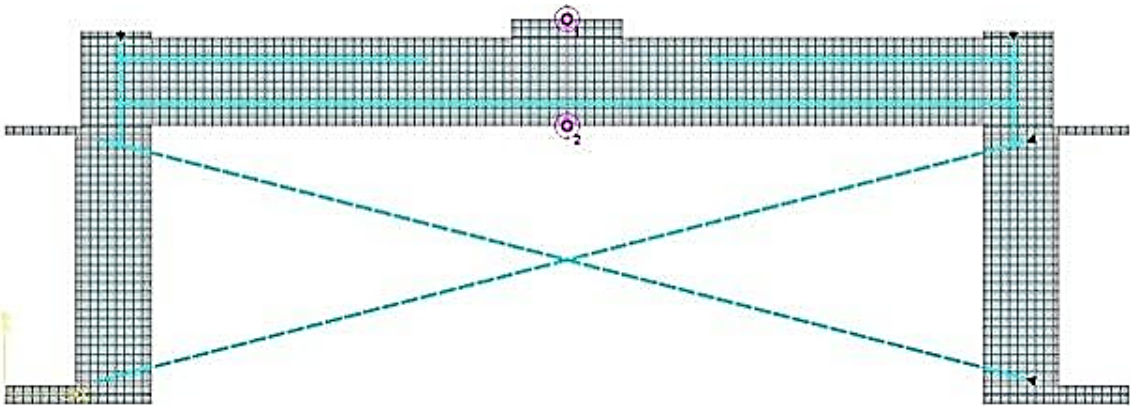

d) Samples B6B & B4B

Figure 4-20. Reinforcement arrangement/lateral restraining systems modelled in ATENA 2D.

Finally, four last samples which had bracing together with strap for lateral confinement are shown in following pictures.

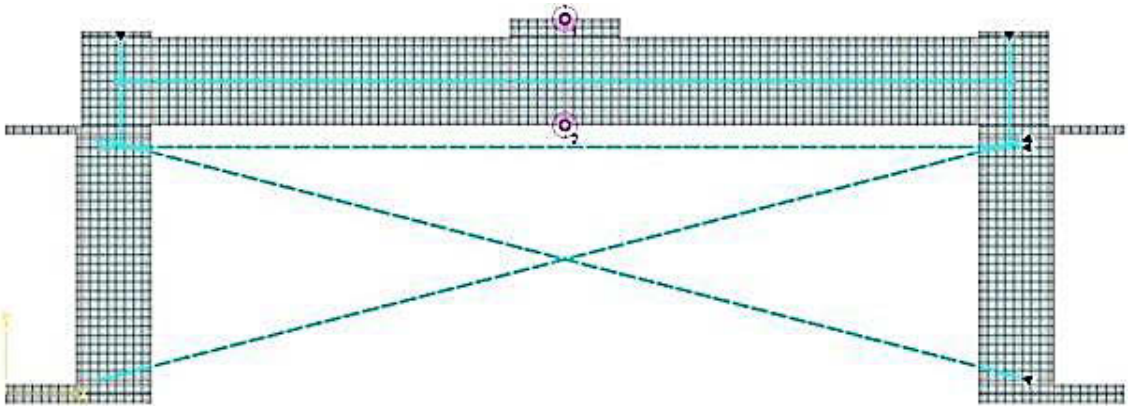

e) Samples M6BS & M4BS

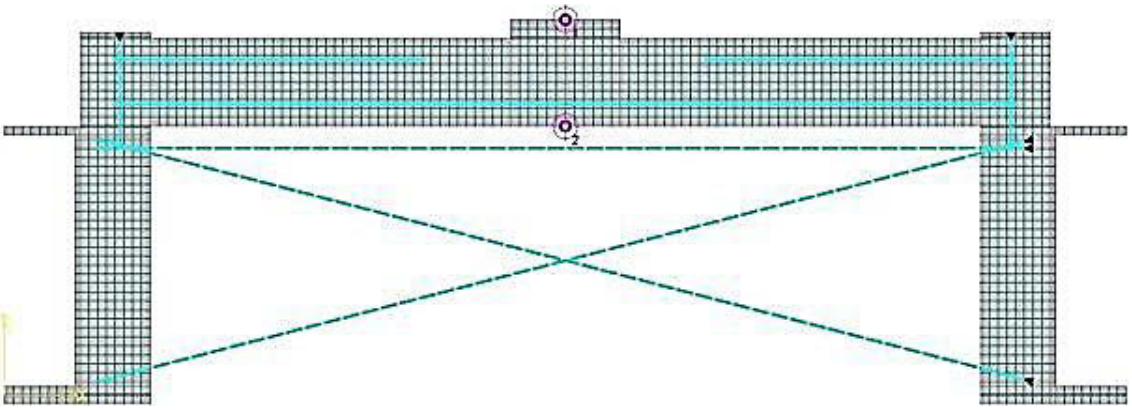

f) Samples B6BS & B4BS

Figure 4-21. Reinforcement arrangement/lateral restraining systems modelled in ATENA 2D.

A sensitivity analysis with respect to FE mesh size was carried out and a mesh size of 10 mm was used for all 10 specimens.

4.3.2 Numerical modelling results

As mentioned earlier, all 10 samples were modelled using ATENA 2D software. Table 4-5 summarises assumptions considered in the 2D modelling of tested steel-concrete composite decks.

Table 4-5. Specifications and assumptions considered in numerical modelling.

Mesh size	1 cm
Loading step	0.5 mm/step
Solution parameters	Standard Newton Raphson
Compression softening	Crush band

The comparison between experimental results and finite element predictions are presented in the following figures.

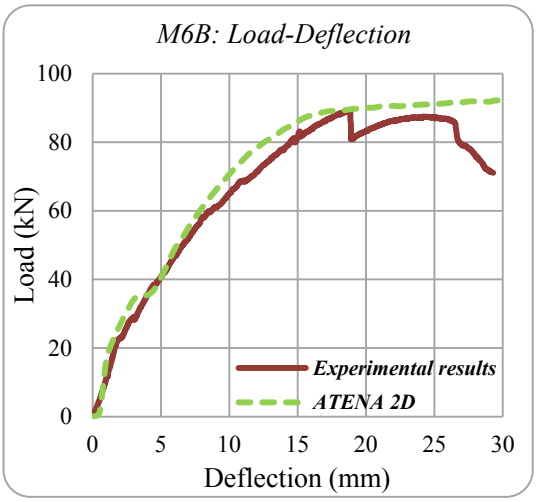

Figure 4-22. Numerical & experimental results for sample M6B.

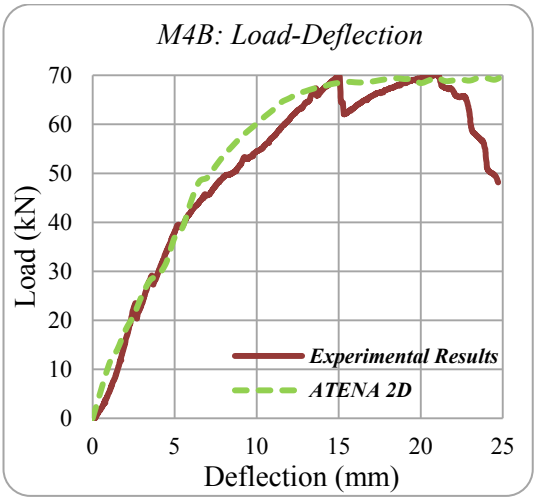

Figure 4-23. Numerical & experimental results for sample M4B.

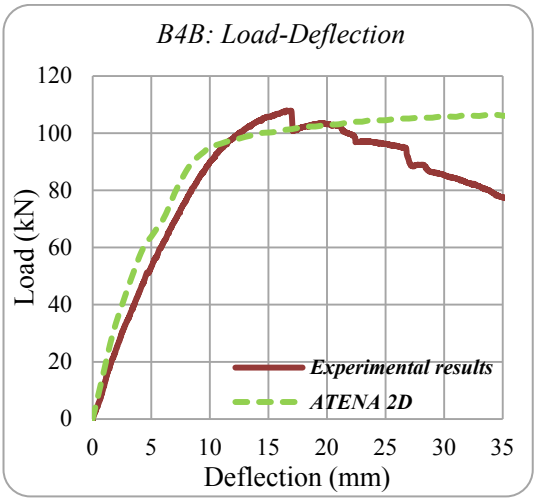

Figure 4-24. Numerical & experimental results for sample B4B.

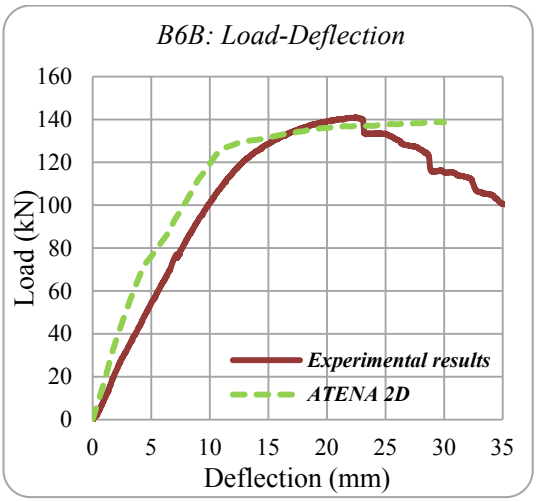

Figure 4-25. Numerical & experimental results for sample B6B.

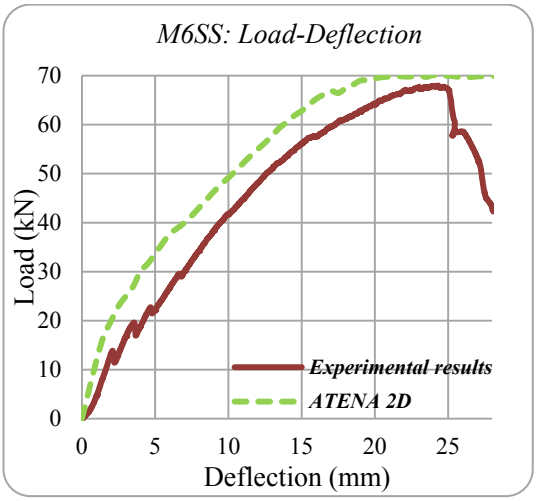

Figure 4-26. Numerical & experimental results for sample M6SS.

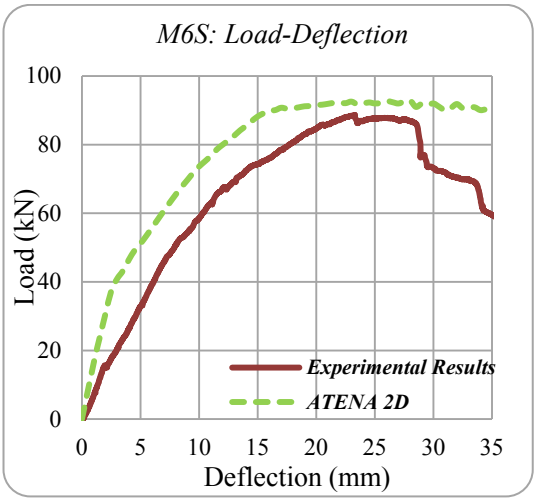

Figure 4-27. Numerical & experimental results for sample M6S.

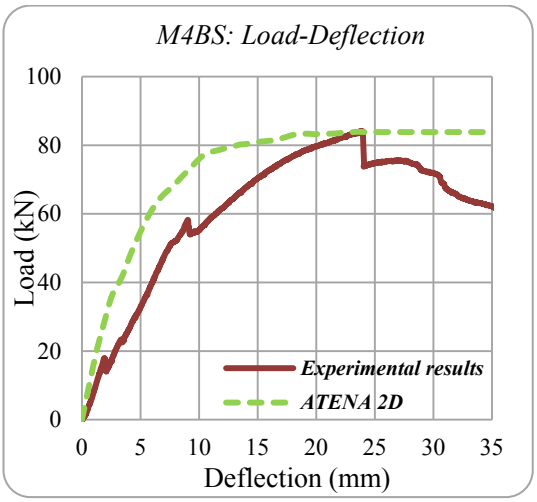

Figure 4-28. Numerical & experimental results for sample M4BS.

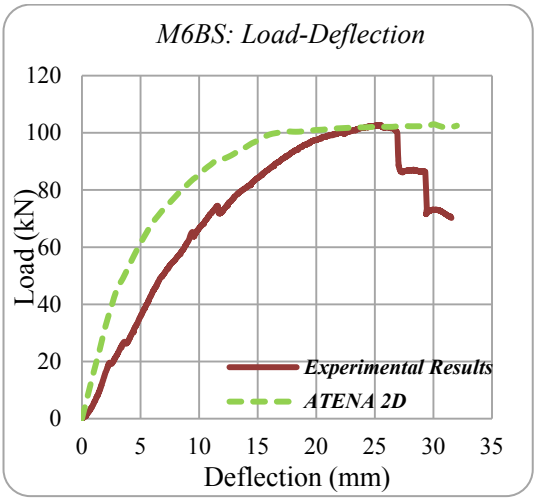

Figure 4-29. Numerical & experimental results for sample M6BS.

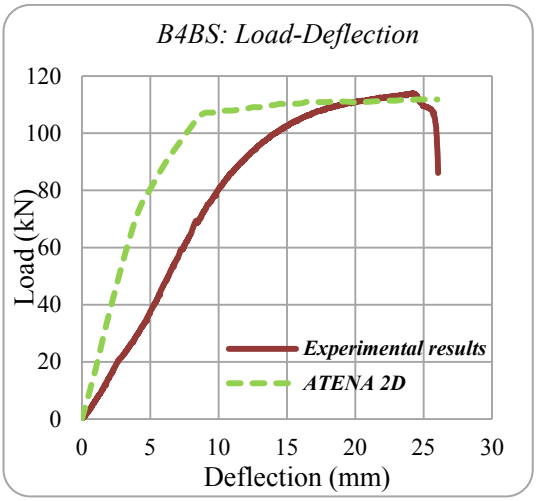

Figure 4-30. Numerical & experimental results for sample B4BS.

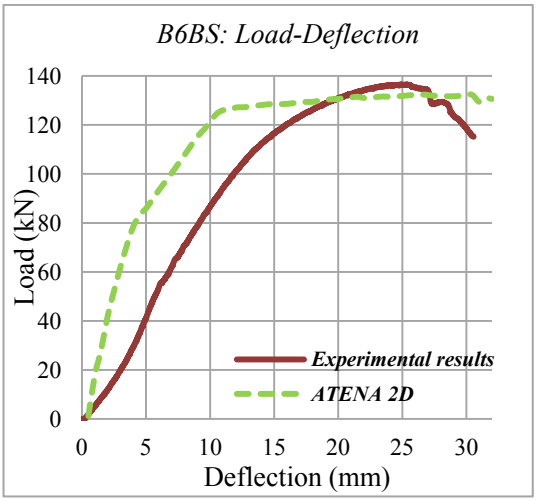

Figure 4-31. Numerical & experimental results for sample B6BS.

4.3.3 Conclusion

A 2D modelling has been conducted to numerically simulate the behaviour of 10 one-way RC slabs restrained against lateral expansion. Results of numerical modelling have been compared with experimental data. A good correlation between the FE results and experimental data was observed. It was shown that the 2D FE model can adequately capture the ultimate loading capacity and load-deflection response of RC slabs in the proposed deconstructible steel-concrete composite decks.

For those samples with X cross bracings and horizontal straps (last four samples), the initial slope of load-deflection response predicted by the FE models is higher than experimental data. This discrepancy can be attributed to 3D effects that cannot be captured by the developed 2D FE models. Also, it is seen that the 2D numerical models cannot capture the first sharp drop in the experimental load-deflection diagrams. These sharp drops are because of the cracks developing at the RC slab supports (between the bolted shear connectors). Obviously, the 2D FE models are unable to capture these cracks that run between two adjacent bolted shear connectors (see Figure 3-19c). These cracks only can be captured by the 3D models.

Chapter 5

Summary and Conclusion

5 SUMMARY AND CONCLUSION

The summary of all test results is presented in **Error! Reference source not found.**. With regard to the results of lab tests on 10 precast RC slabs strips that span between two steel girders and are connected to the girders by high strength bolted shear connectors, the following conclusions are drawn;

- The good performance of precast RC slabs in this novel steel-concrete composite deck system was demonstrated in the experimental programme and consistent results were achieved. It was shown that this system can be a reasonable choice for the next generation of composite bridge decks.

- Compressive membrane action induced in the system enhanced the ultimate loading capacity of the RC slabs. The transverse straps and X cross bracings provided for the RC slabs allowed for development of compressive membrane action (CMA). Also, the composite decks with both X cross bracing and straps had higher loading capacity compared with the systems with only straps or X cross bracings. This is clearly demonstrative of the enhancing effect of CMA in the composite decks with transverse restraints.

- The high strength bolted shear connectors demonstrated a superior performance with no failure or bending occurred in the bolts used as the shear connector. Furthermore, no slip between RC slab and steel girders occurred in the direction perpendicular to the girders.

- Specimens $1-4$ and $7-8$ failed due to major cracks developed in the neighbourhood of connection holes in the slabs, whereas other specimens mainly failed because of concrete crushing.

- Using straps together with X cross bracings in the last 4 specimens provided higher lateral stiffness for the RC slabs and reduced the longitudinal expansion of the one-way slabs. Also, the specimens with straps exhibited a higher level of ductility compared with other restrained slabs.

- Higher CMA in the proposed system can be expected that lead to further enhancement in the loading capacity, provided a concrete with higher compressive strength is used for constructing the slabs.

- The load-deflection response of samples with the same reinforcing configurations are depicted and compared in Figure 5-1.

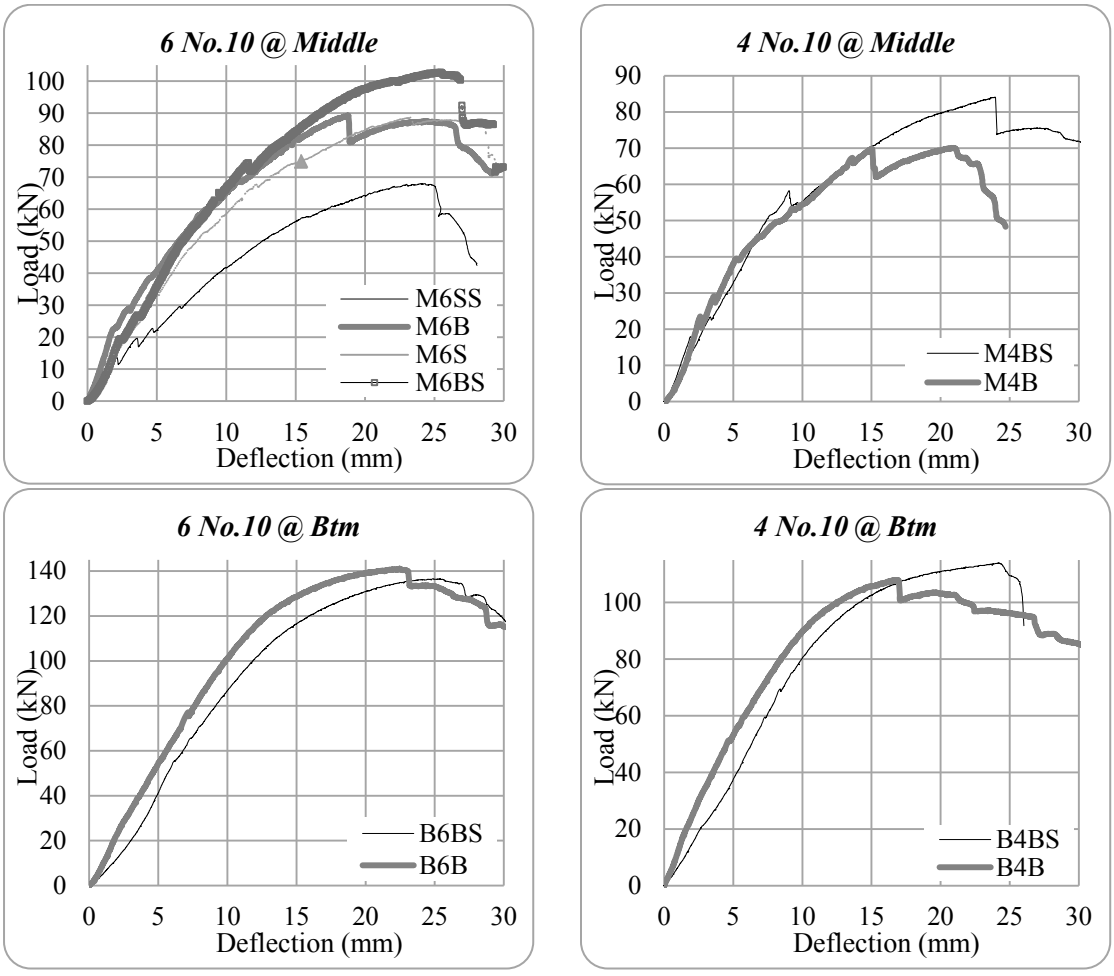

Figure 5-1. Load-deflection response of RC slabs specimens with the same amount of reinforcing steel bars but with different locations for the reinforcement.

- It can be concluded that samples with reinforcement located at the soffit of the slab show higher toughness (energy-based ductility) compared with samples with one layer of isotropic reinforcement placed at the middle depth of slab.

- Use of straps together with X bracing as lateral restraining system (last four samples) does not make significant change in the ductility index. This proves

that inducing the CMA action and accordingly shifting the failure model would not necessarily lead to brittle failure modes (with lower ductility).

- A 2D FE modelling has been conducted to simulate the behaviour of 10 one-was RC slabs restrained against lateral expansion. Results of numerical modelling have been compared with experimental data. A good consistency between the FE results and experimental data was observed.
- The FE models produced load-deflections which are overly stiff compared with experimental data. This is particularly the case for those samples with lateral X bracings and straps (last four samples). Also, it can be seen that numerical models are incapable of capturing the first sharp drops observed in the experimental load-deflection diagrams. These discrepancies can be attributed to the 3D cracking effects in the vicinity of bolted shear connectors that cannot be captured by the developed 2D FE models.

The experimental ultimate loading capacity of all 10 tested specimens is provided in Figure 5-2.

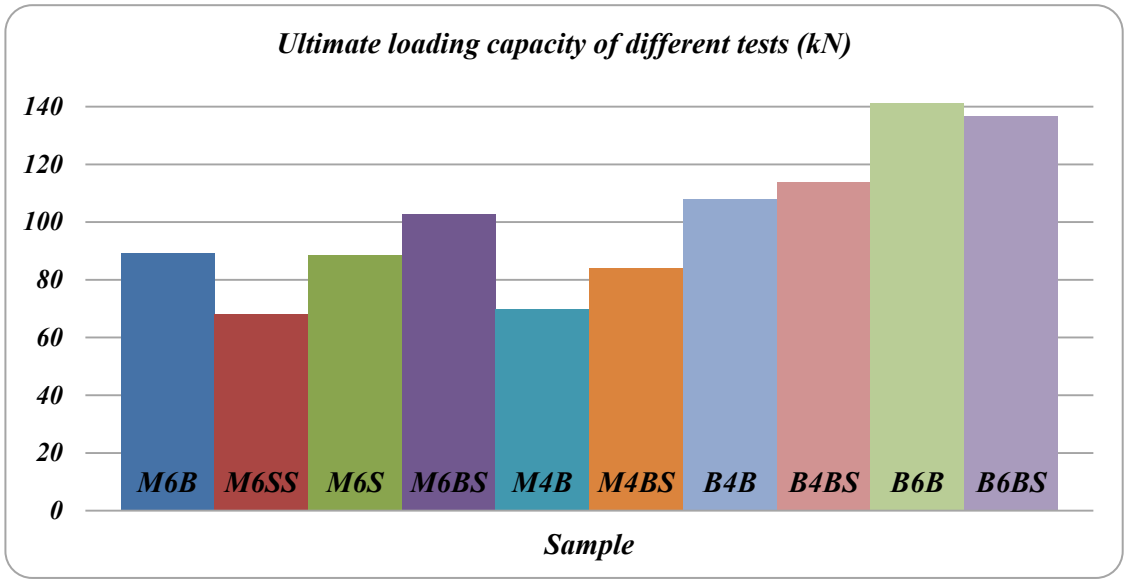

Figure 5-2. Comparison of experimental ultimate loading capacity for all 10 tested specimens.

The proposed system allows for replacing the internal reinforcements with external straps or X cross bracings. This feature can improve the service life of bridge decks

subjected to corrosion. Furthermore, in the proposed composite system the precast slabs can be easily replaced, in case repair or rehabilitation of the deck is required.

REFERENCES

ACI COMMITTEE 544 1998. Design Considerations for Steel Fibre Reinforced Concrete (ACI 544.4R-88). *American COncrete Institute, 18 pp*.

ALSAYED, S. H. & ALHOZAIMY, A. M. 1999. Ductility of concrete beams reinforced with FRP bars and steel fibers. *Journal of Composite Materials,* 33**,** 1792-1806.

ASTM 1992 Standard test for flexural toughness and first-crack strength of fibre-reinforced concrete (using beam with third-point loading). *C 1018, West Conshohocken, Pa.***,** 514-520.

AZAD, A. K., BALUCH, M. H., ABBASI, M. S. A. & KAREEM, K. 1994. Punching capacity of deck slabs in girder-slab bridges. *ACI Structural Journal,* 91**,** 656-662.

AZAD, A. K., BALUCH, M. H., AL-MANDIL, M. Y., SHARIF, A. M. & KAREEM, K. 1993. Loss of punching capacity of bridge deck slabs from crack damage. *ACI Structural Journal,* 90**,** 37-41.

BAKHT, B. & LAM, C. 2000. Behavior of transverse confining systems for steel-free deck slabs. *ASCE, Journal of Bridge Engineering***,** 139-147.

BAKHT, B. & MUFTI, A. A. 1996. FRC deck slabs without tensile reinforcement. *Concrete International,* 18**,** 50-55.

BRAESTRUP, M. W. 1980. Dome Effect in RC Slabs: Rigid-Plastic Analysis,. *ASCE, Journal of structural engineering,* 106**,** 1237-1253.

BROTCHIE, J. F. 1963. A refined theory for slabs. *Journal of the Institution of Engineers, Australia,* 35**,** 292-296.

BS 5400 1990. *British Standard Institute, British Standard for the design of steel, concrete and composite bridge, London*.

ČERVENKA, V., JENDELE, L. & ČERVENKA, J. 2012. ATENA Program Documentation-Part 1-Theory *Cervenka Consulting Ltd.*

CHRISTIANSEN, K. P. 1963. the effect of membrane stresses on the ultimate strength of interior panel of reinforced concrete slab. *Structural Engineer,* 41**,** 261-265.

CHRISTIANSEN, K. P. & FREDRIKSEN, V. T. 1983. Experimental investigation of rectangular concrete slabs with horizontal restraints. *Materials and Structures,* 16**,** 179-192.

COPE, R. J. & RAO, P. V. 1977. Non-linear finite element analysis of concrete slab structures. *Proc Inst Civ Eng (Lond),* 63**,** 159-179.

COPE, R. J. & RAO, P. V. Non-linear finite element strategies for bridge slabs. 1981. 273-288.

DALLAM, L. N. 1968. Pushout tests with high strength bolt shear connectors. . *Report for Missouri State Highway Department, Department of Civil Engineering, University of Missouri – Columbia.*

DALLAM, L. N. & HARPSTER, J. L. 1968. Composite beam tests with high-strength bolt shear connectors. . *Report for Missouri State Highway Department, Department of Civil Engineering, University of Missouri – Columbia.*

DATTA, T. K. & RAMESH, C. K. 1975. Some experimental studies on a reinforced concrete slab-beam system. *Magazine of Concrete Research,* 27**,** 111-120.

DESAYI, P. & KULKARNI, A. B. 1977. Membrane action, deflections and cracking of two-way reinforced concrete slabs. *Matériaux et Constructions,* 10**,** 303-312.

EYRE, J. R. 1990. Flow Rule in Elastically Restrained One-Way Spanning RC Slabs. *Journal of Structural Engineering,* 116**,** 3251-3267.

EYRE, J. R. 1997. Direct assessment of safe strengths of RC slabs under membrane action. *ASCE, Journal of structural engineering,* 123**,** 1331-1338.

EYRE, J. R. & KEMP, K. 1984. A graphical solution predicting increase in strength of slabs. *Magazine of Concrete Research,* 35**,** 151-156.

EYRE, J. R. & KEMP, K. 1994. In-plane stiffness of reinforced concrete slabs under compressive membrane action. *Magazine of Concrete Research***,** 67-77.

FANG, I. K., LEE, J.-H. & CHEN, C.-R. 1994. Behavior of partially restrained slabs under concentrated load. *ACI Structural Journal,* 91**,** 133-139.

FANG, I. K., WORLEY, J., BURNS, N. H. & KLINGNER, R. E. 1990. Behavior of isotropic R/C bridge decks on steel girders. *Journal of structural engineering New York, N.Y.,* 116**,** 659-678.

FOSTER, S. J. & ATTARD, M. M. 1997. Experimental tests on eccentrically loaded high-strength concrete columns. *ACI Structural Journal,* 94**,** 295-303.

GVOZDEV, A. A. 1960. The determination of the value of the collapse load for statically indeterminate systems undergoing plastic deformation. *International Journal of Mechanical Sciences,* 1**,** 322-335.

HAYES, B. 1968. Allowing for membrane action in the plastic analysis of rectangular reinfroced concrete slabs. *Magazine of Concrete Research,* 20**,** 205-212.

HUNG, T. Y. & NAWY, E. G. 1971. Limit strength and serviceability factors in uniformly loaded isotropically reinforced two-way slabs. Cracking, Deflection and Ultimate Load of Concrete Slab Systems. *ACI Special Publication, SP-30, Detroit, 1971,* 301-311.

JANAS, M. 1973. Arching Action in Elastic-Plastic Plates. *J. Srruct. Mech,,* 1**,** 277-293.

JEONG, S.-M. & NAAMAN, A. E. Ductility of concrete beams prestressed with FRP tendons. 1995. 1466-1469.

KEMP, K. O. 1967. Yield of square reinforced concrete slab on simple supports allowing for membrane action. *Structural Engineer,* 45**,** 235-240.

KIRKPATRICK, J., RANKIN, G. I. B. & LONG, A. E. 1984a. Strength evaluation of M-beam bridge deck slabs. *Structural Engineer,* 62B**,** 60-68.

KIRKPATRICK, J., RANKIN, G. I. B. & LONG, A. E. 1986. Influence of comperssive membrane action on the serviceability of beam and slab bridge decks. *Structural Engineer, Part B: R&D Quarterly,* 64 B**,** 6-9, 12.

KLOWAK, C., MEMON, A. & MUFTI, A. 2006. Static and fatigue investigation of second generation steel-free bridge decks. *Cement and Concrete Composites,* 28**,** 890-897.

KWON, G., ENGELHARDT, M. D. & KLINGER, R. E. 2010. Behavior of post-installed shear connectors under static and fatigue loading. *Journal of Constructional Steel Research,* 66**,** 532-541.

LAHLOUH, E. H. & WALDRON, P. 1992. Membrane action in one-way slab strips. *Proceedings of the Institution of Civil Engineers, Structs & Bldgs,* 94**,** 419-428.

LEE, S. S. M. & BRADFORD, M. A. 2013a. Sustainable composite Beams with deconstructable bolted shear connectors. *SEMC 2013: The Fifth International Conference on Structural Engineering, Mechanics and Computation, Cape Town, South Africa*.

LEE, S. S. M. & BRADFORD, M. A. 2013b. Sustainable composite beam behaviour with deconstructable bolted shear connectors-Full scale experimental investigation. *Concrete 2013, Gold Coast, Wueensland, Australia*.

LIEBENBERG, A. C. 1966. Arch action in concrete slabs (Parts 1&2). *South African Counsil for Scientific and Industrial Research,* Report No. 234.

LONG, A. E. 1975. A Two-phase approach to the prediction of the punching strength of slabs. *Journal of American Concrete Institute, Proceeding,,* 72**,** 37-45.

LONG, A. E. & BOND, D. 1967. Punching failure of reinforced concrete slabs. *Proc Inst Civ. Engrs (Lond), 1967,* 37**,** 109-135.

MARSHALL, W. T., NELSON, H. M. & BANERJEE, H. K. 1971. An experimental study of the use of high-strength friction-grip bolts as shear connectors in composite beams. *The Structural Engineer* 49**,** 171-178.

MASTERTON, D. M. & LONG, A. E. 1974. The punching strength of slabs a flexural approach using finite elements,. *ACI Special publication, SP-42: Shear in reinforced concrete,* 2, part 4**,** 747-768.

MATTOCK, A. H., KRIZ, L. B. & HOGNESTAD, E. 1961. Rectangular concrete stress distribution in ultimate strength design. *ACI,* 57**,** 875-926.

MCDOWELL, E. L., MCKEE, K. E. & SEVIN, E. 1956. Arching action theory of masonry walls. *J. Struct. Div. ASCE,* 82(ST2).

MORLEY, C. T. 1967. Yield line theory for reinforced concrete slabs at moderately large deflections. *Magazine of Concrete Research,* 19**,** 211-222.

MORLEY, C. T. & OLONISAKIN, A. A. 1995. The Galerkin method applied to compressive membrane action. *Development in computational techniques for structural engineering,* Ch.47, 1995.

MUFTI, A. A., JAEGER, L. G., BAKHT, B. & WEGNER, L. D. 1993. Experimental investigation of fibre-reinforced concrete deck slabs without internal steel reinforcement. *Canadian Journal of Civil Engineering,* 20**,** 398-406.

NAAMAN, A. E., HARAJLI, M. H. & WRIGHT, J. K. 1986. ANALYSIS OF DUCTILITY IN PARTIALLY PRESTRESSED CONCRETE FLEXURAL MEMBERS. *Journal - Prestressed Concrete Institute,* 31**,** 64-87.

NI 1990. *Department of the Environment, Design Specification for Bridge Decks, DOE, Northern Island*.

NIBLOCK, R. 1986. Compressive membrane action and the ultimate capacity of uniformly loaded reinforced concrete slabs. *PhD Thesis, Queen's University of Belfast, Northern Island 1986*.

OCKLESTON, A. J. 1955. Load Tests on a Three Storey Reinforced Concrete Building in Johannesburg. *The Structural Engineer***,** 304.

OCKLESTON, A. J. 1958. Arching action in reinforced concrete slabs. *Structural Engineer,* 36**,** 197-201.

OHBD 1992. *Ontario Ministry of Transport, Ontario Highway Bridge Design Code (OHBD), 1979 [amended 1983 & 1992]*.

PARK, R. 1964. Tensile membrane behavior of uniformly loaded rectangular reinforced concrete slabs with fully restrained edges. *Magazine of Concrete Research,* 16**,** 39-44.

PARK, R. 1964a. Ultimate strength of rectangular concrete slabs under ultimate load with edge restraint. *Proceedings of the Institution of Civil Engineers,* 28**,** pp 125-150.

PARK, R. 1964b. Ultimate strength and long term behaviour of ultimate load in two way concrete slabs. *Magazine of Concrete Research,* 16**,** pp 139-152.

PARK, R. 1965. The lateral stiffness and strength required to ensure membrane action at ultimate load. *Magazine of Concrete Research,* 17**,** pp 29-38.

PARK, R. & GAMBLE, W. L. 1980. *Reinforced Concrete Slabs,* New York, USA., John Wiley & Sons.

PETROU, M. F. & PERDIKARIS, P. C. 1996. Punching shear failure in concrete decks as snap-through instability. *Journal of Structural Engineering,* 122**,** 998-1005.

POWELL, D. S. 1956. *The ultimate strength of concrete panels subjected to uniformly distributed loads,* Cambridge University.

RAMESH, C. K. & DATTA, T. K. 1973. Ultimate strength of reinforced concrete slab-beam systems. *The Indian Concrete Journal,* 47**,** 301-308.

RANKIN, G. I. B. 1982. Punching failure and compressive membrane action in reinforced concrete slabs. *PhD thesis, Queen's University of Belfast, Northern Island, 1982*.

RANKIN, G. I. B. & LONG, A. E. 1987a. Predicting the punching strength of conventional slab-column specimens. *Proceedings of the Institution of Civil Engineers (London),* 82**,** 327-346.

RANKIN, G. I. B. & LONG, A. E. 1987b. Predicting the enhanced punching strengthof interior slab-column connections. *Proceedings of the Institution of Civil Engineers (London),* 82**,** 1165-1186.

RANKIN, G. I. B. & LONG, A. E. 1997. Arching action strength enhancement in laterally-restrained slab strips. *Proceedings of the Institution of Civil Engineers, Structs & Bldgs* 122**,** 461-467.

RUDDLE, M. 1990. Arching action and the ultimate capacity of reinforced concrete beams. *PhD thesis, Queen's University of Belfast, Northern Island 1990*.

RUDDLE, M. E., RANKIN, G. I. B. & LONG, A. E. 2002. Arching action—flexural and shear strength enhancements in rectangular and Tee beams. *Proceedings of the Institution of Civil Engineers, Structures and Buildings,* 156**,** 63-74.

SAWZUCK, A. & WINNICK, L. 1965. Plastic behaviour of simply supported plates at moderately large deflections. *International Journal of Solids and Structures,* 1**,** 97-111.

SHARPE, R. L. 1977. EARTHQUAKE PROBLEM. *ACI Special Publication, SP-53, Detroit***,** 25-46.

SKATES, A. 1987. Development of a design method for restrained concrete slab systems subject to concentrated and uniform loading. *PhD thesis, Queen's University of Belfast, Northern Island 1987*.

SPADEA, G., BENCARDINO, F. & SWAMY, R. N. 1997. Strengthening and Upgrading Structures with Bonded CFRP Sheets Design Aspects for Structural Integrity. *Proceedings of the Third International RILEM Symposium (FRPRCS-3): Non-Metallic (FRP) for Concrete Structures, Sapporo, Japan,* 1**,** 379-386.

TAYLOR, R. & HAYES, B. 1965. Some tests on the effect of edge restraint on punching shear in RC slabs. *Magazine of Concrete Research.*

TAYLOR, S. E. 2000. Compressive membrane action in high strength concrete bridge deck slabs. *PhD Thesis, Queen's University of Belfast, January 2000.*

TAYLOR, S. E., RANKIN, B., CLELAND, D. J. & KIRKPATRICK, J. 2007. Serviceability of Bridge Deck Slabs with Arching Action. *ACI Structural Journal,* 104**,** 39-48.

TAYLOR, S. E., RANKIN, G. I. B. & CLELAND, D. J. 2001. Arching action in high-strength concrete slabs. *Proceedings of the Institution of Civil Engineers: Structures and Buildings,* 146**,** 352-362.

TURNER, C. A. P. 1909. Concrete Steel Construction: Part 1, Buildings. *ACI Special Publication, , American Concrete Institute, Michigan, USA,* .

VALIPOUR, H. R. & FOSTER, S. J. 2009. Nonlocal damage formulation for a flexibility-based frame element. *Journal of Structural Engineering,* 135**,** 1213-1221.

WESTERGAARD, H. M. & SLATER, W. A. 1921. Moments and stresses in slabs. *J. Am. Conc. Inst.,* 17**,** 415-538.

WOOD, R. H. 1961. Plastic and elastic design of slabs and plates. *Thames and Hudsen, London, 1961*.